Effect of Laser Welding and Stretch Forming on the Corrosion Performance of Hot-Dip Galvanized Steel

by

Ken Yu-Jen Su

A thesis
presented to the University of Waterloo
in fulfillment of the
thesis requirement for the degree of
Master of Applied Science
in
Mechanical Engineering

Waterloo, Ontario, Canada, 2008

AUTHOR'S DECLARATION

I hereby declare that I am the sole author of this thesis. This is a true copy of the thesis, including any required final revisions, as accepted by my examiners.

I understand that my thesis may be made electronically available to the public.

ABSTRACT

The use of laser welding in the automotive industry in the past few decades has facilitated joining of hot-dip galvanized (HDG) steel sheets at high production rates and low cost. The recent development of tailor welded blanks (TWB) using laser welding allowed combinations of sheet grades and thicknesses to "tailor" the vehicle part for optimized design, structural integrity and crash performance but more importantly, reductions in weight. Welded blanks are further subjected to stamping or stretch forming prior to final assembly. Unfortunately, both welding and stretch forming cause the galvanized coating to deteriorate, and thereby, undermine the long term corrosion protection. Despite existing publications on zinc coated steel and advances in processing techniques, there is a lack of understanding on the influence of laser welding and stretch forming on the corrosion performance of HDG steel. Hence, the purpose of this study was to determine how welding speed and biaxial strain affect interstitial-free (IF) and high strength low allow (HSLA) steel coupons when they are subjected to continuous immersion and accelerated corrosion tests. The corrosion rates of the coupons were evaluated using electrochemical techniques and gravimetry.

Changes in the galvanized coating were characterized using scanning electron metallography. It was observed that, the original zinc layer transformed into the delta and gamma Fe-Zn intermetallic phases locally in the heat affected zone (HAZ) after laser welding. The resulting microstructure was similar to that of a commercially galvannealed coating and exhibited superior corrosion resistance than that of pure zinc.

Linear polarization resistance (LPR) measurements revealed that the zinc coating was able to protect a chemically exposed region of steel in 0.1 M NaCl solution. While the Nd:YAG laser welded coupons with narrow HAZs performed equally well as the non-welded ones, diode laser welded coupons, with a wide locally annealed coating in the HAZ, exhibited a decrease in the peak corrosion rate of zinc. Moreover, minimal amounts of rust were observed on the surface of the HAZ after testing. With biaxial strain, welded and deformed coupons generally demonstrated higher peak corrosion rates than that of undeformed welded ones.

When subjected to cyclic corrosion testing according to SAE J2334, rust formed in the exposed region after one 24 hour test cycle due to wet-dry conditions. However, zinc corrosion products on

the surface provided substantial corrosion resistance to the remaining zinc coating and to the steel substrate. Gravimetric measurements of welded coupons showed a linear increase in weight gain with increased exposed widths of the steel after 30 cycles but biaxial strain further increased the weight gain on deformed coupons. After 60 cycles, the trend became exponential for both welded and deformed coupons. There was a negligible difference between the corrosion performance of IF and HSLA steel.

Using X-Ray diffraction and Raman spectroscopy, species of both iron and zinc corrosion products were identified. Without the application of paint coatings, zinc oxide (ZnO), zinc hydroxy chloride ($ZnCl_2[Zn(OH)_2]_4$), and hydrozincite ($[ZnCO_3]_2[Zn(OH)_2]_3$) were responsible for passivating the surface and reducing the overall corrosion rate of the galvanized coating.

ACKNOWLEDGEMENTS

First and foremost I want to thank my wife Linda, for loving and supporting me unconditionally. I am grateful to have her with me while I accomplished the master's degree at the University of Waterloo. I want to thank my parents and all my family for their love and support in my education.

I wish to thank both of my thesis supervisors for their guidance and support in this research. Dr. Carolyn Hansson has sharpened my critical thinking over the time of this work. Her professionalism, expertise and considerations are greatly admired. Thanks to Dr. Norman Zhou for pointing out aspects in both the research and industry environment and for encouraging me to make my own decisions for research.

This research could not have been completed without the financial and in-kind support from the International Lead Zinc Research Organization (ILZRO), Teck Cominco Metals Ltd., Ontario Centres of Excellence (OCE), formerly ATC-Power Lasers and ArcelorMittal Dofasco. I am thankful to Dr. Greg Zhang for commenting on the galvanic interactions of Fe-Zn couples, Dr. Hong Ping Gu for helping me prepare Nd:YAG laser welded samples, Elliot Biro for providing the steels so promptly, and Paul Andreychuk for conducting limited dome height testing so proficiently.

I am indebt to the colleagues and alumni at the Concrete Durability Laboratory. Thanks to Dr. Shahzma Jaffer, Dr. Amir Poursaee, Kyle Anders, and Brad Bergsma for being wonderfully helpful. Your delicious birthday deserts will be terribly missed. Thanks to all the colleagues and alumni at the Centre for Advanced Materials Joining for their comments and friendship. Dr. Michael Kuntz, Dr. Xiaogang Li, Dr. Sushanta Panda, Narasimhan Sreenivasan, Mingshen Xia, Victor H. Baltazar H. and Ibraheem Khan were specifically resourceful and supportive during the course of this research.

DEDICATION

To my grandmother

who took care of me and taught me

in her simple ways

TALBE OF CONTENTS

LIST OF FIGURES

LIST OF TABLES

CHAPTER 1
INTRODUCTION

With a continuous increase in gasoline prices and exhaust emission that contribute to global climate change, the automotive industry is conscientious in trying to reduce the weight and cost of our vehicles while maintaining the structural integrity and crash performance. Along with performance requirements of the auto body, the need for corrosion resistance remains an important issue for protection against weathering in the natural environment. To name a few, galvanic, crevice, and pitting corrosion are commonly seen on vehicle bodies that deteriorates the cosmetic appearance. This is particularly an issue in places where de-icing salts are used in the winter because significant corrosion to components under the vehicle as well as to the visible exterior can occur. Steel sheets used for the auto body are typically galvanized with a zinc coating followed by a phosphate coat, E-coat, primer coat, and finally a top coat. The value of zinc and each additional coating comes to extend the cosmetic appearance and life of the auto body by acting as isolating physical barriers so that steel is not directly exposed to the environment. In addition, if the coating is scratched or damaged zinc can cathodically protect steel by sacrificing itself and corrode preferentially before steel starts to corrode. Therefore, the majority of steel sheets used in the automotive industry are zinc coated for corrosion protection.

Zinc coating is produced by hot dip galvanizing (HDG) in which a metallurgical bond is formed between the zinc and the steel surface. In a continuous galvanizing line, steel sheets are immersed in a molten zinc bath and withdrawn slowly. In addition, 0.135 wt.% of aluminum is added to the zinc bath so that a thin layer containing iron and aluminum forms on the side of the steel surface. This inhibition layer of Fe_2Al_5 allows a ductile coating of pure zinc to deposit on top of the steel substrate as protection barrier against corrosion (Marder 2000). Although galvanized steel is popularly used on vehicle frames and components, its smooth surface finish actually makes paint application difficult on the zinc coating. Therefore, in order to improve paint adherence on the zinc coating, an annealing process is sometimes used as the subsequent step to allow a reaction between zinc and the steel substrate to take place. This is better known as galvannealing (GA) where the formation of iron-zinc alloys in the coating can provide excellent wear and corrosion resistance and

are typically used on external body panels. The interested reader is referred to “the metallurgy of zinc coated steels” by Marder, A.R.

After galvanizing, the steel sheets undergo two additional processes in the manufacture of their final shape or component: laser welding and stretch forming.

1.1 Laser Welding

The application of a laser beam in materials joining processes dates back to the 1960’s. There are several advantages in using a laser for joining metals in comparison to brazing, soldering and solid state welding. These include the elimination of flux, the elimination of unnecessary metal interfaces in the current path, and higher operating temperatures. With the continuous development of laser beams, the power input have increased to a magnitude of $10^6 \sim 10^7$ W/cm^2. In the modern laser welding system, the ability of computer control allows laser power to be varied for different welding conditions. The use of optical feedback and monitoring systems further optimizes the laser welding process to better suit different industrial applications and needs (Duley 1999). Even though laser welding has higher capital costs than conventional welding processes such as gas tungsten arc welding (GTAW) or resistance spot welding (RSW), laser welding provides many attractions to remain economically competitive. A narrow heat-affected zone, minimal thermal distortion, high processing speed, and improved metallurgical properties are all qualities seen on a laser weld (Xie and Denney 2001).

Despite the drawback that laser welding is very sensitive to gap or misalignment and reflective materials, its versatility and productivity facilitate many applications in different industries. The field of tailor blanking in the automotive industry is a prominent example of such application and is described in the following section. Joining galvanized steel was made easy with a laser where electrode degradation on a resistance spot weld was problematic. Further, structural components that are laser welded generally demonstrate improved crash performance than those that are resistance spot welded (Bocos, Zubiri et al. 2005).

1.2 Tailor Welded Blanks

A tailor welded blank (TWB) is the term used to describe a part in which two or more steel sheets having dissimilar thicknesses and/or grades are laser welded together by a linear butt joint. This can be seen in Figure 1-1 where a typical vehicle side panel consisting of different grades of steel and different thicknesses are welded together to form an optimized blank. The design optimization is achieved through a thickness increase near the engine fire wall and around hinges which require improved crash performance and a thickness reduction near the rear where strength can be compromised. The overall number of parts to be combined is reduced thereby reducing the weight of the vehicle. The blanks are placed between forming dies to achieve intricate shapes as vehicle components.

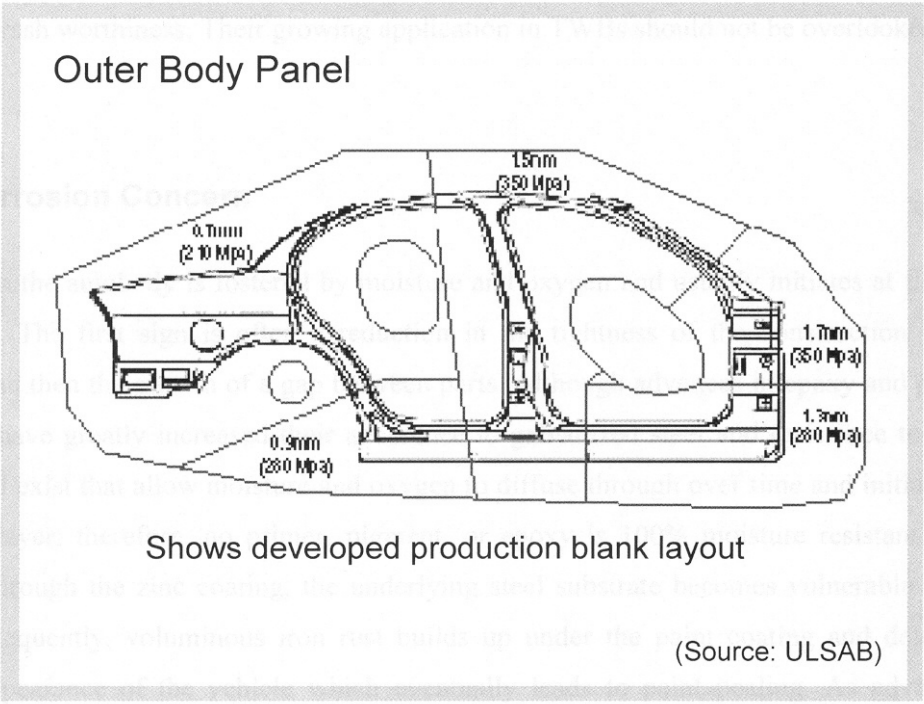

Figure 1-1: Outer layer of body side panel with over 4.8m of weld (2001)

Until recently, the most popular TWB components are door inners, and body side panels, followed by B-Pillars and rails. TWBs are currently the best solution for attaining high strength to weight ratio while maintaining crash performance using the laser welding process (2001). The leading

users of TWBs include GM and DaimlerChrysler in North America; Toyota, Nissan and Honda in Japan; and Volkswagen, BMW and Mercedes in Europe (2001). A report from a consortium of major steel makers, called Ultra Light Steel Auto Body (ULSAB), points out that close to half of the auto body by mass is expected to be formed from tailored blanks in the near future (1998).

Conventionally, the interstitial-free (IF) steel has been the popular grade for making TWBs due to its excellent drawing properties even after laser welding. With high strength low alloy (HSLA) steels, higher yield strengths are achieved while reasonable ductilities are maintained. Research has confirmed that IF and HSLA grades made for TWBs exhibit satisfactory fatigue strength and formability (Aristotile and Fersini 1999). Therefore, laser welded components are well suited for subsequent stretching. In recent years, the use of advanced high strength steels such as dual phase (DP) and transformation induced plasticity (TRIP) steels has increased gradually with proven acceptable crash worthiness. Their growing application in TWBs should not be overlooked.

1.3 Corrosion Concern

Corrosion on the autobody is fostered by moisture and oxygen and usually initiates at flange or hem connections. The first sign is often a reduction in the tightness of the construction followed by loosening and then the growth of a gap between parts. Although advances in epoxy and paint coating technology have greatly increased their adherence to galvanized steel and resistance to weathering, pinholes still exist that allow moisture and oxygen to diffuse through over time and initiate pits in the galvanized layer; therefore, no primer, pigment, or epoxy is 100% moisture resistant. Once a pit penetrates through the zinc coating, the underlying steel substrate becomes vulnerable to corrosion attack. Subsequently, voluminous iron rust builds up under the paint coating and deteriorates the cosmetic appearance of the vehicle which eventually leads to paint pealing. As advantageous as TWBs are, there are shortcomings. Both laser welding and stretch forming steps can possibly undermine the corrosion protection. While the zinc coating is lost along the weld during welding, it becomes thinner after stretch forming. Therefore, after attaining their final shape inside the dies, the zinc coating on these components will have experienced deterioration and possibly reduction in corrosion resistance.

In an effort to better understand the protection of galvanized zinc coatings and their overall performance, the Automotive Corrosion & Prevention Committee[i] (ACAP) in cooperation with Auto/Steel Partnership (2001) have developed a cosmetic corrosion lab test to simulate the long term exposure of fully coated (with a phosphate, E-coat[ii], primed, and top coat layer) galvanized steel under normal atmospheric conditions. By subjecting test coupons to alternating wet and dry conditions and elevated temperatures in an environmental chamber, corrosion acceleration can be achieved. An earlier study compared the cosmetic corrosion of blanks made from both mash-seam and laser welding (Simpson, Hoffman et al. 1998). They concluded that due to a wider damage in the zinc coating, mash-seam welded blanks revealed a greater deterioration than laser welded ones. In another comparison on the cosmetic corrosion performance of hot-dip galvanized panels, it was found that laser welded panels showed improved corrosion resistance over resistance spot welded and mash-seam welded panels (Van Ooij, Edwards et al. 1991).

1.4 Thesis Objective and Outline

Generally, the corrosion rate of free zinc is relatively linear and is directly proportional to the duration of exposure in the environment. While research on the corrosion properties of zinc (Slunder and Boyd 1983) and the performance of zinc coatings (Porter 1991) can be found in a vast number of publications, little work was conducted to understand how processing affects the corrosion performance of zinc coated steel. Therefore, it is the objective of this thesis to evaluate specifically the effect of laser welding and stretch forming on the corrosion performance of HDG steels. Using both continuous immersion and accelerated corrosion tests, this work intends to address some of the following questions:

- how do varying welding speeds, hence weld widths affect the corrosion rate?
- how do different steel grades influence the corrosion rate?

[i] Under the materials, processes, and parts council in the society of automotive engineers (SAE)

[ii] Application of organic resin paint coating by electrolysis

- how does the formation of the heat affected zone influence zinc protection?
- how long can zinc protect the weld?
- what is the corrosion potential of zinc coupled to the weld?
- What are the corrosion products formed?
- how does stretch forming affect the corrosion performance of the zinc coating?

Both IF and HSLA steels with a HDG coating have been selected as the test material in this work. Two thicknesses are chosen as the basis for a TWB. The corrosion progress is to be monitored by electrochemical techniques while long term corrosion rates are estimated from the accelerated laboratory test data. It is the intent of this work to provide corrosion data for use in models so that future predictions can be made to assess the long-term behaviour of galvanized steels. An understanding of corrosion promises to be fruitful to the aesthetics of a vehicle and future design considerations.

In this thesis, a literature review of the changes in the zinc coating associated with laser welding and stretch forming is given in chapter two. In addition, the corrosion properties and electrochemistry of zinc and iron are included. Chapter three details the experimental procedures including, welding and forming parameters, continuous immersion and accelerated corrosion tests and use of analytical tools. Chapter four examines the transformation of the zinc coating after laser welding and stretch forming. The corrosion potential and current density trends over time and the corrosion rates of galvanized steel in solution is presented in chapter five while gravimetry results and thickness reduction of the zinc is discussed in chapter six. In chapter seven, corrosion products of iron and zinc are summarized. Finally, up to date conclusions and recommendations for future work are presented in chapter eight and nine respectively.

CHAPTER 2
LITERATURE REVIEW

2.1 Galvanized Steels on Autobodies

Steel sheets used in the automotive industry must possess excellent weldability as well as formability. Therefore, they must retain excellent deep-drawing properties after laser welding in order to endure forming without fracture. Furthermore, the galvanized zinc coating must remain adherent to the steel substrate after the forming operation to retain its corrosion protection. The conventional interstitial – free (IF) and high strength low alloy (HSLA) steels exhibit excellent mechanical properties demonstrated through tensile tests (Bocos, Zubiri et al. 2005) and ability to retain the zinc on the surface. For those reasons, they have been widely used in TWB applications. A review of the changes in their microstructure and properties due to manufacturing processes are essential in further investigation of their corrosion performance.

2.1.1 Interstitial-Free (IF) Steel

This ultra low carbon steel (0.005% max) is often stabilized with elements such as titanium and/or niobium in order for carbon and nitrogen atoms to precipitate, hence leaving an interstitial free ferrite matrix (2002). Its exceptional formability is particularly used for deep drawing where the steel exhibits high resistance to thinning during processing. This property makes IF steel well suited for the application of tailor welded blanks. Typical components that use this type of steel include door inners and body side inners. However, one draw back of the IF steel is that its low yield strength makes it susceptible to fatigue.

After laser welding IF steel, Panda et al. (2007) reported significant grain growth in the heat affected zone (HAZ) while the fusion zone (FZ) consisted of elongated ferrite and bainite grains. In their study, the formation of bainite in the fusion zone increased the hardness of the weld to as much

as twice that of the parent metal. Further, tensile tests of welded IF specimens in both the longitudinal and transverse direction showed higher Y.S and UTS values than those of parent metal.

2.1.2 High Strength Low Alloy (HSLA) Steel

Similar to IF steel, HSLA steels are produced by alloying small amounts of niobium, titanium and vanadium to form fine grained ferrite matrix but in this case, with dispersed carbides or carbonitrides at the grain boundaries (2002). Although there is a significant increase in strength, it is accompanied by a reduction in ductility. Nonetheless, the relatively high toughness and strength to weight ratio allow HSLA to be successfully designed in thinner sections or structural members on the autobody such as the rock inners or the b and c pillars (2002). HSLA steels typically have yield strengths between 280~500 MPa that offer satisfactory dent and fatigue resistance while maintaining reasonable formability and weldability. Research shows that after welding with a diode laser, HSLA maintains similar strengths as the parent metal at various welding speeds (Xia, Sreenivasan et al. 2007). Hence, laser welding has only a minor effect on the formability of HSLA compared with IF steel. Moreover, HSLA has been found to be more corrosion resistant than plain carbon steels which makes it more useful for automakers (Callister Jr. 1997). Since the HAZ is of particular importance for formability after laser welding, it is important to investigate how the HAZ influences the corrosion behaviour.

2.2 Laser Welding

Of the common laser beams used in materials joining today, CO_2 gas was the earliest type of laser applied particularly in the heavy industries such as ship building and iron and steel making where thick plates need to be welded together. It was also the dominant laser initially in the automotive industry. Different sets of reflective mirrors and lenses are used to focus the laser beam obtained from a mixture of CO_2, N_2 and He gases. Despite its high output power of up to 10 kW during welding, problems occur due to a build up of high vapour pressure inside the keyhole which generates a turbulent weld pool with violent fluid motion that often lead to quality concerns. Blowholes and

porosities are the most common defects when gas is trapped in the molten keyhole (Matsunawa, Mizutani et al. 2003). With the advancement in technology, solid state Nd:YAG lasers quickly became more popular. The output of Nd:YAG lasers is often transmitted through fibre optic cables and integrated with a robot in a welding cell (Duley 1999). Finally, recent developments in semiconductors brought forward the high power diode laser as a contender. Its compactness and small floor foot print are attractive to the automotive industry. Details of these two laser systems are given below.

Prior to laser welding, it is well known that edge preparation and beam alignment are required to produce a sound quality weld. In addition, laser power is important during welding since it determines how much heat is given to the work piece. By affecting the fusion and the heat affected zone width, the test sample in the forming die will also be influenced.

2.2.1 Nd:YAG Laser

A tightly focused beam from an Nd:YAG laser is produced from a synthetic glass crystal composed of yttrium, aluminum garnet ($Y_3Al_5O_{12}$) and doped with triply ionized neodymium. The rod crystal is optically pumped with a flash lamp to produce output powers of up to 4 kW and power density greater than $10^{10}W/m^2$. Similar to the CO_2 laser, the Nd:YAG laser operates with a keyhole mode of welding which generates deep penetration and narrow welds. Welding setup and parameters must be optimized to avoid spatter caused by the molten metal with turbulence in the keyhole.

Looi et al. (2004) claim that after laser welding galvanized steel specimens are generally susceptible to intergranular attack. In particular, high heat input and slow welding speeds tend to deteriorate corrosion resistance of the coupon. The advantage of the Nd:YAG laser lies in its flexibility to deliver the laser beam through optic cables over long distances. Furthermore it is possible to couple two or more lasers into a single beam.

2.2.2 Diode Laser

Although the use of laser diodes has been mature in optical, medical and telecommunication applications, it was only applied in materials processing in recent years due to an increase in output power. A high power diode laser (HPDL) employs doped semiconductor crystals as sources to produce a monochromatic beam. However, due to the difference in diode geometry and divergence during focusing, a rectangular beam at the focal plane is produced (Howard 2005). Instead of generating a keyhole, the diode laser operates with conduction mode welding whereby heat is absorbed by the material and melts the base metal; hence high vapour pressure is avoided and a stable weld pool is obtained. However, welding with the diode laser can lead to increased fusion and heat affected zone widths. Figure 2-1 depicts the cross section with a conduction and keyhole weld.

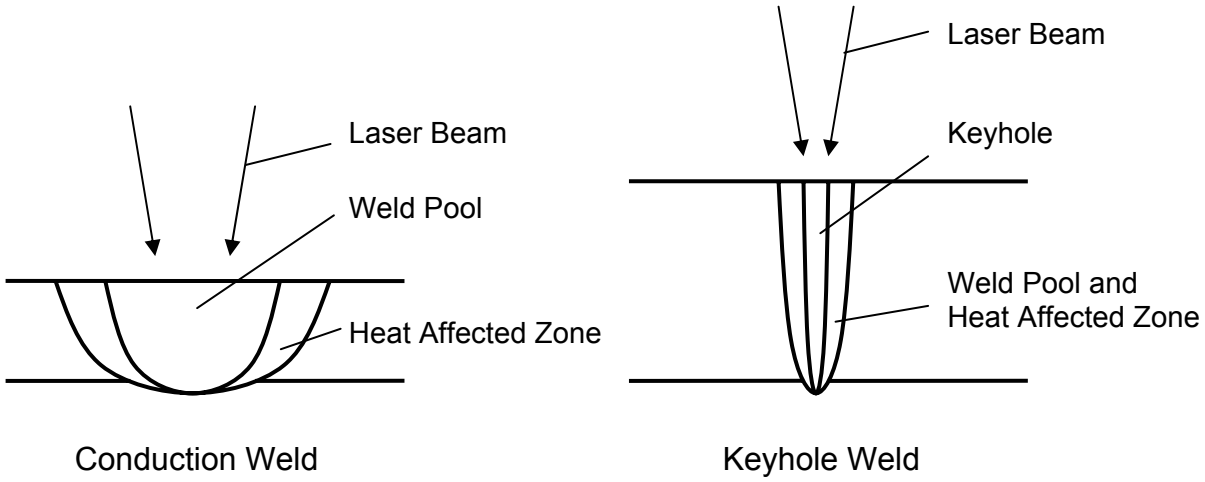

Figure 2-1: Conduction vs. Keyhole Welding

Despite its inferior beam quality and power, many uses of the HPDL still exist. For example, when traversed longitudinally, cutting, cladding, marking and welding can be performed (Nacey 2001). When the laser beam is traversed laterally, heat treating, surface glazing, and paint stripping can be achieved (Bocos, Zubiri et al. 2005). Diode lasers have been applied to weld stainless and carbon steel pipes, titanium alloys, and aluminum sheets (Nacey 2001; Howard 2005). Studies have

shown that diode laser welding is fully capable in butt, fillet and lap-joint configurations (Bliedtner, Heyse et al. 2001).

2.2.3 Laser Welding on Galvanized Steel

The main problem with laser welding of galvanized steel lies in the physical properties of zinc. Zinc has a low boiling point at 906°C/1663°F compared with the melting point of steel at 1530°C/2786°F. Therefore, when the laser is irradiated on galvanized steel sheets, the zinc coating will vapourize before the steel substrate melts. This setback is especially problematic in the lap joint configuration where one sheet overlays on top of another is welded together (Graham, Weckman et al. 1996). In the butt joint configuration, the fusion zone is completely exposed and left unprotected after welding. Depending on the laser power and welding parameters, the zinc coating in the heat affected zone (HAZ) may be partially exposed as well. This further increases the exposed width and leaves the steel substrate vulnerable to corrosion attack. In the present study, while a distance of 1 mm across the weld without zinc coating is generally observed on a coupon welded by Nd:YAG laser, more than 10 mm in total exposed width can be seen on those welded by the diode laser.

2.2.4 Fe-Zn Intermetallic Compounds

When steel sheets are joined together by fusion welding, they will experience a rapid fluctuation in temperature known as a thermal cycle. The sheets melt upon heating from the laser source and then solidify to form the weld. As the peak temperature decreases across the weld, distinct microstructural changes can be observed in the heat affected zone namely due to grain growth, recrystallization and tempering (Kou 1987). Similarly, the zinc coating immediately next to the exposed region or in the heat affected zone also experiences microstructural changes. With sufficient heat input, the aluminum inhibition layer in the galvanized coating will break down. Consequently, the zinc coating is allowed to diffuse into the steel substrate and transform into Fe-Zn intermetallic compounds. This is similar to the commercial galvannealing process where a HDG coating is heat treated to obtain Fe-Zn intermetallic compounds for better paint adhesion and corrosion resistance. Hence, the effect of

thermal cycle on the zinc coating due to laser welding causes a localized transformation from that of a HDG coating to a GA one.

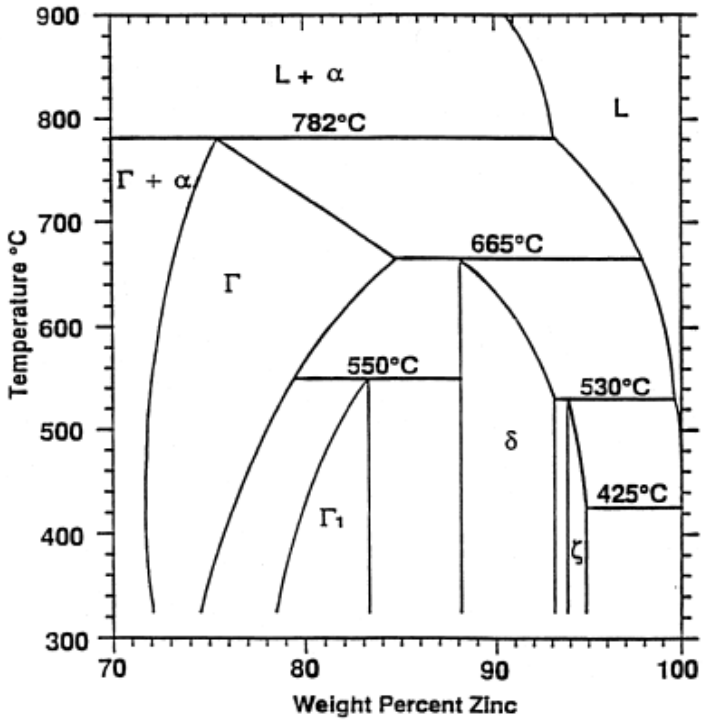

Figure 2-2: Alloy phases at high zinc % in the Fe-Zn binary phase diagram (Marder 2000)

Upon examining the Fe-Zn binary phase diagram illustrated in Figure 2-2, four intermetallic phases with varying atomic percent of zinc are identified. They are zeta (ξ), delta (δ), gamma-1 (Γ_1), and gamma (Γ). These four phases form different layers in a GA coating and are likely to form in the coating of the HAZ after laser welding galvanized steel. Table 2-1 presents a summary of their formulae and the atomic percentage of iron (Dionne 2006). In Yadav's experiment (2007), it was confirmed that a coating with alloy phases has a lower corrosion rate than that of a pure galvanized zinc coating. The alloy layers are able to offer protection to both the steel substrate and increase corrosion resistance. Therefore, it is possible for Fe-Zn intermetallic phases to lower the corrosion rate in the HAZ and prolong the overall life of welded galvanized steel.

Table 2-1: Formulae and properties of Fe-Zn alloy phases (Marder 2000; Dionne 2006)

Phase	Formula	Fe Content at. %	Peritectic Melting Point	Crystal Structure
Eta (η)	Zn	0.03%	420°C	Hexagonal
Zeta (ξ)	$FeZn_{13}$	5.9 ~ 7.1%	530°C	Monoclinic
Delta (δ)	$FeZn_{10}$	8.1 ~ 13.2%	672°C	Hexagonal
Gamma-1 (Γ_1)	Fe_5Zn_{21}	18.9 ~ 24.0%	550°C	Cubic
Gamma (Γ)	Fe_3Zn_{10}	18.0 ~ 31.0%	782°C	Cubic

Research shows that by annealing hot-dip galvanized coatings to produce galvannealed coatings, the corrosion rate can be substantially decreased (Zhang 1996). In acidic environments, the iron-zinc intermetallic phases formed during hot-dip galvanizing is 30% more corrosion resistant than pure zinc coatings as a result of an increase in the iron content in the zinc coating during diffusion which extends the life of the coating (Porter 1991). By applying heat treatment to hot-dip galvanized sheet, Hadden (1952) has shown that a coating with as much iron content as 20% is capable of achieving a life more than triple than that of a pure zinc coating in atmospheric conditions. In a similar experiment, Campbell et al. (1965) also confirmed that having more than 15% iron in the coating can result in a longer life for specimens exposed in an industrial setting.

Unfortunately, the effect of heat input in the zinc coating can also generate defects since the growth of Fe-Zn alloy phases can cause detrimental cracks. Reumont et al. (2001) suggest that great differences of linear thermal expansion coefficients exist between iron and the various Fe-Zn phases which leads to the development of large stresses and ultimately cracks in the coating.

2.3 Weld Microstructure

Even though the emphasis of this work was focused on the changes and performance of the galvanized coating after laser welding and stretch forming, it is important to recognize the

heterogeneity of the microstructure in the fusion zone and heat affected zone due to welding and their potential to influence the corrosion rate. It is possible that different weld microstructures can have varying corrosion resistance to rust. Furthermore, it would be valuable to investigate how residual stresses influence corrosion.

By examining the behaviour of four microstructures commonly found after welding low carbon steels namely, ferrite, pearlite, bainite and martensite, in 3.5% NaCl solution, Sephton and Pistorius (2000) reported corrosion potentials in the range of -0.65 V_{SCE}. They found negligible potential differences and galvanic interaction between the different microstructures. However, from their experiment, they suggest that the fusion line area is particularly vulnerable to localized corrosion relative to the HAZ.

2.4 Deforming Galvanized Steel

One way of evaluating how formable galvanized sheets are when subjected to stamping or stretching is by the limiting dome height (LDH) test. This test was developed as a laboratory simulation where a hemispherical punch deforms a sheet metal that is tightly clamped between dies by moving towards the sheet in the out-of-plane direction (Sreenivasan 2007). Figure 2-3 depicts the die and setup of the LDH test. By varying the width of the test specimens, LDH in uniaxial, plane and biaxial strain conditions can be produced. Since a significant portion of stamping failures occurs close to plane-strain conditions, the LDH test is a suitable tool that determines the formability of steel sheets until the onset of necking or failure.

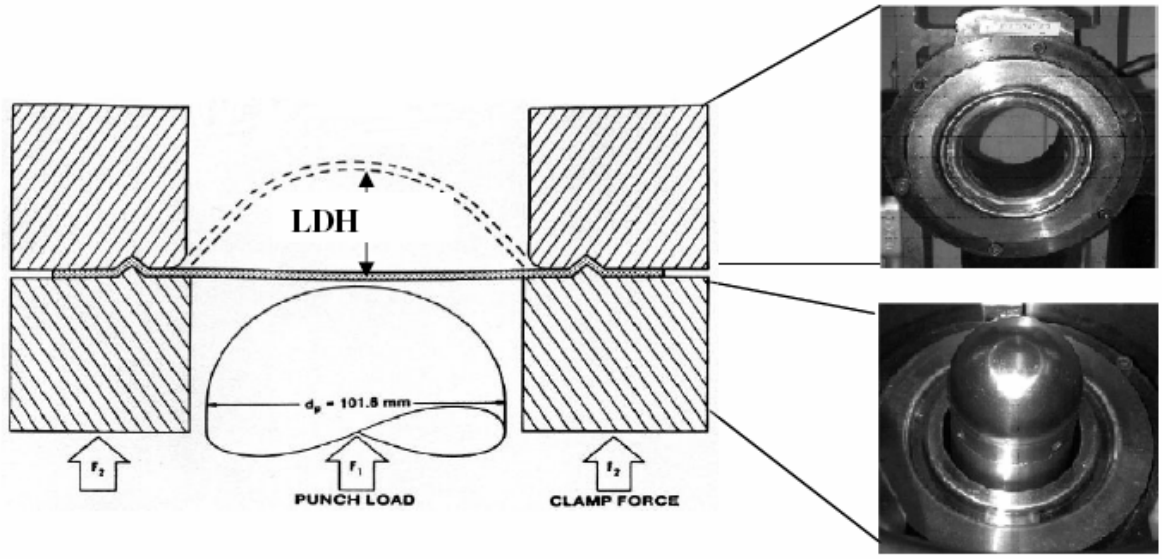

Figure 2-3: LDH setup and die geometry (Sreenivasan 2007)

Compared to uniaxial and plane strain conditions, biaxial strain causes not only the most deformation but also the most delamination to HDG steel sheets (Vagge, Raja et al. 2007). Research shows that polarization resistance is decreased with higher effective strain (Raja, Panday et al. 2006). Since corrosion rates are inverse proportional to polarization resistance (Stern and Geary 1957), higher strains would lead to higher corrosion rates.

Gupta and Kumar (2006) demonstrated that under plane strain and biaxial stretching conditions, the LDH test results of welded galvanized IF sheets were inferior to uncoated sheets. It is suspected that the formation of brittle Fe-Zn intermetallics may have been the cause of the observed decrease in formability. However, as the coating thickness increased, they observed a reduction in the coefficient of friction at the punch–sheet interface resulting in a slight increase in the LDH of galvanized IF sheets. In addition, they have observed two peak strains in the longitudinal direction. The maximum strain along the weld was found to be near 20 mm from the centre of the dome, termed the pole, on a single thickness blank. Gupta and Kumar's research (2006) also showed that when welded IF steel sheets were subjected to LDH tests, the height of the dome was close to that of the unwelded ones. Therefore, the influence of welding on IF steel LDH can be considered to be

negligible. In the case of HSLA, Sreenivasan (2007) reported a small difference in LDH between welded and base metal samples and concluded a minor influence of welding on the formability of HSLA.

General considerations in deforming galvanized steel are three fold. Firstly, the specimen surface area is increased after deformation by LDH. Secondly, deformation leads to thinning of the coating. Lastly, cracks are produced in the coating that exposes the steel substrate to the environment. Therefore, an increase in deformation results in widening of the exposed weld and substrate, increased surface area, and generation of cracks. In addition, the coating thickness is reduced due to stretching. These factors are the cause of an increase in corrosion rate of deformed HDG steel as observed by Fedrizzi and Bonora (1993).

2.5 General Corrosion Properties of Zinc and Iron

Zinc and its alloys are some of the most corrosion resistance materials. This is due to their ability to form protective layers that cover the metal surface (Porter 1991). These protective layers are typically oxide, hydroxide or carbonate films that are very adherent to the metal surface and can be insoluble in solution. Corrosion of zinc increases from immersion in hard water, then in sea water; soft water is the most corrosive (Slunder and Boyd 1983). Upon contact with water or immersed in solution, zinc dissolves readily and forms a film of corrosion products on the surface. The corrosion film is particularly stable in near neutral pH solutions but will dissolve in strong acidic or alkaline solutions (Slunder and Boyd 1983). In addition, the corrosion rate of zinc is especially low in near neutral pH values but can increase in either acidic or alkaline environments (Porter 1991). In the presence of sodium chloride in the solution, the corrosion rate of iron increases to a maximum at about 3% NaCl, which is the concentration of seawater, and then decreases with greater amounts (Uhlig and Revie 2008). Under atmospheric conditions, high moisture content or condensation on the metal surface may cause zinc hydroxide to form. This film is then likely to react with carbon dioxide to form insoluble zinc carbonate that shields zinc from the outside environment. Thus, zinc carbonate is very protective and is responsible for the excellent corrosion resistance of zinc in the atmosphere (Porter 1991).

Important factors that may affect the rate of zinc corrosion include temperature, humidity, and the frequency and duration of moisture contact also known as time of wetness (TOW) (Slunder and Boyd 1983). With a rise in temperature, zinc exhibits an increase in corrosion rate. For pure zinc immersed in aerated distilled water, the corrosion rate reaches a maximum at about 65°C and then decreases drastically with higher temperatures. The reason for this change is due to the transformation of the corrosion film from a gelatinous adherent type to a non-adherent granular type (Slunder and Boyd 1983). Zinc corrosion increases linearly with increasing humidity as a result of condensation on the metal surface. By increasing the TOW, zinc corrosion rate can also increase significantly. This is commonly applied in cyclic corrosion tests in order to achieve accelerated results. Depending on the degree of inclination of the exposed surface in the environment, the corrosion rate can differ considerably.

Another notable finding is that when zinc coated steel is immersed in water at temperatures near 70°C, a reversal of polarity occurs for the zinc potential where the zinc coating suddenly becomes cathodic to the steel substrate (Slunder and Boyd 1983). Berndsen et al. (2003) were able to apply this property in their etching technique to reveal the microstructure of zinc coated steel. Further, it is also possible for polarity reversal to occur even at room temperature in the presence of bicarbonate in the solution with as little as 600 ppm (Zhang 1996). However, it was observed that with approx. 20 ppm of calcium or sodium salts, the original polarity for the zinc-iron couple can be immediately restored (Zhang 1996).

Corrosion attack on zinc can be suppressed in a few ways. By adding magnesium and calcium ions in solution, the weight loss of zinc can be significantly reduced (Prosek, Thierry et al. 2007). Various amounts of minerals in hard water can impede corrosion by forming protective scales on the zinc surface. In general, the stability, adherence, and compactness of the corrosion products can affect the corrosion resistance thereby influence the corrosion rate of zinc coatings (Zhang 1996).

2.5.1 Corrosion Thermodynamics and Kinetics

To predict the electrochemical reactions, both anodic and cathodic, of a metal in solution, the potential vs. pH, or Pourbaix diagrams, by whom they were first constructed, can be very useful. This

is analogous to examining phase diagrams in material science. Figure 2-4a and 2-4b illustrate the stable phases of zinc and iron respectively in aqueous solution at varying potentials versus the standard hydrogen electrode (SHE), and pH ranges. Thus, it can be understood why zinc and iron is thermodynamically unstable in water at moderate potentials and dissolves over the entire pH range. At low pH values, Zn^{2+} ions will saturate in solution while in near neutral or higher pH values, hydroxide films can cover the zinc surface. Similarly, Fe^{2+} ions are generated at low pH values while Fe_3O_4 forms readily in higher pH solutions. Typically zinc dissolves with two valence electrons at almost 100% faradaic efficiency in common solutions such as NaCl and KOH (Zhang 1996). This is identical with the dissolution of iron. The anodic reactions for the two metals are as follows:

$$Zn \rightarrow Zn^{2+} + 2e^{-} \qquad \text{(Eq. 2-1)}$$

$$Fe \rightarrow Fe^{2+} + 2e^{-} \qquad \text{(Eq. 2-2)}$$

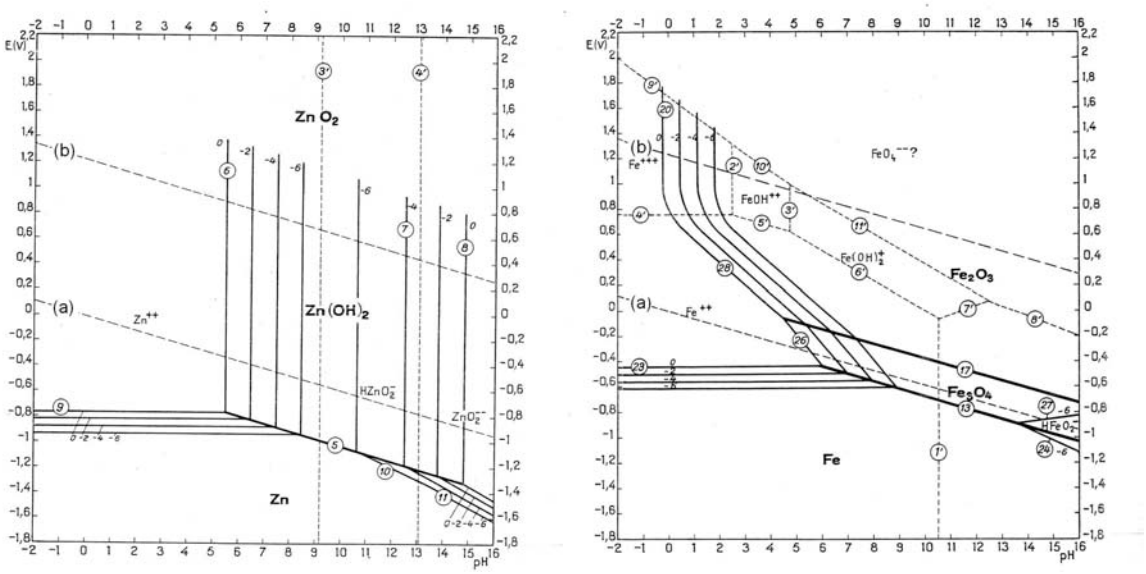

a) b)

Figure 2-4: Potential-pH equilibrium diagram of a) zinc and b) iron in aqueous solution (Pourbaix 1996)

In neutral solutions, zinc dissolution can occur in two charge transfer-steps where the second step is the rate determining step (Zhang 1996):

$$Zn \rightarrow Zn^{+} + e^{-} \quad \text{(Eq. 2-3)}$$

$$Zn^{+} \rightarrow Zn^{2+} + e^{-} \text{ (r.d.s)} \quad \text{(Eq. 2-4)}$$

The dashed lines of (a) and (b) divide the Pourbaix diagram into three regions and indicate the stability of hydrogen, water, and oxygen. At potential ranges below line (a), hydrogen evolution is thermodynamically stable; therefore, water will be decomposed to form hydrogen and hydroxide ions. Depending on the pH, the cathodic reaction taking place on the zinc or iron surface would follow Eq. 2-5 if the solution is acidic or Eq. 2-6 if the solution is neutral or alkaline.

$$2H^{+} + 2e^{-} \rightarrow H_2 \quad \text{(Eq. 2-5)}$$

$$2H_2O + 2e^{-} \rightarrow H_2 + 2(OH)^{-} \quad \text{(Eq. 2-6)}$$

At moderate potentials between lines (a) and (b), water becomes the stable phase and oxygen will be decomposed through the cathodic reactions of Eq. 2-7 and 2-8 in acid and in neutral or alkaline solutions respectively.

$$O_2 + 4H^{+} + 4e^{-} \rightarrow 2H_2O \quad \text{(Eq. 2-7)}$$

$$O_2 + 2H_2O + 4e^{-} \rightarrow 4(OH)^{-} \quad \text{(Eq. 2-8)}$$

While the potential at which zinc dissolves in neutral pH solution is about -0.76 V with respect to the standard hydrogen electrode, it is near -0.44 V for iron.

While it is essential to understand the electrochemical reactions that govern the corrosion of metals in the environment, in practice, the corrosion rates are often of greater consideration. For iron and steel immersed aqueous solutions, it is found that the diffusion of oxygen to the metal surface and through a layer of hydrous ferrous oxide generally controls the corrosion rate (Uhlig and Revie 2008). Similarly, the corrosion rate of zinc is also controlled by the diffusion of oxygen through the film of zinc corrosion products at moderate potentials (Slunder and Boyd 1983).

2.5.2 Corrosion Potential (E_{corr})

The corrosion potential, also known as open circuit potential, is the value at which a metal is in equilibrium with the electrolyte. At more positive potentials, the metal corrodes freely in the electrolyte whereas at more negative potentials the metal is immune to corrosion. This value is not measured absolutely but rather as a potential difference with respect to a reference electrode such as the saturated calomel electrode(SCE). Researches have found the corrosion potential for zinc immersed in NaCl solution to be near -1.05 V_{SCE} (-0.81 V_{SHE}) (El-Mahdy, Nishikata et al. 2000; Yadav, Nishikata et al. 2004; Prosek, Thierry et al. 2007). For IF steel in NaCl solution, the corrosion potential is found to be near -0.55 V_{SCE} (-0.31 V_{SHE}). The corrosion potential of zinc may be considered as a degree of protectiveness of the coating. As the corrosion potential of zinc increases positively, zinc loses its ability to protect the exposed steel slowly. Therefore substantial protection against corrosion can be offered if the potential of steel is lowered by about 200 mV below its free corrosion potential (Zhang and Valeriote 1993). For carbon steels under total immersion conditions in NaCl solution, Baldwin et al. (1995) found that a protection potential of about -0.72 V_{SCE} would significantly reduce the corrosion rate. Under the recommended practice by a NACE[i] standard, the criterion of cathodic protection on a submerged steel surface should be at least -0.78 V_{SCE} or more negative (NACE RP0388-90). That is, at values close to -0.78 V_{SCE}, steel may be partially protected by the zinc coating. Once the corrosion potential becomes more positive than -0.78 V_{SCE}, steel is no longer protected and begins to corrode.

In the presence of different Fe-Zn alloy phases in the coating, various corrosion potentials may exist. Using a technique called galvanostatic polarization, whereby each Fe-Zn alloy phases were removed individually, Fedrizzi and Bonora (1993) obtained potential plateaus at -0.87 V_{SCE}, -0.82 V_{SCE}, and -0.77 V_{SCE} for the zeta (ξ), delta (δ), and gamma (Γ) phase respectively of an alloy coating in NaCl solution. Very close potential values were also reported by Queiroz and Costa (2007) who used the coulometric stripping technique, whereby an applied anodic current density selectively dissolves the alloy phases and potential plateaus were obtained, to characterize the alloy phases in a galvannealed coating. It would be of interest to observe whether these potentials can be identified during electrochemical monitoring of welded coupons.

---

[i] National Association of Corrosion Engineers

2.5.3 Galvanic Couple and Protection Distance

When two dissimilar metals such as zinc and iron are placed in contact and completes an electrical circuit, a galvanic couple is formed. The potential difference between the two metals provides the driving force for galvanic corrosion. Consequently, the corrosion potential of the more active zinc is increased while that of the more noble iron is decreased. The resulting potential of the galvanic couple always falls in between the value of the two. Furthermore, the corrosion rate of zinc rises while that of the more noble iron drops. This sacrificial action of zinc is the basis of cathodic protection for iron.

Under immersed conditions, the ability of zinc to cathodically protect steel in solution over a distance is termed the "throwing power". The degree of protection afforded to steel is directly related to the conductivity of the solution (Uhlig 1955). Zhang and Valeriote (1993) agree that conductivity is important in transporting zinc ions in solution in order to offer its protection. Zhang (2000) examined how various types of environments affected the protection distance (PD) of zinc over iron and observed that in chloride containing bulk solutions, zinc was capable of protecting steel at a greater distance than in a thin layer of solution or in distilled water. He also found that when the ASTM B117 salt spray test was used, the PD decreased. With wet-humid-dry conditions, the PD was almost non-existent when the wet stage was removed leaving only the humid and dry stages. More importantly, the larger the distance separated between zinc and steel, the shorter the PD. In the experiment by Baldwin et al. (1995), it was found that with a protection potential of about -0.72 V_{SCE}, zinc was able to protect steel over a distance of 48 mm after 1 hour in NaCl solution. Even though the PD decreased over time, it suggests the possibility that a weld with a total exposed width of 96 mm can be protected by the adjacent galvanized coating.

On the corrosion surface of a zinc-steel couple exposed to atmospheric conditions, five regions are distinguished across the interface (Zhang 2000): on the zinc surface, it is general corrosion; at the zinc-steel interface, a very narrow region of galvanic corrosion is observed; across the steel surface, a full cathodic protected region is identified followed by partial cathodic protected region and then general corrosion of steel. With increasing distance from the interface, the density and size of rust pits increased, eventually covering the entire surface of exposed steel.

2.5.4 Corrosion Products of Zinc and Iron

For galvanized steel on autobodies, it is essential to understand how corrosion products evolve under atmospheric conditions or when subjected to moisture and humidity. The atmospheric environment is often divided into different types, namely, rural, urban, industrial and marine. Each type of atmospheric environment can cause zinc to form different compounds. In general, oxides, hydroxides, and carbonates are the most common corrosion products of zinc and have a very low solubility in water (Porter 1991). In fresh waters, zinc oxide, ZnO and zinc hydroxide, $Zn(OH)_2$ are commonly found. Initially, zinc hydroxides are formed when dissolved zinc species react with hydroxyls in solution.

$$Zn^{2+} + 2(OH)^- \rightarrow Zn(OH)_2 \qquad \text{(Eq. 2-9)}$$

$$Zn^{2+} + H_2O \rightarrow Zn(OH)^+ + H^+ \qquad \text{(Eq. 2-10)}$$

$$Zn(OH)^+ + OH^- \rightarrow Zn(OH)_2 \qquad \text{(Eq. 2-11)}$$

Hydroxide precipitates on the zinc surface may gradually transform into zinc oxides by the reaction below

$$Zn(OH)_2 \rightarrow ZnO + H_2O \qquad \text{(Eq. 2-12)}$$

As mentioned earlier, one of the most corrosion resistant films is zinc carbonate. It is responsible for the protection of zinc under atmospheric conditions. When the solution pH is less than seven, zinc carbonate is the stable corrosion product. On the other hand, when the pH value is greater than seven, zinc hydroxide becomes the stable phase (Slunder and Boyd 1983). If calcium cations are present, than calcium carbonate may also form. With atmospheric exposure, zinc hydroxide would frequently develop into a thin layer of porous zinc oxide. However, when the environment contains chlorides, the corrosion process generally leads to the formation of zinc hydroxy chloride (ZHC), also known as simonkolleite, by the equation below. In some publications, $Zn_5(OH)_8Cl_2$ may be seen as the alternate formula.

$$4Zn^{2+} + 8OH^- + ZnCl_2(aq) \rightarrow ZnCl_2[Zn(OH)_2]_4 \qquad \text{(Eq. 2-13)}$$

Bernard et al. (1995) reported that in the presence of chlorides and large pores in the coating, Cl^- ions can react directly with zinc cations to form ZHC. In several studies, it has been reported that

the more ZHC there are in the corrosion product, the higher the corrosion resistance of zinc (Zhang 1996).

At room temperature the corrosion products that form are typically gelatinous and very adherent but as temperature increases to 75°C, the corrosion products become granular, and non-adherent to the zinc surface (Zhang 1996). Further increase in temperature will cause the corrosion products to be more compact and adherent on the zinc surface.

Ohtsuka and Matsuda's work (2003) showed that when the relative humidity (RH) is below 80%, a zinc plate exposed to 3 wt% NaCl solution was covered with ZnO as the main corrosion product; however, when the RH reaches over 80%, an aqueous $ZnCl_2$ layer first forms on the zinc plate then precipitation of ZHC is promoted from a concentrated solution of $ZnCl_2$. Hence, Ohtsuka and Matsuda proposed that a lack of sufficient concentration of $ZnCl_2$ and RH level would prevent the formation of ZHC. In addition, if a ZnO layer was formed first on the zinc surface, the formation of a concentrated $ZnCl_2$ layer may be retarded.

It is generally agreed that ZHC is likely to form with a high concentration of chlorides at low pH values (Zhu, Persson et al. 2000; Prosek, Thierry et al. 2007). But when the zinc surface is confined inside crevices such as hem flanges on the autobody, the corrosion mechanism differs from that in an open atmospheric environment. Zhu et al's study (2000) showed that ZHC was the dominant corrosion product of zinc on open surfaces while zinc carbonate hydroxide, also known as hydrozincite, $[ZnCO_3]_2[Zn(OH)_2]_3$ was predominant on zinc under confined conditions. However, with an increase in the concentration of NaCl solution, the corrosion product changed from hydrozincite to ZHC.

Under wet-dry cycles, Yadav et al. (2004) reported a rise in intensity of the zinc corrosion products with an increase in number of cycles. They found that the corrosion products formed on a galvanized steel sample were very similar to those found on a pure zinc sample. More importantly, the build up of zinc corrosion products, sometimes referred to as white rust, prolong the time of wetness by retaining more moisture on the zinc surface, thus retarding the drying process.

The corrosion products of low (or ultra low) carbon steel steels such as HSLA and IF typically include iron oxides, FeO, Fe_2O3, Fe_3O_4, and iron oxide hydroxide, FeO(OH). It is also

possible for the alloying elements in the steel chemistry to oxidize and influence the formation of corrosion products. Oh et al. (1998) have successfully characterized different phases of iron oxides, iron hydroxides, and iron oxide hydroxides in their study using Raman spectroscopy on the corrosion layers on steel. In the case of Fe-Zn alloys, Hadden (1952) observed a yellow appearance on the corroded surface of heat treated galvanized steel.

2.5.4.1 X-Ray Diffraction (XRD)

Among the powerful analytical tools, the use of XRD in determining crystal structures or identifying phases has been the central application. However, it has gained increasing popularity in revealing compounds or corrosion products such as those from iron and zinc. A brief explanation of the technique is provided here.

When a beam of X-ray with a known wavelength contacts a solid material with a specific crystal structure, diffraction can occur under the conditions that the atomic spacing or the distance between two planes of atoms is similar to that of the beam wavelength and that the wave motion of the X-rays can be interfered (Cullity 1978). Upon satisfying particular angles of incidence, known as Bragg's law, then the X-rays will be scattered. If the scattered rays are in phase, they will reinforce each other to cause a constructive interference or a diffracted beam. Those angles that do not satisfy Bragg's law will scatter X-rays out of phase cancel out each other and cause destructive interference in which no diffraction will be detected.

The galvanized steels in El-Mahdy's (2000) wet-dry cycles in the presence of chlorides revealed ZnO, ZHC, $Zn_5(CO_3)_2(OH)_6$, α-FeOOH, β-FeOOH, and δ-FeOOH as the corrosion products. XRD diffraction patterns were also obtained by Yadav et al. (2007) that revealed zeta (ξ), delta (δ), and gamma (Γ) phases in the galvanized coating.

2.5.4.2 Raman Spectroscopy (RS)

Raman Spectroscopy is another versatile analytical tool that examines vibrational changes in a specimen by the scattering of monochromatic light, usually from a laser in the visible, near infrared or near ultraviolet range (Skoog, Holler et al. 1997). This technique is capable of analyzing organic and inorganic substances in powder, solid, liquid, and gas form. Furthermore, samples may be immersed in water or solution for analysis. In recent years, RS has gained popularity in materials engineering for phase identification. Similar to XRD, results of RS peaks or Raman shifts can be compared with publications or databases. The Raman spectra of corrosion products build up on pure zinc after immersion in NaCl solution have been identified by Bernard et al. (1995). Their results were close with those found by Thierry et al. (1991) and are summarized in Table 2-2.

Table 2-2: Raman shifts of zinc corrosion products from different references

Authors	Raman Shift (cm^{-1})		
	ZHC	$ZnCO_3$	ZnO
Bernard, Hugot-Le Goff, Phillips	257, 397, 736, 715, 3449, 3483	385, 740, 1060, 1370, 1540	330, 440, 570, 1080, 1135
Thierry, Massinon, Hugot-Le-Goff	210, 256, 399, 3453, 3484	140, 216, 383, 730, 1063	100, 330, 375, 440, 540-580

2.6 Electrochemical Techniques

Electrochemical techniques are often conducted in laboratories under controlled environments. They offer rapid determination of the corrosion properties of a sample at a particular instance in time. Even though the long term corrosion rates may not be precisely reflected, the observed data are nonetheless useful in predicting the long term behaviour of the sample.

2.6.1 Linear Polarization Resistance (LPR)

LPR is an effective electrochemical technique widely used to determine the instantaneous corrosion rate of a system in aqueous solutions. The non-destructive nature and short application time are two of the advantages making it more appealing than other techniques. During an LPR measurement, a constant overpotential is applied to the specimen or the working electrode (WE) which is measured by the reference electrode (RE). It was observed that within an overpotential of ±20 mV of the specimen's E_{corr}, the specimen surface is hardly disturbed and the natural corrosion process is unaffected. It was found that a linear relationship existed between the corrosion current and the overpotential (Stern and Geary 1957). In addition, the linearity in this region is inversely proportional to the corrosion rate of the specimen. The resulting current response measured between the specimen and the counter electrode (CE) is used to calculate the polarization resistance, Rp, of the specimen using the following equation:

$$R_p = \frac{\Delta E}{\Delta I} \qquad \text{(Eq. 2-14)}$$

where ΔE and ΔI are the difference in overpotential and corrosion current respectively.

With the aid of the Stern-Geary equation (1957), the corrosion current, I_{corr}, can be related to the polarization resistance in the equation below:

$$I_{corr} = \frac{B}{R_p} = \frac{\beta_a \cdot \beta_c}{2.3 \cdot (\beta_a + \beta_c) \cdot R_p} \qquad \text{(Eq. 2-15)}$$

where B is the Stern-Geary constant and β_a and β_c are the anodic and cathodic Tafel constants respectively.

Tafel constants must be determined empirically and few values have been found for zinc in NaCl solutions. Reported values of β_a varied between 0.04 ~ 0.06 V while β_c approached infinite for zinc in NaCl solutions (Zhang 1996; Barranco, Feliu Jr. et al. 2004). Stern showed that for Tafel constants ranging between 0.06 ~ 0.12 V, the calculated corrosion rate is within reasonable error. Therefore, when Tafel constants are unknown or difficult to obtain, the value of $\beta_a = \beta_c = 0.1$ may be

applied and the constant minor error associated with the result will still be within experimental scatter.

Finally, the weight loss, w, in grams per unit area, of the zinc coating can be determined using Faraday's Law and equation below. Alternately, the depth loss, D, of the coating can be presented by dividing the equation below by the density, ρ, of zinc.

$$w = \frac{I_{corr} \cdot t \cdot M}{A \cdot n \cdot F} \qquad \text{(Eq. 2-16)}$$

where:

I_{corr} = corrosion current (A)

t = time (s)

M = atomic weight (g/mol)

A = corroding area (cm^2)

n = number of equivalents exchanged

F = Faraday's number (96,500 coulombs/mol of equivalent)

2.7 Accelerated Laboratory Tests

In accelerated corrosion testing, the salt spray test (ASTM B117) is one of the oldest standardized and widest used method. However, the continuous wet condition from this test was notorious for its poor correlation to weathering conditions and actual corrosion performance in service. More importantly, the salt spray test did not reflect corrosion in automotive environments. In fact, it was found that the salt spray test was one of the poorest methods for galvanized steel (Moran, Ziman et al. 1995). Therefore, it has been the interest of automotive engineers and steel makers to develop an improved standardized test to better correlate results from proving grounds, outdoor exposures and on-vehicle

exposures. Since then, cyclic laboratory tests particularly used in the automotive industry have proven to give improved reproducibility and repeatability.

The acceleration of corrosion is based on the synergistic effect of alternating wet and dry cycles in the laboratory environment. In recent years, the Japanese CCT-IV, and the GM standard GM 9540P-B are among the well known cyclic laboratory test standards that correlate realistically to long term field performance (Roudabush, McCune et al. 1995). In Roudabush et al.'s design of experiments, they tested parameters such as salt composition, NaCl concentration, temperature and humidity of the humid and dry stages, which lead to further modifications and development of a cyclic corrosion test of automotive steel sheets. Together with the American Iron and Steel Institute's (AISI) Task Force on automotive corrosion, the Society of Automotive Engineer's (SAE) Automotive Corrosion and Prevention Committee (ACAP) developed the SAE J2334 standard that proved to have the best correlation between accelerated laboratory tests on zinc coated steels and long term on-vehicle testing (Repp 2002). Despite the fact that accelerated laboratory tests do not necessarily simulate natural atmospheric conditions, experimental results can reasonably predict corrosion rates after long exposures. An early study on the corrosion performance of TWBs was conducted by Simpson et al. (1998) which included both galvanized and galvannealed samples as well as laser welded and mash-seam welded blanks. They found that laser welded blanks outperformed mash-seam welded blanks and galvannealed coatings had superior corrosion resistance than galvanized coatings after 80 cycles of SAE J2334. Using both ASTM B117 and SAE J2334, Bandyopadhyay et al. (2006) concluded that galvannealed coatings show superb corrosion and red rust resistance and are excellent materials for automakers.

During the wetting and drying cycles, test specimens experience a change in the environment from exposure to bulk solution to thin layer electrolyte as they dry. The time of wetness for galvanized coatings starts when the relative humidity exceeds 86% (Zhang 1996). Zhang pointed out that because diffusion of oxygen is easy through a thin layer of electrolyte, it translates into a higher corrosion rate than that in bulk solution of NaCl. Researches in Zhu's study (Zhu, Persson et al. 2000) suggest that the corrosion rate of zinc is higher on confined surfaces than on open surfaces under similar conditions. The high corrosion rate of zinc in crevices is attributed to the restricted diffusion of oxygen, slow oxygen reduction, and higher concentration of chlorides which favoured the formation of ZHC. Further, the corrosion rate for both confined and open surfaces increased

considerably as the drying time decreased. Contrarily, Yadav et al. (2004) suggests that corrosion tends to increase as the drying time increases. This is because while solution dries on the specimen surface, the zinc coating loses its ability to dissolve into ions and supply sufficient galvanic current to defect sites for cathodic protection. Thus, the galvanic protection will be effective only when the surface is sufficiently wet. Other than the corrosion rate, the morphology and compactness of corrosion products will also be significantly influenced by the duration of the wet-dry cycles as well as the frequency of the cycles.

While the weight loss of zinc decreased with deposits of calcium chloride, the opposite trend was observed when the deposits were on carbon steel (Prosek, Thierry et al. 2007). Hence, it is possible for calcium cations in the salt solution to lower the corrosion rate on the zinc coating by forming protective corrosion products.

CHAPTER 3
EXPERIMENTAL PROCEDURE

3.1 Materials

Steel sheets used in this study included both the conventional IF and the popular HSLA. Each steel grade had two thicknesses: 0.77 mm and 1.77 mm and were hot-dip galvanized in a continuous production line with a nominal coating weight of 80 g/m^2 (~ 11.5 μm) for the IF steel and 75 g/m^2 (~ 10.5 μm) for the HSLA steel. The average coating weights are given in Table 3-1. The exact steel chemical compositions for IF steel are given in Table 3-2 and 3-3. Likewise the properties for HSLA steel are presented in Table 3-4 and 3-5.

Table 3-1: Average coating weight of experimental materials

	IF	HSLA
0.77 mm	80 g/m^2	77 g/m^2
1.77 mm	82 g/m^2	75 g/m^2

Table 3-2: Chemical composition of 0.77mm IF steel (wt.%)

C	Si	Mn	P	S	Ni
0.002	0.006	0.180	0.009	0.007	0.025
Cr	**Mo**	**Cu**	**Al**	**Ti**	**Nb**
0.015	0.003	0.014	0.047	0.054	0.007

Table 3-3: Chemical composition of 1.77mm IF steel (wt.%)

C	Si	Mn	P	S	Ni
0.002	0.010	0.170	0.007	0.009	0.011
Cr	**Mo**	**Cu**	**Al**	**Ti**	**Nb**
0.036	0.003	0.041	0.046	0.046	0.009

Table 3-4: Chemical composition of 0.77mm HSLA steel (wt.%)

C	Si	Mn	P	S	Ni
0.060	0.227	0.624	0.006	0.004	0.013
Cr	**Mo**	**Cu**	**Al**	**Ti**	**Nb**
0.041	0.005	0.044	0.039	0.003	0.021

Table 3-5: Chemical composition of 1.77mm HSLA steel (wt.%)

C	Si	Mn	P	S	Ni
0.058	0.215	0.640	0.007	0.002	0.041
Cr	**Mo**	**Cu**	**Al**	**Ti**	**Nb**
0.071	0.014	0.121	0.038	0.014	0.022

3.2 Characterization of the Galvanized Coating after Welding

The effect of laser welding on the changes in the galvanized coating close to the weld was examined using a JEOL model JSM-6460, scanning electron microscope (SEM). In addition, elemental analysis was conducted using X-Ray energy dispersive spectroscopy (EDS).

The cross sections of both Nd:YAG and diode laser welded samples were mounted in epoxy resin, ground with silicon carbide paper from #320, #400, to #800 grid size. Polishing was then conducted using 3 μm and then 1 μm waterfree suspension with ethanol based lubricant. Prepared metallographic samples were etched in 0.5% alcoholic nitric acid at 75°C for 10~30 seconds prior to viewing under the SEM. Micrographs on the transformation of the zinc coating and growth of the Fe-Zn alloy phases are presented in the following chapter.

3.3 Electrochemical Test – LPR

One method of quantifying the corrosion performance is by electrochemical test. Both the open circuit potential and the current density were monitored over a period of 60 days. Only IF steel was

used in this setup. The LPR technique was performed using a Princeton Applied Research (PAR) potentiostat model PARSTAT 2263, interfaced with the PowerSuite software. In this test, three types of specimen were examined in solution: stripped, welded and deformed coupons. All three types of coupons having varying exposed widths and their respective corrosion rates were investigated. Preparation steps for each type of specimen are described in the following sections.

In the electrochemical cell, the immersed coupons were the working electrodes (WE) while the saturated calomel electrode (SCE) was employed as the reference electrode (RE). A graphite rod served as the counter electrode (CE). All potential values in this test and presented in the results chapter were measured with respect to the SCE unless otherwise specified. The electrolyte was 0.1 M NaCl solution prepared using reagent grade salt and distilled water. An example of the electrochemical cell is displayed in Figure 3-1 where coupons in triplicates from each variable and type stand upright on a platform that was made to accommodate the build up of corrosion products over time and to prevent corrosion products from covering the coupon surfaces. The cells are aerated through openings in the cover.

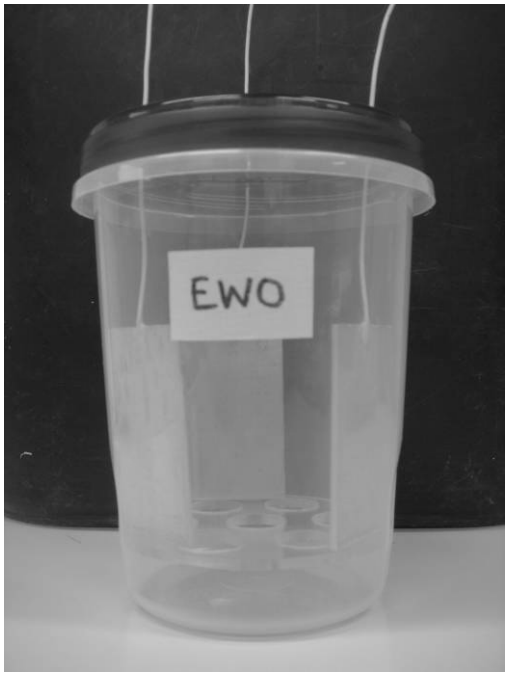

Figure 3-1: Sample corrosion cell with test coupons and wire connections

All test coupons are rectangles having a nominal size of 38.1 mm x 63.5 mm (1.5" x 2.5"). In order to facilitate electrochemical measurements, wires were spot welded onto the zinc coating beside the exposed region for all coupons and then epoxy coated. Similarly, all exposed edges were epoxy coated to induce corrosion on the front and back surfaces only of the coupons.

Typically in LPR, a constant potential of ±10~20 mV in the form of square waves are applied to the open circuit potential of the working electrodes. In this study, ±10 mV was used and held for 100 seconds and the resulting net current was directly measured. This ensured a linear relationship between the applied potential and the corrosion current. From the measured net current, the polarization resistance of the corroding coupons was determined. The corrosion current density was then determined using the Stern-Geary equation (1957). Finally, the zinc corrosion rate for each coupon was calculated with the aid of Faraday's Law.

3.4 Chemical Stripping

To simulate the exposed region of the underlying steel due to laser welding, the zinc coating on galvanized steel sheets was removed chemically using inhibited acid. First, the IF steel sheets were cut to the nominal size then both surfaces of the specimens were protected using masking tape leaving only widths of 0, 1, 3, 6 and 9 mm. The stripping solution was prepared by mixing 25 vol.% of hydrochloric acid (HCl) with deionized water and adding 1 g/L of hexamethyl tetramine. When the specimens were immersed in the stripping solution, the exposed or unprotected zinc coating dissolved vigorously while tiny bubbles of hydrogen formed. When all of the zinc had dissolved, the specimens were removed from the stripping solution showing varying widths of the exposed steel substrate. Fully prepared coupons are shown in Figure 3-2 with increasing exposed width from left to right. For the purpose of discussion, they are called "stripped coupons". In addition, to observe how differences in zinc surface area affect the corrosion rate, two more sets of coupons having an exposed width of 3 mm were also prepared. Figure 3-3 shows that while the narrow coupon has only half the nominal zinc surface area, the wide coupon has twice. These two sets of coupons are referred to as 3 mm(N) for narrow and 3 mm(W) for wide.

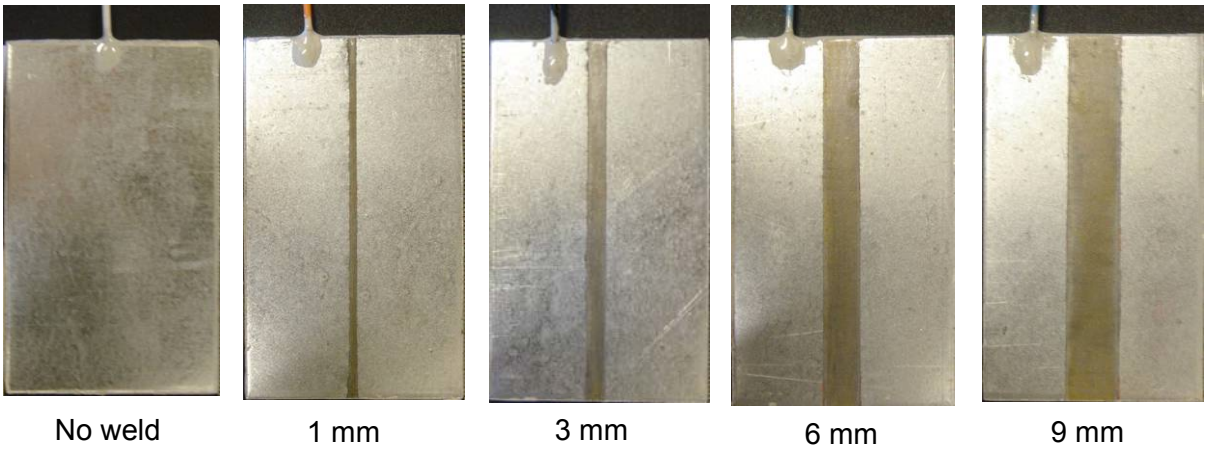

Figure 3-2: Prepared coupons showing specific exposed widths of the steel substrate by means of chemical stripping of the galvanized coating

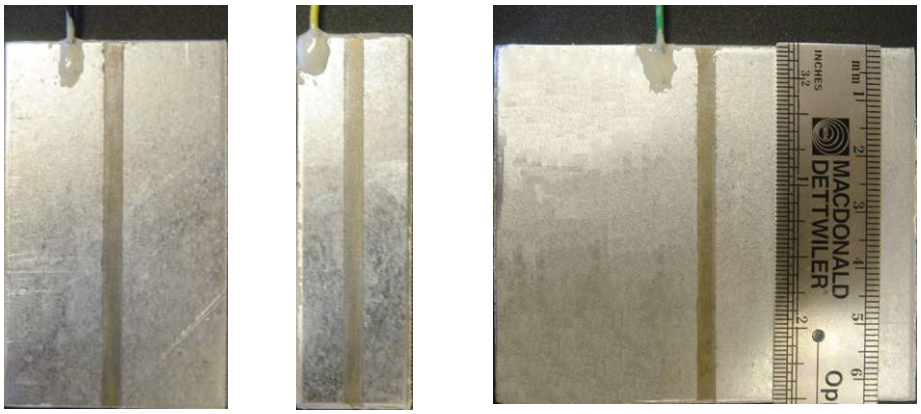

a) b) c)

Figure 3-3: Prepared coupons having a 3 mm exposed width and a) a nominal b) half the, and c) twice the, zinc surface area

3.5 Laser Welding

All welding conducted during the course of this work were bead-on-plate welds using two high power lasers: an Nd:YAG and a diode laser. The Nd:YAG laser is a Haas HL3006D having 3 kW of power that produces a keyhole type weld with very narrow fusion and heat affected zones. This system used fibre optics to deliver the beam onto the work piece.

Figure 3-4: Welding setup of Nuvonyx diode laser on a robot

For conduction type welding, a Nuvonyx ISL-4000L AlGaAs diode laser mounted on a Panasonic VR-16 welding robot shown in Figure 3-4 was employed. This high power diode laser has a power output of 4 kW, a rectangular beam of 12 mm x 0.9 mm and a wavelength of 800 nm (Nuvonyx 2001). Argon shielding gas was provided to the weld pool through a gas nozzle mounted on the diode laser head with a flow rate of 14 L/min (35 cfh). Table 3-6 illustrates the selected welding speeds optimized for complete penetration and the resulting exposed widths for IF steel.

Table 3-6: Optimized welding speeds for IF steel

IF	Laser	Welding Speed	Exposed Width
0.77 mm	**Nd:YAG**	4.8 m/min	1 mm
	Diode	2.25 m/min	3 mm
	Diode	1.50 m/min	5 mm
1.77 mm	**Nd:YAG**	2.4 m/min	1 mm
	Diode	0.45 m/min	6 mm
	Diode	0.30 m/min	9 mm

Table 3-7: Optimized welding speeds for HSLA steel

HSLA	Laser	Welding Speed	Exposed Width
0.77 mm	**Nd:YAG**	4.8 m/min	1 mm
	Diode	2.25 m/min	3 mm
	Diode	1.50 m/min	5 mm
1.77 mm	**Nd:YAG**	2.4 m/min	1 mm
	Diode	0.42 m/min	7 mm
	Diode	0.28 m/min	11 mm

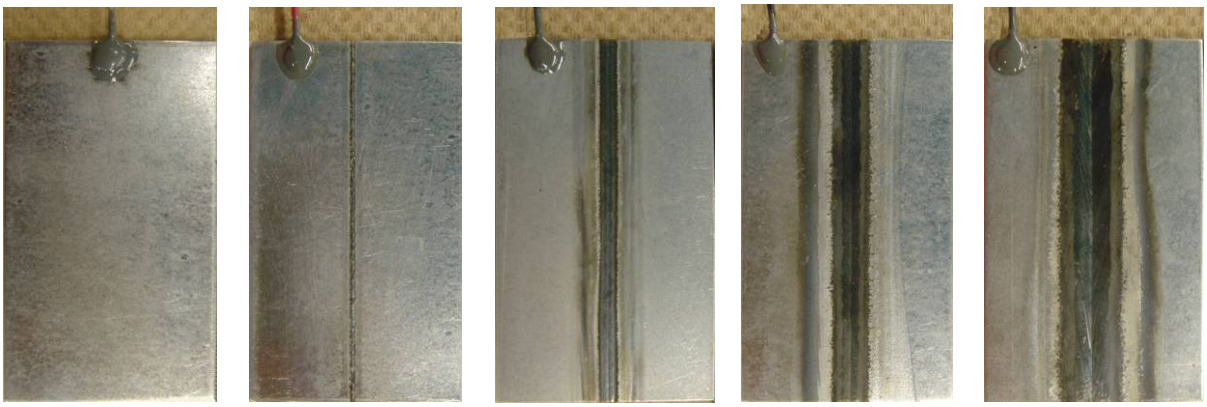

Figure 3-5: Prepared coupons having specific exposed widths after laser welding

Similarly, HSLA steel was welded using speeds given in Table 3-7. While IF coupons were tested in both continuous immersion and accelerated conditions, HSLA coupons were tested only in the accelerated test condition. After laser welding, IF coupons were cut into nominal size, prepared with wires and epoxy coated as previously described. Figure 3-5 shows the front view of fully prepared welded coupons.

3.6 Stretch Forming

Prior to limited dome height testing, square sheets of 200 mm x 200 mm (8" x 8") were first laser welded with the above mentioned speeds. Forming lubricant and 0.1mm polypropylene sheets were applied to the bottom surface of the welded specimens to reduce friction and effects from the punch. The welded square sheets were then inserted into the die shown in Figure 2-3 followed by raising the hemispherical punch slowly. For each welding speed, the welded sheet was stretch formed until necking occurs. The LDH was determined for both steels at different welding speeds and summarized in Table 3-8. It can be seen that with decreasing welding speeds, there was a slight decline in the LDH. This was caused by the laser heat input in which both FZ and the HAZ were broadened.

Table 3-8: LDH for welded IF and HSLA steel coupons

Thickness	Welding Speeds m/min	IF Steel LDH (mm)	HSLA Steel LDH (mm)
0.77	0	38	33
0.77	4.8	37	29.5
0.77	2.25	35	28
0.77	1.5	28.5	20.5
1.77	0	42	39
1.77	2.4	42	37
1.77	0.45	36	33
1.77	0.3	35	29

The actual heights used to stretch form the welded sheets were 80% of the LDH attained from the slowest welding speed for each thickness. Therefore, all welded sheets having the same thickness were stretch formed to the same height to achieve a constant biaxial strain. Table 3-9 presents the actual stretched height for both steels and thicknesses. This height represents the deformation that typical regions on a TWB might experience during stamping while at the same time significantly influences the galvanized coating

Table 3-9: Heights used for deformed coupons

Thickness	IF Steel Deformed Height (mm)	HSLA Steel Deformed Height (mm)
0.77	23	17
1.77	29	25

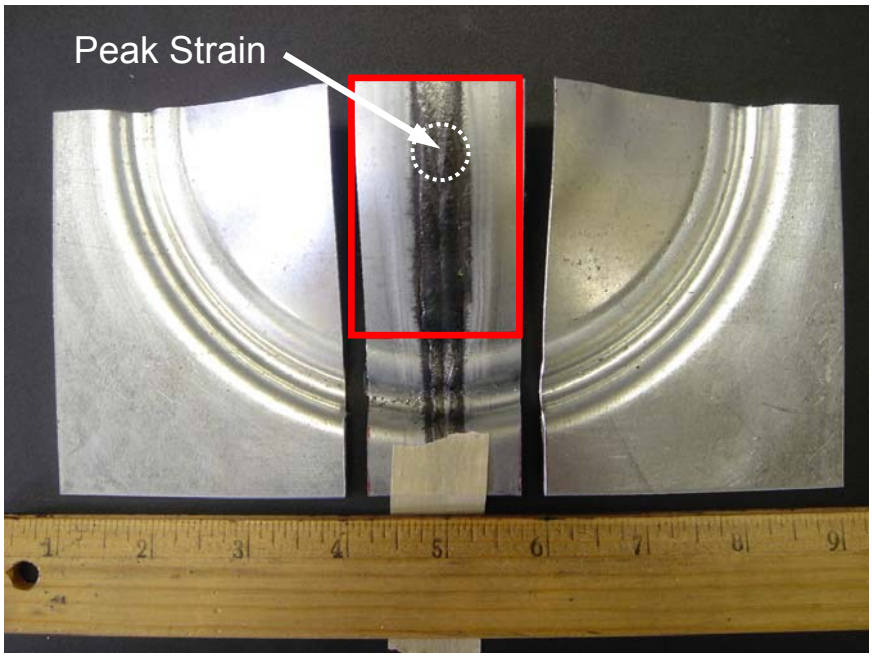

Figure 3-6: Sectioning of a biaxially strained specimen

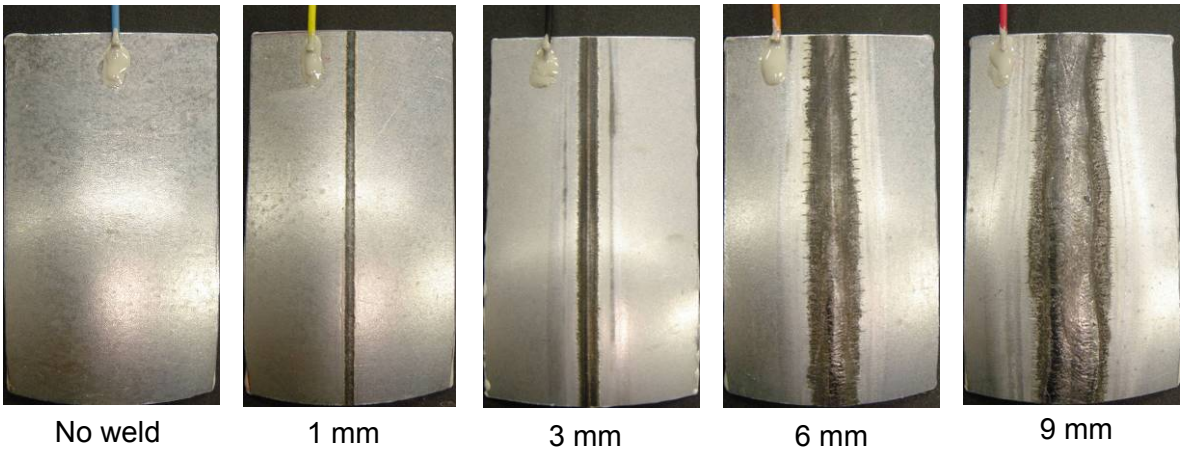

Figure 3-7: Prepared coupons after laser welding and stretch forming

To obtain the same dimensions for LPR testing as the welded coupons, the stretch formed sheets were cut in half and sectioned according to Figure 3-6. They are referred to as "deformed coupons". It is important to point out that after stretch forming, the fusion and the heat affected zones were enlarged further. It should be noted that a peak strain along the weld in the sectioned coupon exists. Two peak strains are also likely to be present across the weld near the long edges of the sectioned coupon. Fully prepared coupons with wire connections and epoxy coated edges are illustrated in Figure 3-7.

3.7 Cyclic Corrosion Test – SAE J2334

The purpose of this test was to evaluate the long term corrosion performance of IF and HSLA steel through the accelerated corrosion process at specified intervals. Both types of steels in the welded and deformed condition were studied. The acceleration of the corrosion process was controlled using an Ascott CC450XP corrosion or environmental chamber as shown in Figure 3-8a. Figure 3-8b shows the holding tank where the test solution is stored. The SAE J2334 standard consists of three stages in a test cycle namely, the humid stage, the salt application or immersion stage, and the dry stage. A schematic flow of the three stages in one cycle is illustrated in Figure 3-9. Each full cycle lasts for one day.

a) b)

Figure 3-8: Photo image of a) main corrosion chamber and b) solution tank

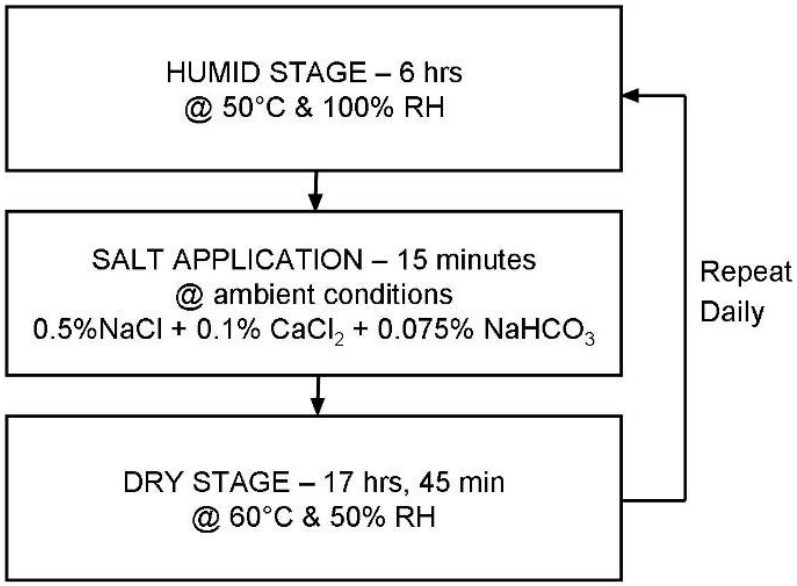

Figure 3-9: Wet, immersion and dry stages in one test cycle of SAE J2334

The test solution consists of 0.5% sodium chloride, NaCl, 0.1% calcium chloride, $CaCl_2$, and 0.075% sodium bicarbonate, $NaHCO_3$. It was noted that sodium bicarbonate forms insoluble precipitates in the presence of calcium chloride, therefore, during preparation of the test solution, the former chemical was dissolved separately in distilled water before adding to the solution of calcium chloride and sodium chloride.

The Ascott operation manual was consulted for programming of the test step and a description is included in Appendix A for reference. During operation, the test solution remains in the holding tank during the humid and dry stages and is pumped into the corrosion chamber during the immersion period. Before the accelerated corrosion test, test coupons were weighed. After 30, 45 and 60 cycles, test coupons were weighed again and examined for surface conditions, zinc corrosion, and rust formation. Test coupons were rotated and randomly placed in the corrosion chamber every 10 cycles to obtain uniform exposure. Figure 3-10 shows that the test coupons were placed at 15° to the vertical on non-metallic racks inside the corrosion chamber.

Figure 3-10: Placement of coupons on racks inside the corrosion chamber

To check the variation of temperature and RH at different locations in the corrosion chamber, six pairs of a thermistor and an RH sensor were wrapped in Tyvek and placed in the corrosion chamber. A Keithley data acquisition system was used to read in the temperature and RH values. To ensure consistent test solution was being used, the solution conductivity and pH were monitored twice a week. The respective coupons were taken out of the corrosion chamber after 30, 45, and 60 days, sectioned and prepared metallographically and examined under the SEM.

3.8 Analysis of Corrosion Products and Corroded Coating

A Rigaku – ACF8, micro X-Ray diffraction machine (XRD) with 2.2 kW of power was operated at 50 kV and 40 mA with a collimator of 800 μm was used to characterize Fe-Zn intermetallic phases after welding and the formation of zinc and iron corrosion products after cyclic corrosion testing. Copper Kα radiation with a wavelength of 0.154 nm was generated. Powder diffraction was particularly useful for the large volume of rust generated after the cyclic corrosion test. Rust was taken from the exposed weld region, dried and ground to fine powder. Since corrosion products on the zinc surface were difficult to remove, they were analyzed on a small section of the test coupons.

A Renishaw RM1000 microscope equipped with a Helium/Neon laser of 630 nm wavelength and an output power of 40 mW in the visible range was also employed to analyze corrosion product on cyclic corrosion tested coupons. During analysis, only 25% of the power, 10 mW, was used and a spot size of 5 μm was focused on the coupon surface. Higher power may over heat the crystal in focus. A frequency range between 70 cm^{-1} to 1800 cm^{-1} (wavenumber) was used with an accumulation of three scans for each spot in order to generate consistent and distinguishable peaks. 20 seconds detection time and 5 accumulations were used to obtain good signal to noise ratio.

To determine the average thickness of a galvanized coating after cyclic corrosion testing, ASTM B 487 – 85 involving metallography and microscopy was utilized. The cyclic corrosion tested coupons, welded and deformed, were sectioned and mounted in epoxy resin. Grinding with silicon carbide paper from #320, #400, to #800 grid size was followed by polishing using 3 μm and then 1 μm waterfree suspension with ethanol based lubricant. Prepared samples were viewed under a JEOL model JSM-6460, scanning electron microscope. Five images dispersed over the width of the cross

section were taken and an average of five measurements across the image was determined as the thickness of the remaining zinc coating.

CHAPTER 4
ZINC COATING TRANSFORMATION

In this chapter, the transformation of the galvanized zinc coating as a result of both Nd:YAG and diode laser welding as well as subsequent stretching forming is presented.

A scanning electron micrograph on the cross section of IF steel is shown Figure 4-1 where a homogeneous layer of eta phase zinc overlays the steel substrate. This can be seen on the cross section view of both the IF and HSLA steels. In between the coating and the substrate is the thin inhibition layer of Fe_2Al_5 formed as a result of 0.135 wt.% aluminum addition in the zinc bath.

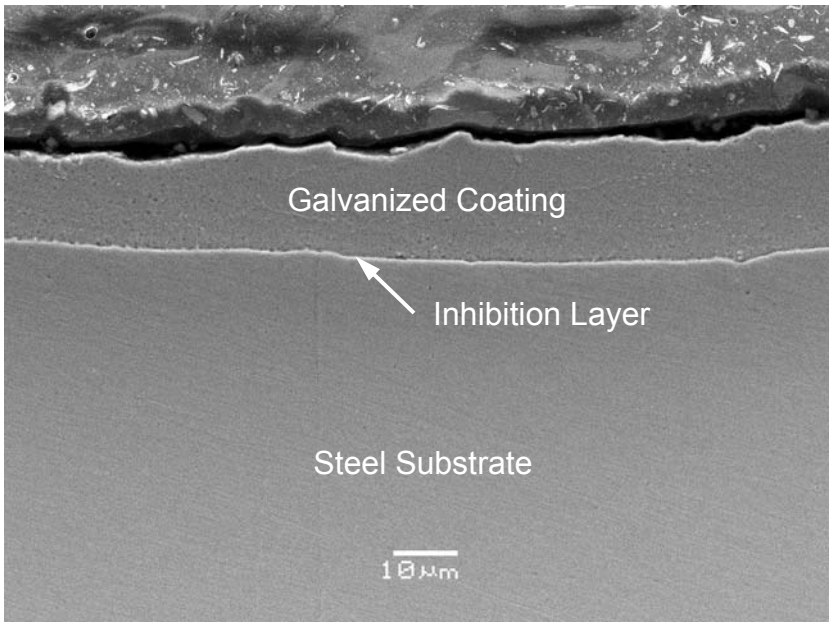

Figure 4-1: Homogeneous eta zinc in the original coating of IF steel

4.1 Nd:YAG Laser Welding

The top view of an Nd:YAG laser welded galvanized sheet is illustrated in Figure 4-2 where the zinc coating had vapourized completely in the fusion zone (FZ). There is a slight change in the shiny appearance of the coating outside of the FZ which indicates the heat affected zone (HAZ).

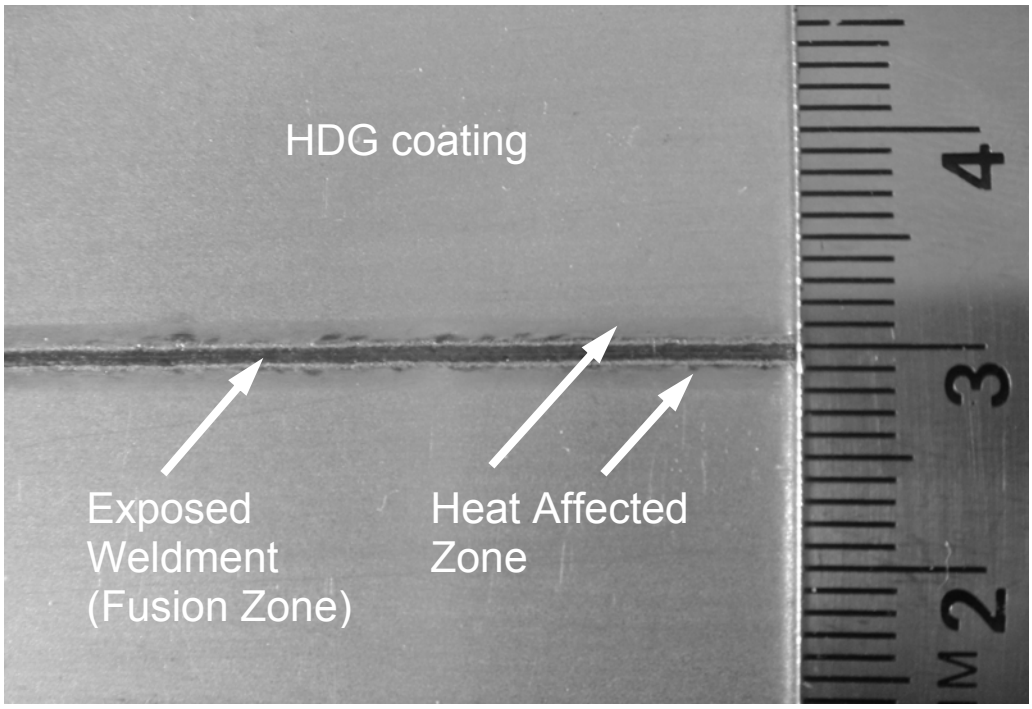

Figure 4-2: Top view of an Nd:YAG laser weldment on galvanized steel

Figure 4-3 shows an example of the cross section of a typical TWB with a 0.77 mm sheet Nd:YAG laser welded to a 1.77 mm sheet. Enlargements on A, B, C, regions in the coating are shown in the succeeding figures. Immediately outside the FZ, a dramatic transformation of the coating over the HAZ can be seen in Figure 4-4. The temperature experienced by the coating was high enough for the zinc to be oxidized. Using EDS, it was revealed that the uppermost region of the coating had a significant content of oxygen and that the new phase with significant growth in the coating was the delta phase zinc.

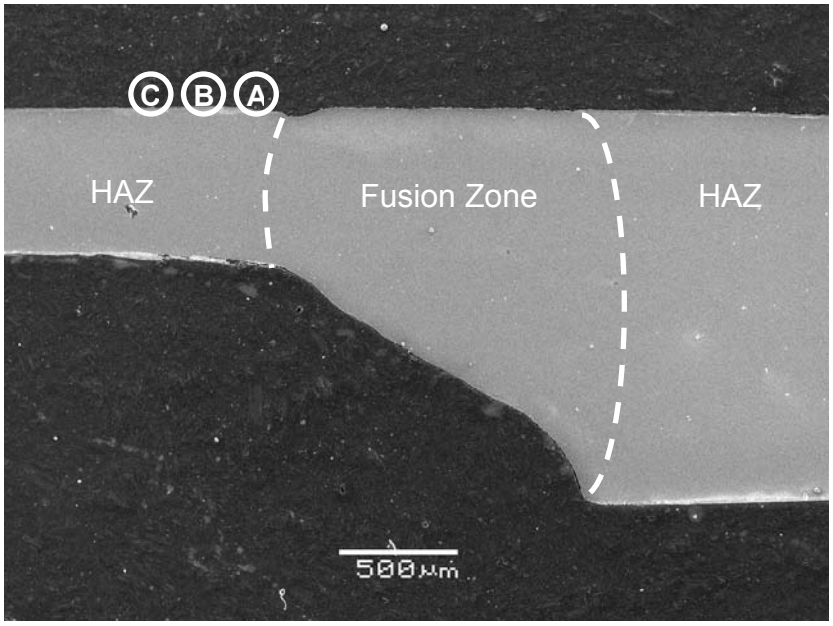

Figure 4-3: Cross section of a typical Nd:YAG laser welded tailored blank joining 0.77 mm to 1.77 mm galvanized steel

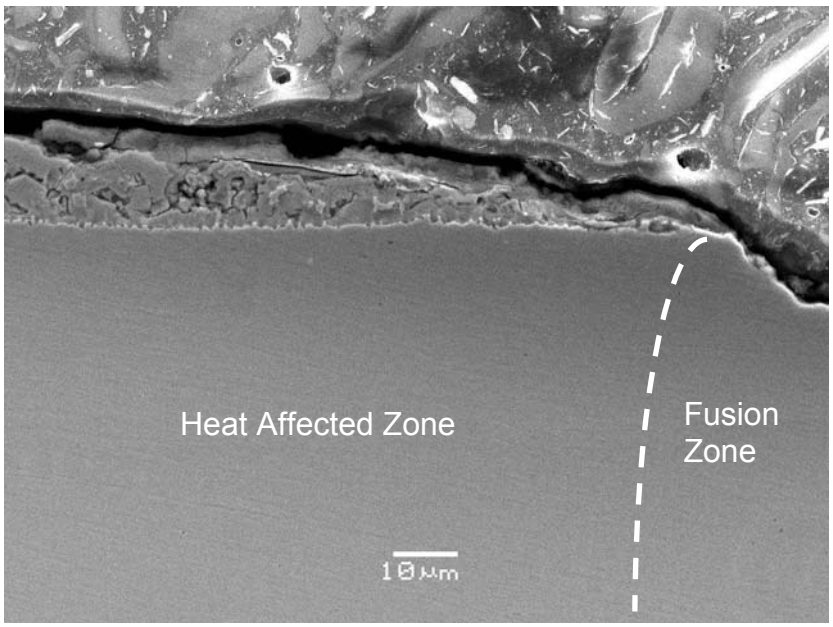

Figure 4-4: Point A in Figure 4-3: Transformed galvanized coating next to exposed weld

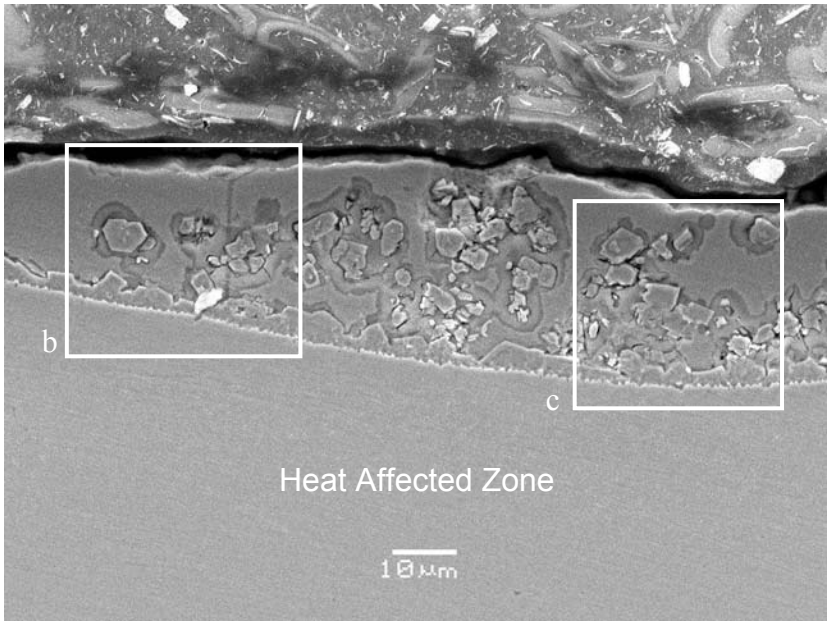

a)

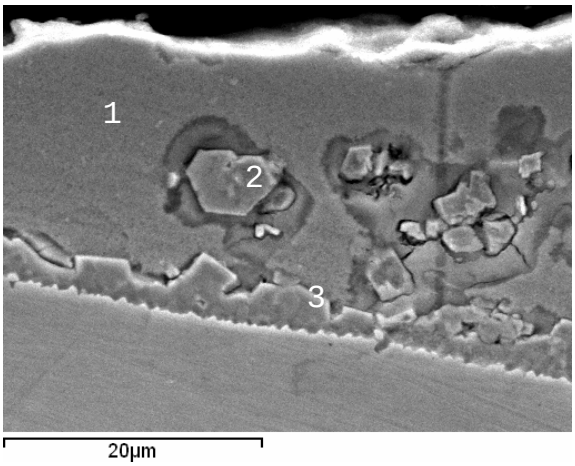

b)

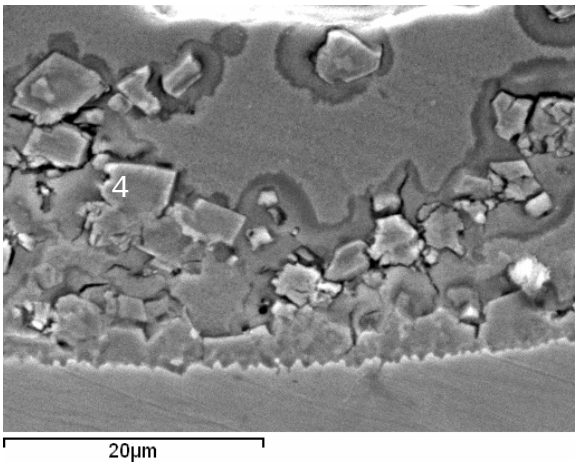

c)

Figure 4-5: a) Point B in Figure 4-3: Fe-Zn alloy formation in the HAZ with growth of delta phase in the enlargements b) and c)

Further away from the FZ, the growth of delta phase was less substantial as indicated in Figure 4-5a. There appears to be delta phase Fe-Zn crystals in the eta zinc matrix in addition to the growth from the inhibition layer. Higher magnifications of the coating are shown in Figure 4-5b and 4-5c where the zeta and delta phases were identified. Their compositions are presented in Table 4-1. Although the gamma phase of higher iron content was not detected, the wavy appearance of the inhibition layer suggests Fe-Zn diffusion and growth of a distinct intermetallic phase. Since the gamma layer can be less than 1 μm in thickness, higher magnifications are necessary to properly identify it.

Table 4-1: Identification of the different Fe-Zn phases from Figure 4-4 and 4-5

Pt.	Zinc wt%	Iron wt%	Phase
1	100	-	Eta
2	88.5	11.5	Delta
3	89.7	10.3	Delta
4	91.9	8.12	Zeta

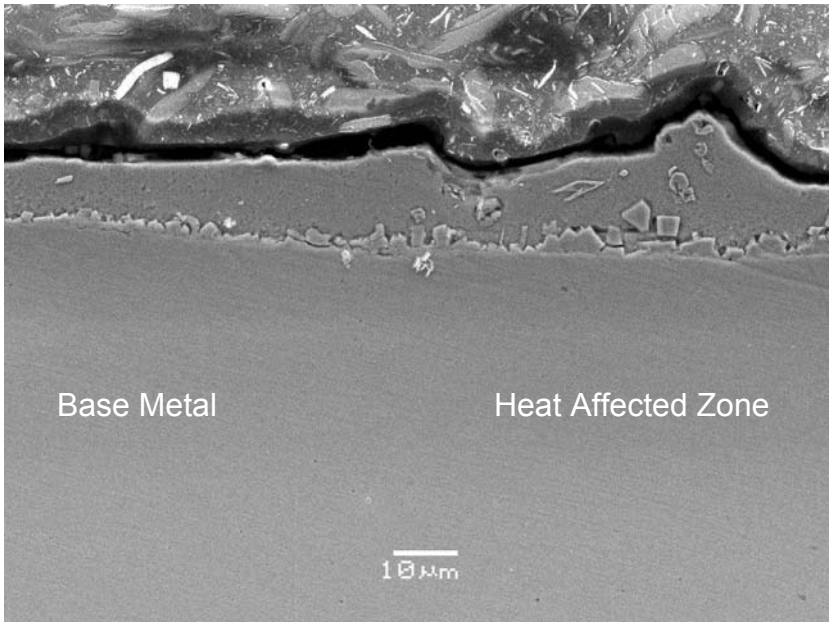

Figure 4-6: Point C in Figure 4-3: Partially transformed coating near the base metal

Further away from the HAZ and closer to the base metal, Fe-Zn diffusion is even less substantial but a minor growth of the delta layer is still apparent as illustrated in Figure 4-6. With a welding speed of 4.8 m/min on a 0.77 mm sheet, the distance over which the galvanized coating had transformed on either side of the FZ was close to 1 mm. Adding the width of the transformation to the exposed width of 1 mm, the coating was affect with a total distance of 3 mm.

In the following section, it will be shown how diode laser welded specimens differ from that of the Nd:YAG laser, and how much the total affected width of the galvanized coating increases.

4.2 Diode Laser Welding

In contrast to Figure 4-2, the top view of a diode laser welded galvanized sheet can be seen in Figure 4-7 where a significant width of the coating was affected. Not only had the zinc coating vapourized in the FZ, it had also vapourized partially in the HAZ, further exposing the steel substrate. Adjacent to the exposed region, a physical build-up of zinc oxide can be observed. Furthermore, it is visually apparent that the original shiny coating changed to different shades of grey in the HAZ as a result of the weld thermal cycle. The effect of a temperature gradient away from the weld allowed different degrees of diffusion in the coating. Consequently, eta phase zinc was transformed to Fe-Zn intermetallic phases. By welding as slow as 0.3 m/min on a 1.77 mm galvanized IF sheet, a transformation over a distance of more than 6 mm on either side of the exposed region was observed. Thus, it is clear that the HAZ generated and width of the coating affected by welding with the diode laser can be considerably greater than that welded with the Nd:YAG laser.

Unlike keyhole welding by the Nd:YAG, conduction welding by the diode laser caused a turbulent weld pool that pushed the molten zinc away and therefore, a build up of zinc was observed outside the FZ as shown in Figures 4-8a and 4-8b. Similar to Figure 4-3, both micrographs depict a substantial amount of delta layer growth. More importantly, the thickness of the coating shows that the build up can be more than 5 times that of the original.

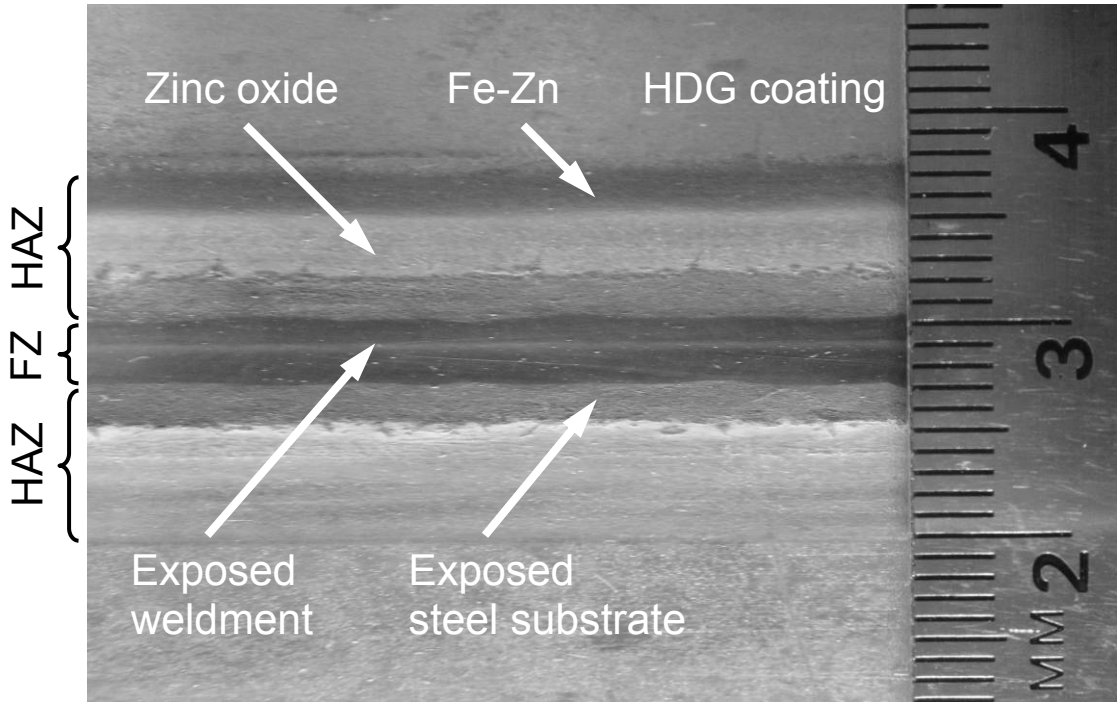

Figure 4-7: Top view of a diode laser weldment on galvanized steel

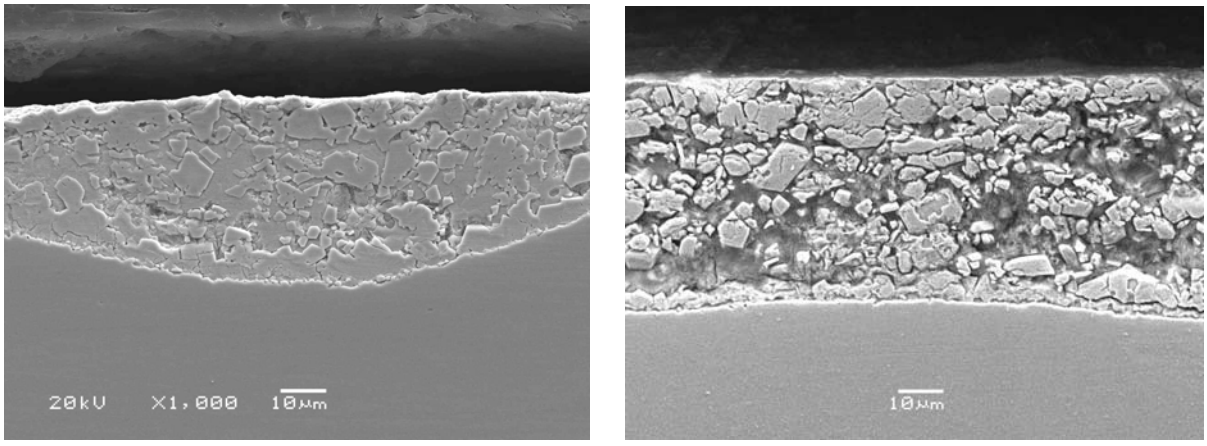

a) b)

Figure 4-8: a) and b) Region of zinc build up on samples welded with a diode laser

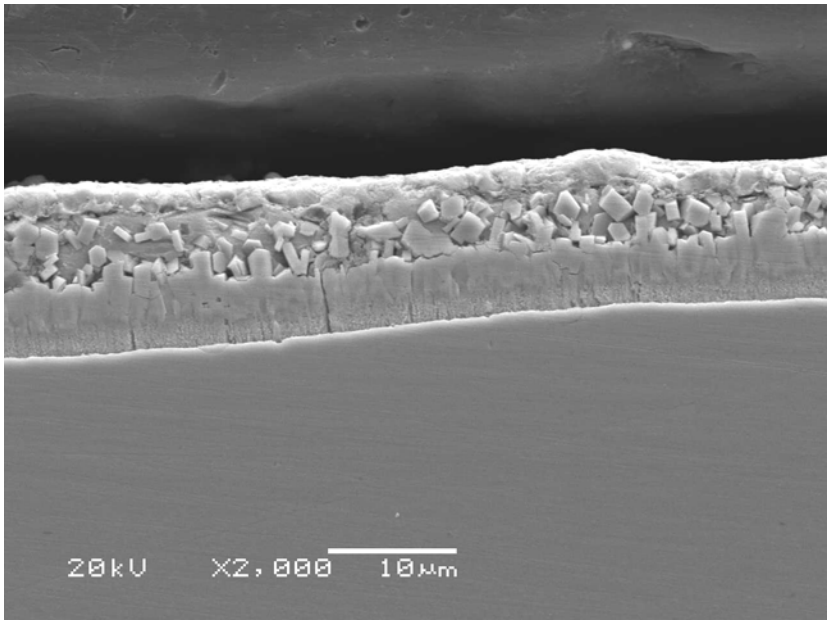

Figure 4-9: Columnar growth of delta phase in HAZ of typical diode laser weld

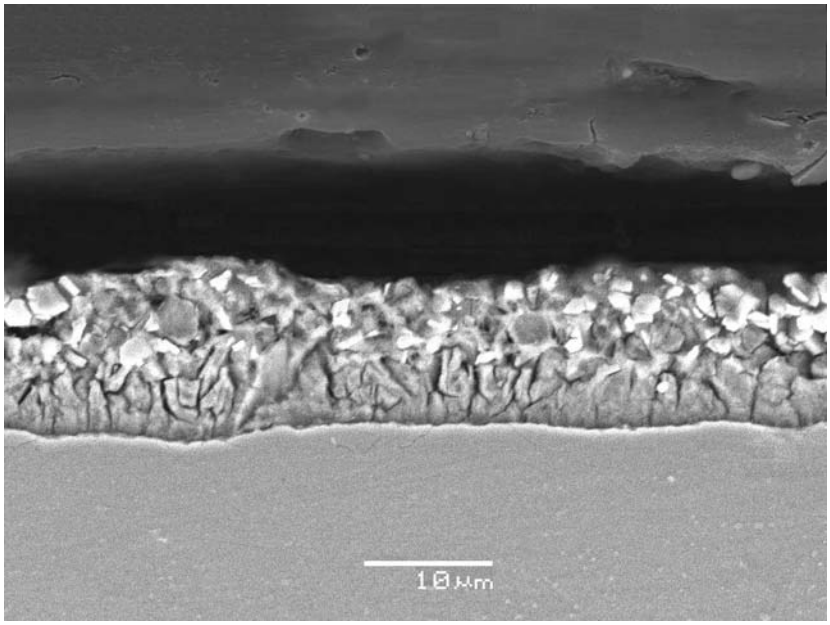

Figure 4-10: Cracks in the delta phase columns after diode laser welding

In addition to forming a puddle shaped build up, conduction welding also resulted in slower cooling rates or longer diffusion times in the HAZ. Consequently, the delta phase was allowed more time to grow in a columnar fashion perpendicular to the steel substrate as shown in Figure 4-9. This contrasts the fast transition shown previously on Nd:YAG laser welded specimen. Another feature in the transformation of the galvanized coating on a diode laser welded sample is the development of cracks perpendicular to the substrate in the delta columns. This was not seen on Nd:YAG laser welded specimens but can be seen in Figure 4-10 and is typical of a galvannealed coating which often causes fluctuations in the coating thickness (Marder 2000). More importantly, cracks in the coating expose the steel substrate to the environment, allow direct attack of chloride ions and may lead to higher corrosion rates.

4.3 Stretch Forming

Even though the use of lubrication and a thin sheet of polypropylene effectively reduced friction and punch effects at the bottom surface of coupon, cracks were produced as a result of the applied load from the punch and biaxial strain. One example is shown in Figure 4-11 where a large crack propagated through the galvanized coating to the underlying steel. Consequently, chloride ions can get trapped inside the crack and induce steel corrosion. It may be possible for micro cracks to be created at the coating substrate interface, or the inhibition layer during the forming process due to the difference in the coating and substrate's hardness or defects in the metallurgical bond.

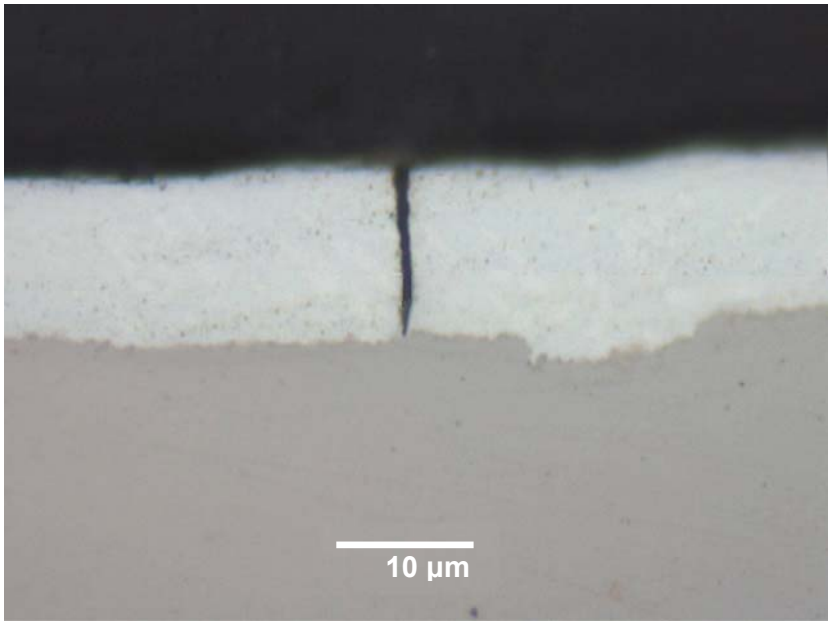

Figure 4-11: Formation and propagation of crack through the galvanized coating to the steel substrate as a result of stretch forming

CHAPTER 5
CONTINUOUS IMMERSION CORROSION TEST

The corrosion potential and the corrosion current density of the test coupons immersed in 0.1 M NaCl solution were monitored over time and presented in this chapter. As a review for the reader, the terms used to describe the test coupons are stripped, where the zinc coating was chemically stripped to leave varying exposed widths of the underlying steel; welded, where laser welding achieved the corresponding exposed widths; and deformed, where laser welded specimens were subsequently stretch formed to generate biaxial strain. In addition to the terms, all test coupons will be referred to by the total widths of the exposed steel.

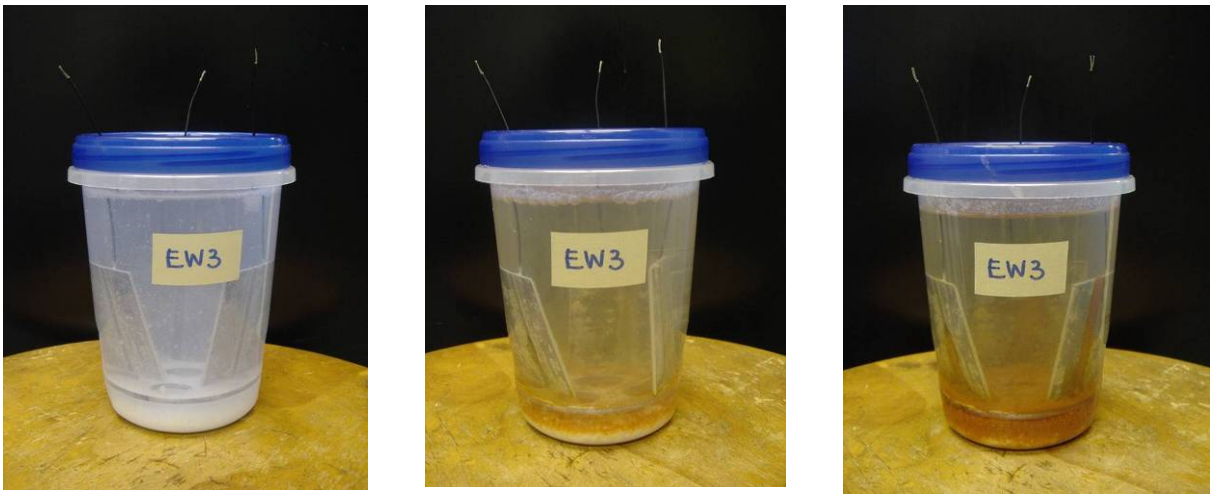

a) b) c)

Figure 5-1: Corrosion cell of stripped coupons having a 3 mm exposed width at a) 7, b) 20, and c) 45 days in 0.1 M NaCl solution

From the continuous immersion test, it was observed that corrosion products initially formed on the test coupon's surface and then accumulated in the corrosion cell. The dissolution of the

galvanized zinc coating in the solution produced white corrosion products. After one week, zinc corrosion products settled and accumulated at the bottom of the corrosion cell as shown in Figure 5-1a. In addition, hydrogen bubbles were seen on the coupon's surface as a result of water decomposition from the cathodic reaction. Once sufficient zinc coating has corroded and could no longer protect the exposed steel, Figure 5-1b shows that iron corrosion products began to form and collect. Gradually, a greater amount of rust accumulated at the bottom and the corrosion cell appears to be red as Figure 5-1c shows. Similar behaviour was observed in the corrosion cells of the welded and the deformed coupons.

5.1 Corrosion current density trends

The average current density vs. time chart for stripped coupons is displayed in Figure 5-2. It can be seen that during the first few days of immersion the current density increased noticeably with increased exposed width but the rate of increase, or the slope for all coupons were nearly the same. At the peak, the current density ranged from 0.23 A/m^2 for the 0 mm coupon to 0.32 A/m^2 for the 9 mm coupon.

Similarly, Figure 5-3 shows the current density vs. time trend for the nominal, narrow and wide coupon having a 3 mm exposed width. Among the three, the 3 mm(W) coupon having twice the nominal width and zinc surface area experienced the lowest current density of 0.19 A/m^2 while the 3 mm(N) coupon with half the nominal width and zinc surface area experienced the highest current density of 0.37 A/m^2. After the peak value, the current density decreased sharply for all stripped coupons and stabilized at a lower value than the initial. A similar current density trend was observed by El-Mahdy et al. (2000) when their zinc coated steels were exposed to increasing number of wet-dry cycles.

The zinc peak corrosion rate as a function of exposed width can be seen in Figure 5-4 with an increasing trend. The equivalent corrosion rates for the 3 mm(N) and 3 mm(W) coupons are 0.29 and 0.56 mm/yr respectively. It can be seen that with 4 times as much zinc surface area, the corrosion rate of the 3 mm(N) is nearly twice that of the 3 mm(W) coupon.

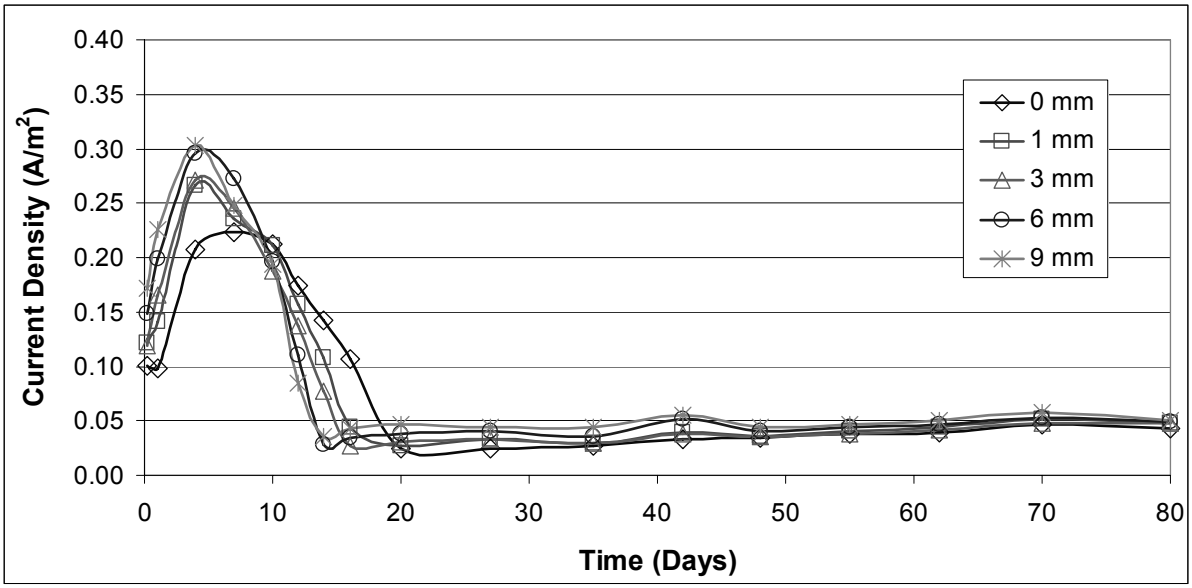

Figure 5-2: Average corrosion current density vs. time for stripped coupons

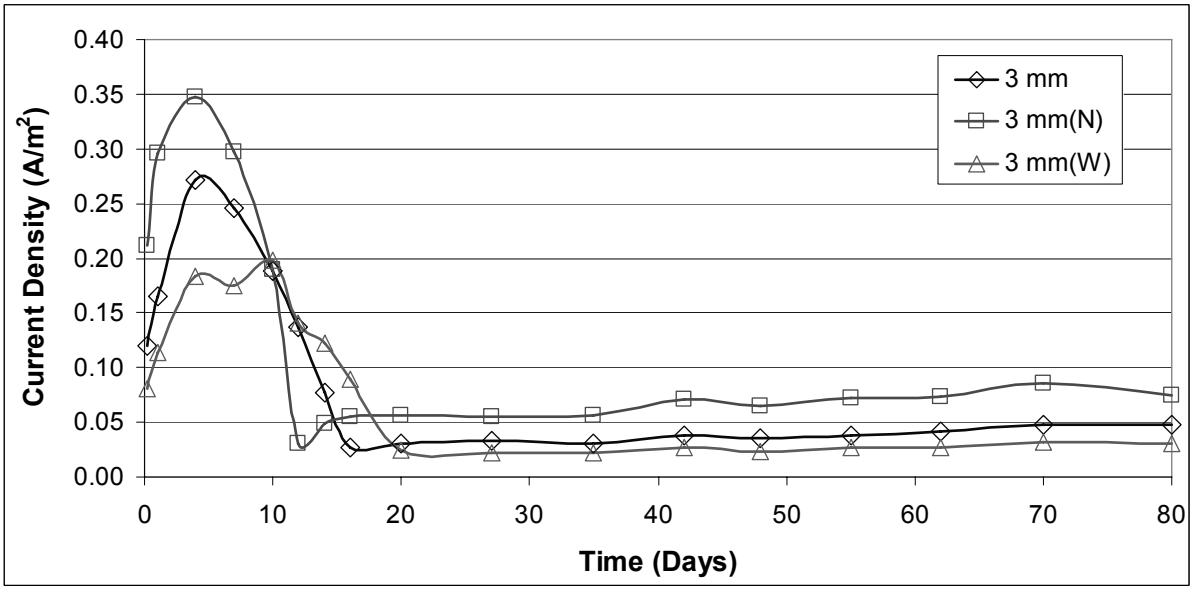

Figure 5-3: Average corrosion current density vs. time on a nominal, narrow, and wide coupon having a 3 mm exposed width

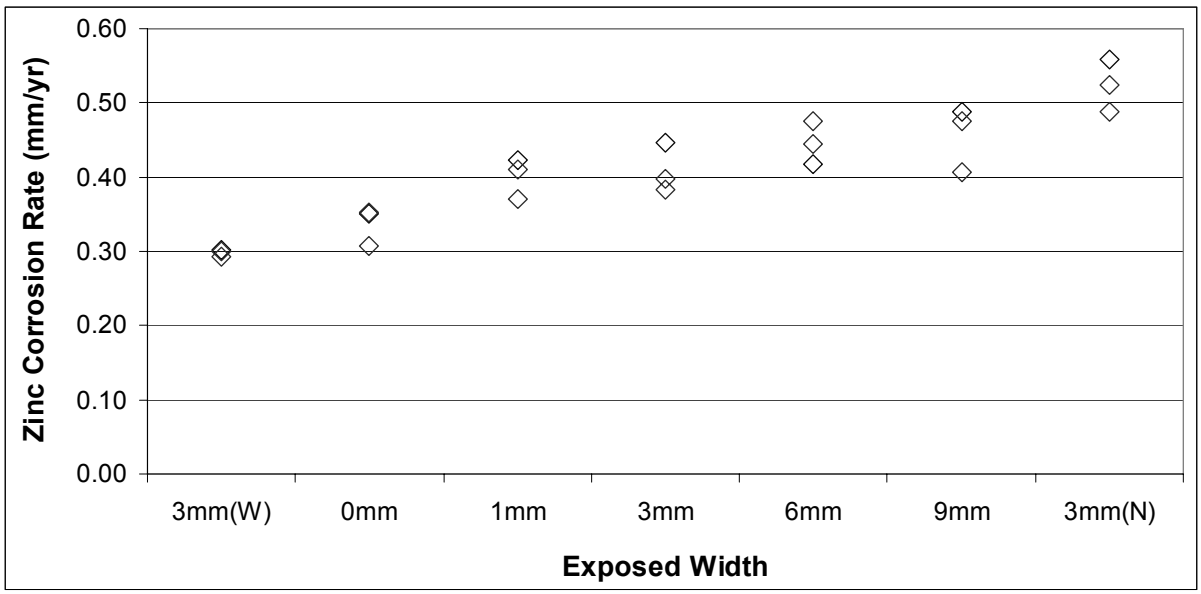

Figure 5-4: Zinc peak corrosion rates for stripped coupons

With the application of laser welding on the same batch of galvanized sheets, few differences were evident in the current density trend of the welded coupons when compared to stripped ones. This is illustrated in Figure 5-5. The first noticeable difference was a more blunt peak during the initial period of immersion; for welded coupons the rise and fall of the current density around the maximum value was more gradual than that of the stripped coupons. The only exception was the 3 mm coupon which behaved in a similar manner as the stripped one and accounts for a possible source of error. Secondly, the peak current densities for the welded coupons were all lower than those of the stripped ones. Thirdly, the zinc coating was able to endure over a longer period before commencement of rust on the welded coupons than on stripped ones. What was similar between welded and stripped coupons was the eventual stabilization of the current density at approximately 0.05 A/m^2.

Figure 5-6 shows a comparison of the zinc peak corrosion rates between the welded and stripped coupons. It was unexpected that on average the welded 1 mm coupons performed equally well as the non-welded ones. Of the welded specimens, the 3 mm coupons showed the highest corrosion rate of 0.46 mm/yr. On average, both 6 and 9 mm coupons showed lower corrosion rates than those of narrower exposed widths and non-welded ones.

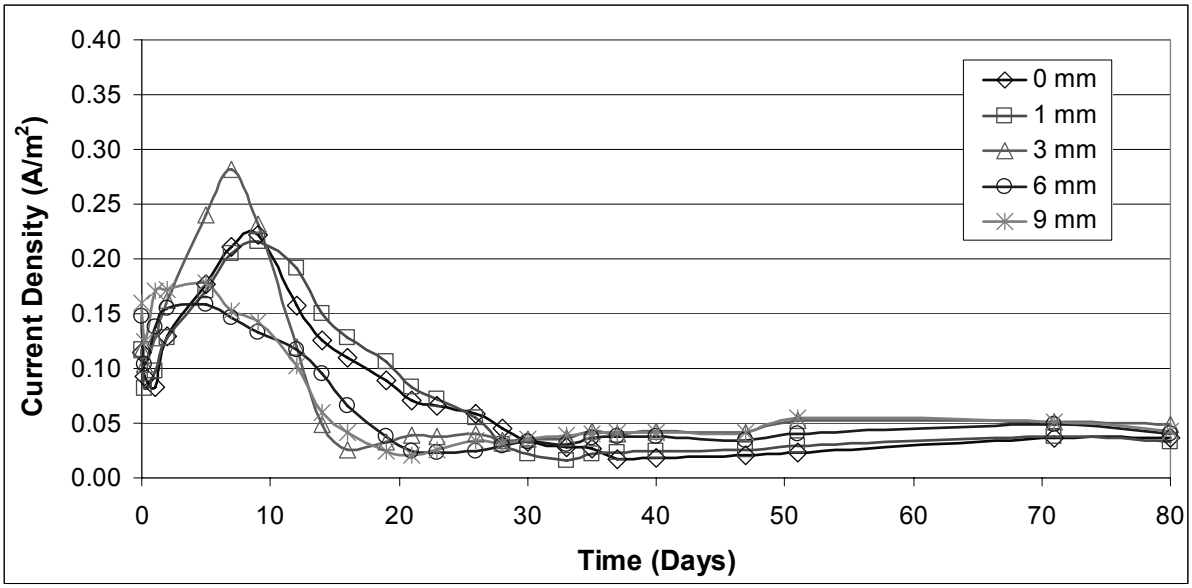

Figure 5-5: Average corrosion current density vs. time for welded coupons

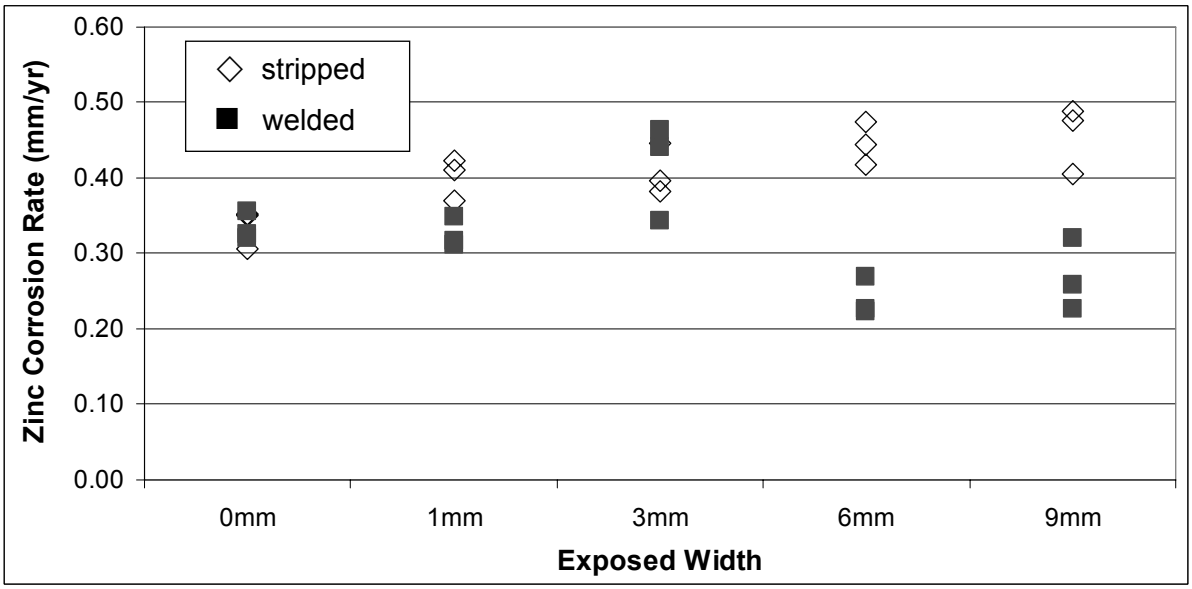

Figure 5-6: Comparison of zinc peak corrosion rates for welded and stripped coupons

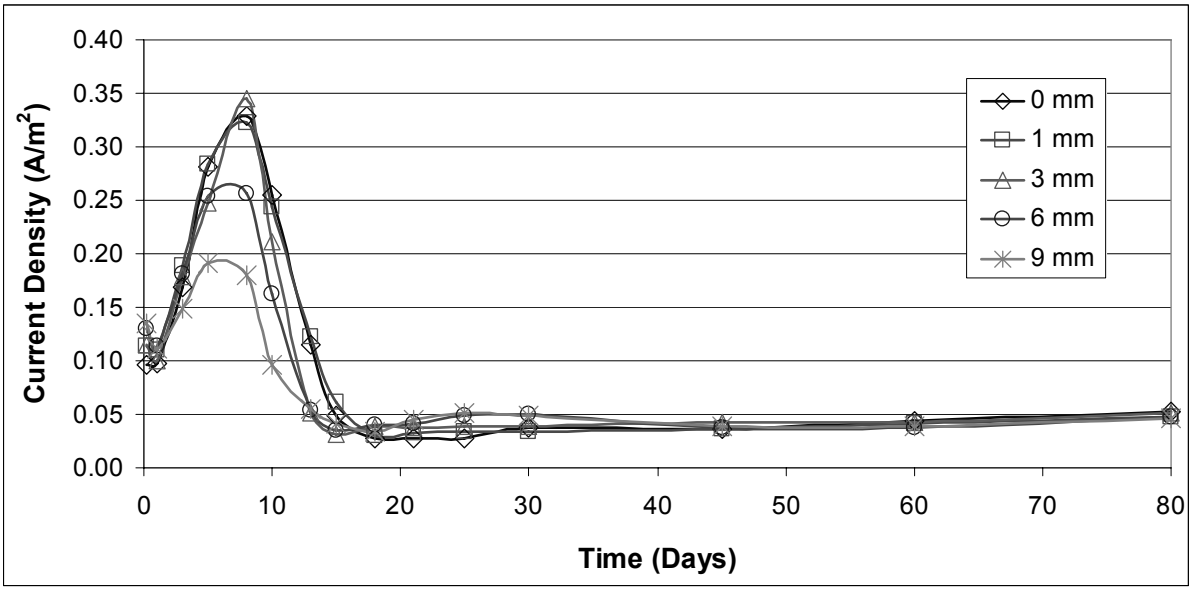

Figure 5-7: Average corrosion current density vs. time for deformed coupons

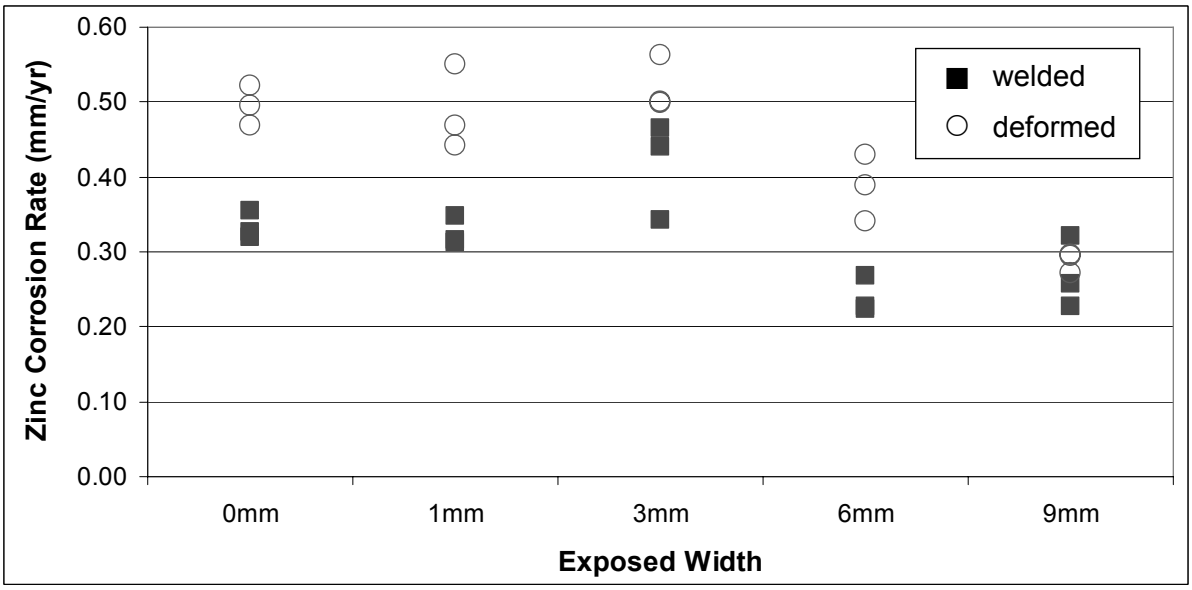

Figure 5-8: Comparison of zinc peak corrosion rates for welded and deformed coupons

After stretch forming, Figure 5-7 shows that all deformed coupons demonstrated higher corrosion current densities compared to laser welded ones except for the 9 mm coupon. It was interesting to observe that all deformed coupons reached the peak current density after nearly the same exposure in solution. Not only were the increases in current density sharper than that of the welded coupons, they were similar to that of the stripped ones. Also common to both stripped and welded coupons was that the long term steady current density settled at around $0.05 A/m^2$. Upon examining the corrosion rates in Figure 5-8, it can be seen that the deformed 3 mm coupon revealed the highest corrosion rate with an average of 0.52 mm/yr. In addition, deformed 0, 1 and 3 mm coupons demonstrated very close values but a decreasing trend was noticed with the 6 and 9 mm coupons. All deformed coupons except for the 9 mm exhibited greater corrosion rates than welded ones.

5.2 Corrosion Potential trends

The corrosion potential of hot-dip galvanized steel immersed in 0.1M NaCl was about -1.05 V_{SCE}. Contrary to the development of the corrosion current density, the corrosion potential first decreased in the negative direction as seen in Figure 5-9. After a few hours the zinc coating reached an equilibrium potential in the NaCl solution. After 1 day, the corrosion potential began to increase slowly in the positive direction. When the corrosion potential reached past -0.95 V_{SCE}, a sudden jump occurred for stripped coupons, increasing to a value close to that of the steel substrate in 0.1M NaCl solution which is around -0.55 V_{SCE}. In El-Mahdy's study (2000), the rapid increase in the corrosion potential occurred near -0.85 V_{SCE}. Over time the corrosion potential stabilized at an intermediate value closer to that of iron than zinc. Figure 5-9 also illustrates the relationship between exposed width and potential; the wider the exposed width, the less time it took for the potential to rise rapidly. Shorter transitions were observed for the 6 and 9 mm coupons while longer transitions were seen on the 0 and 1 mm coupons. On the 9 mm coupon, this abrupt change occurred after 10 days and settled down in 2 days whereas on the 1 mm coupon the rise occurred after 16 days and stabilized after 7 days. During the rapid rise in potential, rust formation could be seen with tints of orange-red in the exposed region or at random locations on the zinc surface.

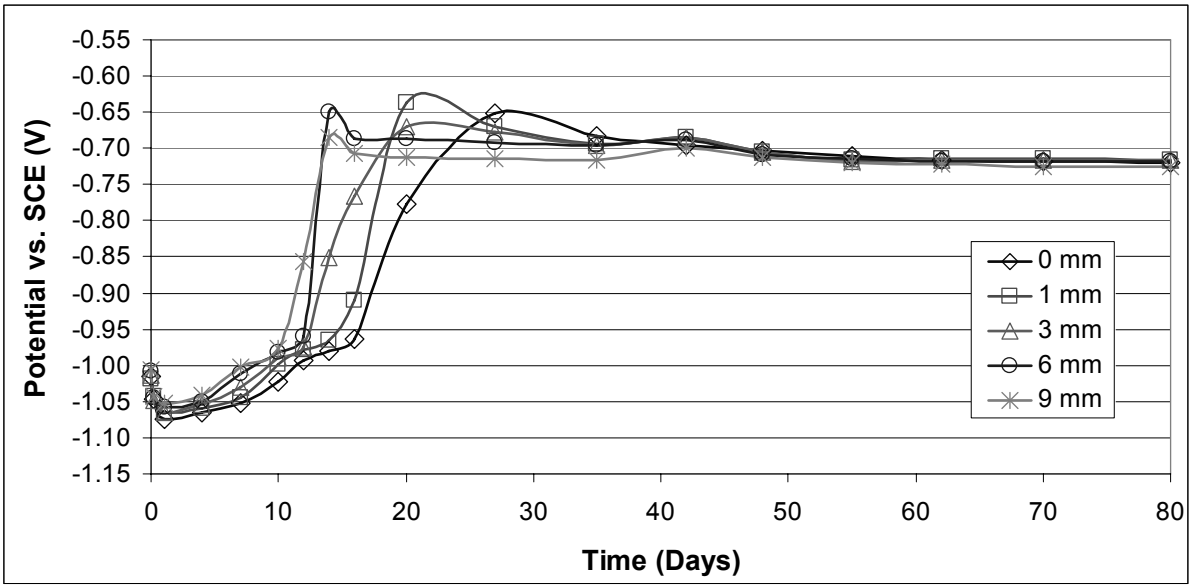

Figure 5-9: Average corrosion potential vs. time for stripped coupons in 0.1 M NaCl

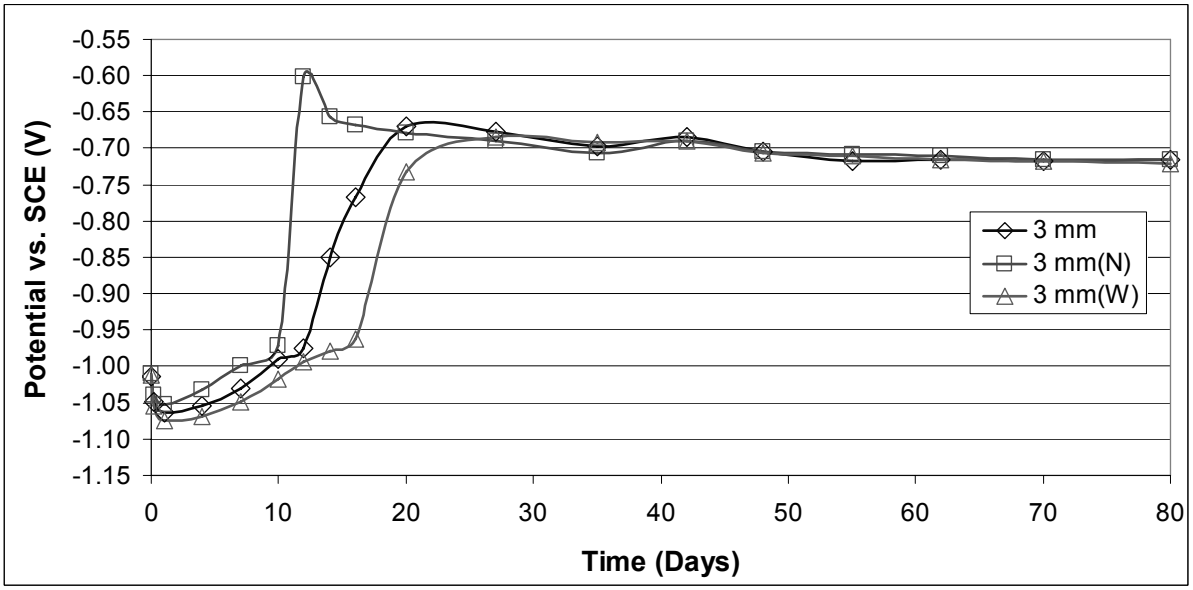

Figure 5-10: Average corrosion potential vs. time on a nominal, narrow, and wide coupon having a 3 mm exposed width in 0.1 M NaCl

Figure 5-10 shows that with half the zinc surface area as the nominal, the potential rises of the 3 mm(N) coupons were nearly vertical and the transition time to the stabilizing mixed potential was very short. With four times as much zinc surface area as the 3 mm(N) coupons, the 3 mm(W) ones endured 60% longer time to the rapid potential rise. The potential of the 3 mm(W) coupons also approached the mixed value steadily without increasing above it as the 3 mm coupons did.

When comparing Figure 5-2 and Figure 5-9, it can be seen that when the current density reached a maximum, the potential began to rise. Once current density reached a minimum, the potential was close to the most positive value. Finally when the corrosion potential stabilized, an intermediate value or a mixed potential of about -0.70 V_{SCE} was observed. The total time of this process varied distinctly with different exposed widths. While on average the zinc protection lasted over 16 days on coupons without an exposed region, it lasted only 12 days on coupons having a 9 mm width of exposed steel. At the mixed potential, rust build up was observed for all stripped coupons. El-Mahdy et al. (2000) also reported a similar corrosion potential trend as a function of wet-dry cycles.

Consider now the corrosion potential for welded coupons as displayed in Figure 5-11. It is apparent that a distinct threshold potential did not exist. The rise in potential was considerably gradual for the 3, 6 and 9 mm coupons. While on average, the potential rise for stripped coupons occurred in less than two days, the transition progressed over 10 days for the 3, 6 and 9 mm coupons before losing zinc protection and allowing rust to form. The overall protection afforded by the zinc coating on the exposed steel lasted well over 20 days for the 3, 6, and 9 mm coupons. This protection is even longer for the 1 mm and non-welded coupons in which case rust formation on the exposed steel was not observed after close to 30 days. In comparison to stripped coupons, the total time to losing the zinc protection before stabilizing at the mixed potential was substantially longer in welded ones. It was anticipated that rust formation would occur first on the 9 mm coupons then on the 6 and 3 mm coupons; however, results indicated the opposite trend. One explanation for this behaviour could be the effect of the locally annealed coating in the HAZ on welded coupons. Thus, with a wider annealed region in the coating and HAZ width, the 9 mm coupons showed greater resistance and a longer time to rust formation than the 6 mm ones. Another reason for the short zinc protection on the 3 mm coupons could be that while all other welded coupons were 1.77 mm thick sheets, the 3 mm coupons were 0.77 mm thick sheets, whose coating weight was just less than that of the 1.77 mm.

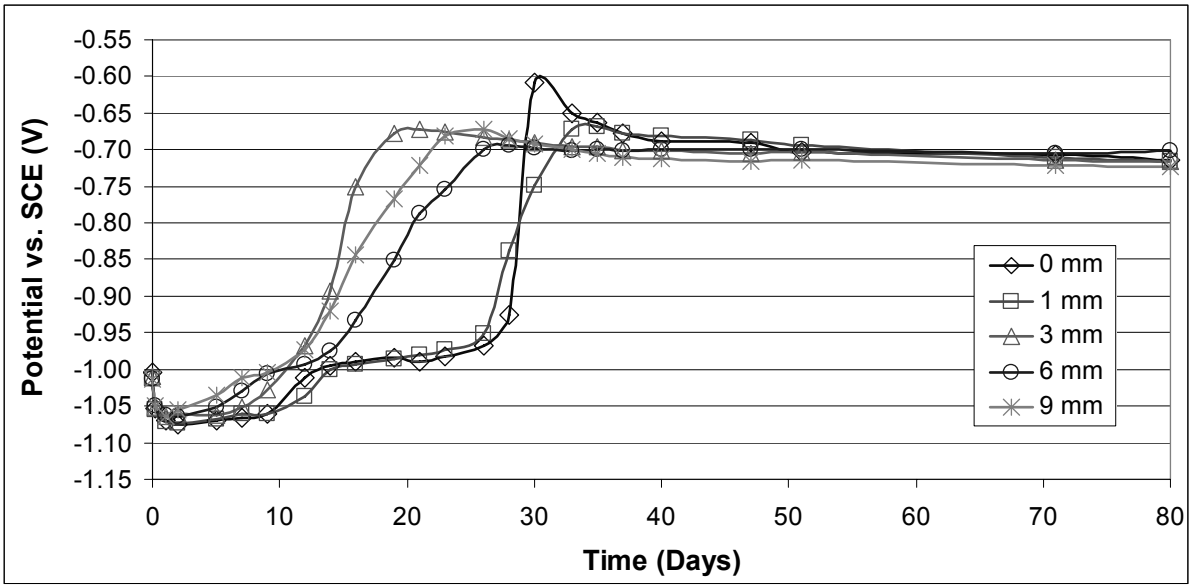

Figure 5-11: Average corrosion potential vs. time for welded coupons in 0.1 M NaCl

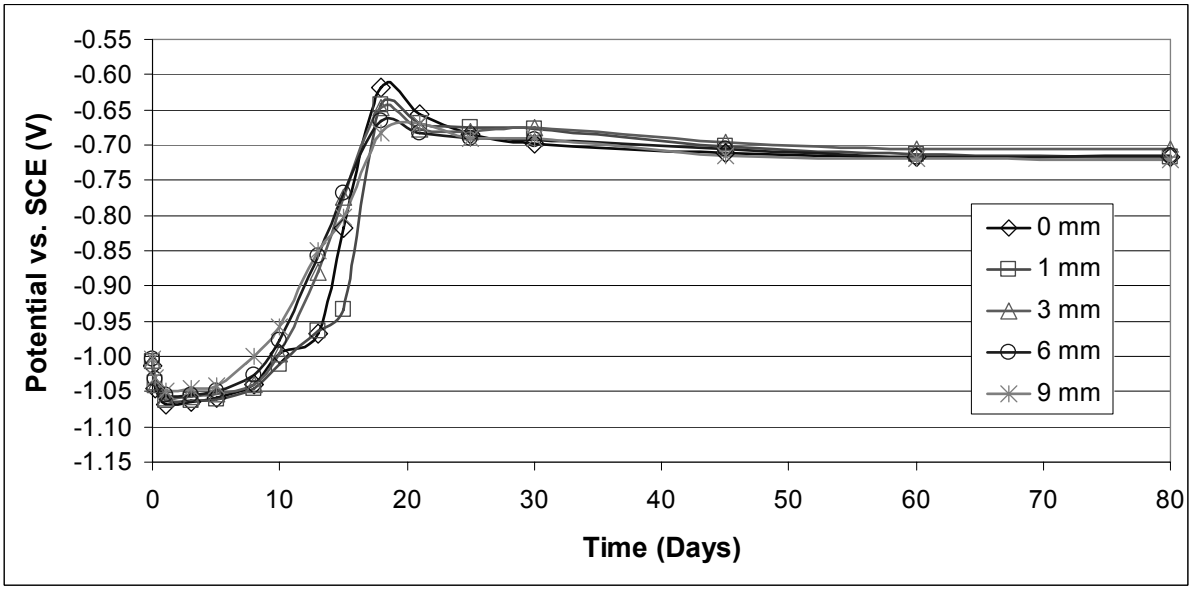

Figure 5-12: Average corrosion potential vs. time for deformed coupons in 0.1 M NaCl

For deformed coupons, the corrosion potential versus time is shown in Figure 5-12. In this batch of coupons, the average slope of the potential rise was greater than that of welded coupons yet still more gradual than that of stripped ones. But interestingly, unlike the varying amount of transition times seen in welded and stripped coupons, the potential rise for all deformed coupons occurred very close to each other. Compared to the previous figures, the zinc protection afforded to the 0 and 1 mm coupons after stretch forming were significantly diminished. The similar slope of potential rise may be related to the amount of biaxial strain experienced by the coupons. Therefore, even with different widths of the exposed region, the potential versus time trend was brought close together with the same amount of biaxial strain. Similar to the previous two batches, the long term mixed potential for deformed coupons remained at about -0.70 V_{SCE}.

A summary and comparison of the average time to rust for all three types of coupons is presented in Table 5-1. It is evident that with wider exposed widths, welded coupons were the most corrosion resistant followed by deformed coupons. Stripped coupons corroded the fastest with little corrosion resistance. While the 3 mm coupons performed consistently among all three types, the 0 and 1 mm coupons varied considerably.

Table 5-1: Comparison of average time to rust in days for stripped, welded and deformed coupons

Coupons	3 mm(W)	0 mm	1 mm	3 mm	6 mm	9 mm	3 mm(N)
Stripped	20	20	18	16	13	13	11
Welded	-	30	30	16	21	19	-
Deformed	-	16	16	15	15	15	-

5.3 Corrosion Progress

From the figures of current density and corrosion potential versus time trends, four stages can be distinguished. During the initial stage, the corrosion potential of the galvanized zinc coating reached equilibrium in the bulk solution. The exposed steel substrate in the salt solution was protected by the galvanic throwing power of zinc. Zhang's studies (2000) have shown that the protection distance of zinc when coupled to steel is much greater in bulk solution than in a thin layer of electrolyte and in dry conditions. This is due to the low resistivity of the electrolyte and the high mobility of zinc ions in bulk solution.

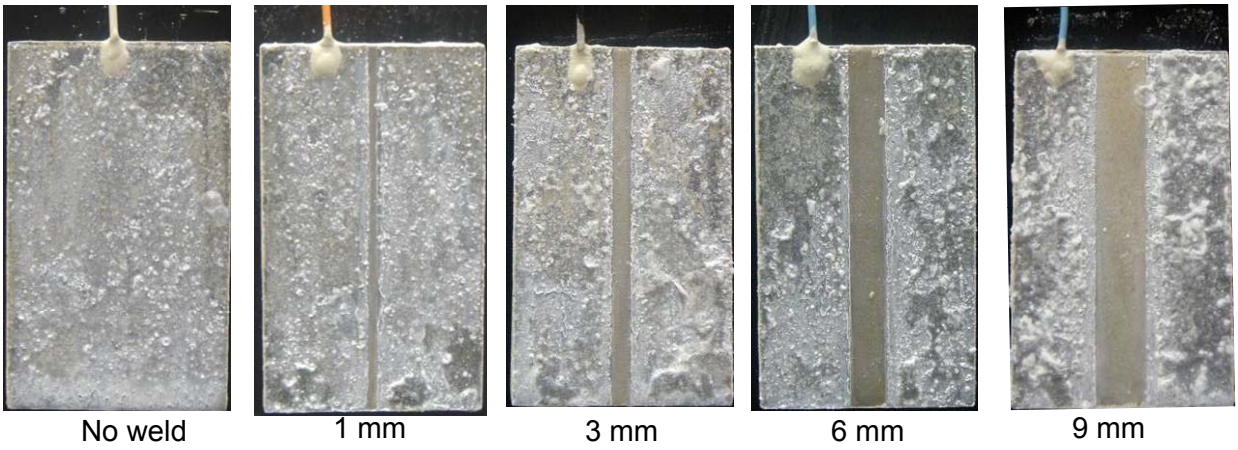

Figure 5-13: Zinc corrosion on stripped coupons after 10 days of immersion in 0.1 M NaCl

In the second stage, zinc dissolved rapidly in solution in order to protect the exposed steel from corroding. By examining the current density trend of the stripped coupons, the rates of increase or the slopes during the first few days of immersion were very close for all exposed widths. This may be attributed to the weight of the zinc coating on the steel substrate. It is also a property of zinc in NaCl solution. Figure 5-13 shows that the exposed region on stripped coupons was still protected after 10 days. This sacrificial action is commonly known as cathodic protection where the zinc corroded more rapidly in order to shield the underlying steel. It is speculated that if a very wide piece

of zinc was coupled adjacent to a narrow strip of steel, the corrosion potential of the couple would remain close to -1.05V_{SCE} for a very time until a substantial amount of zinc had either dissolved or formed corrosion products. As exposure continued, the corrosion of zinc slowed down with the formation of corrosion products. This can be seen after the peak where current density dropped at almost the same rate as it first increased. It is suspected that as zinc corrosion products accumulated, the surface layer acted as a barrier to the solution, significantly reduced the current density and became passivated. It was suggested by Prosek et al. (2007) that the increasing amount of zinc oxide or ZHC may also prompt a decrease in the zinc current density or corrosion rate.

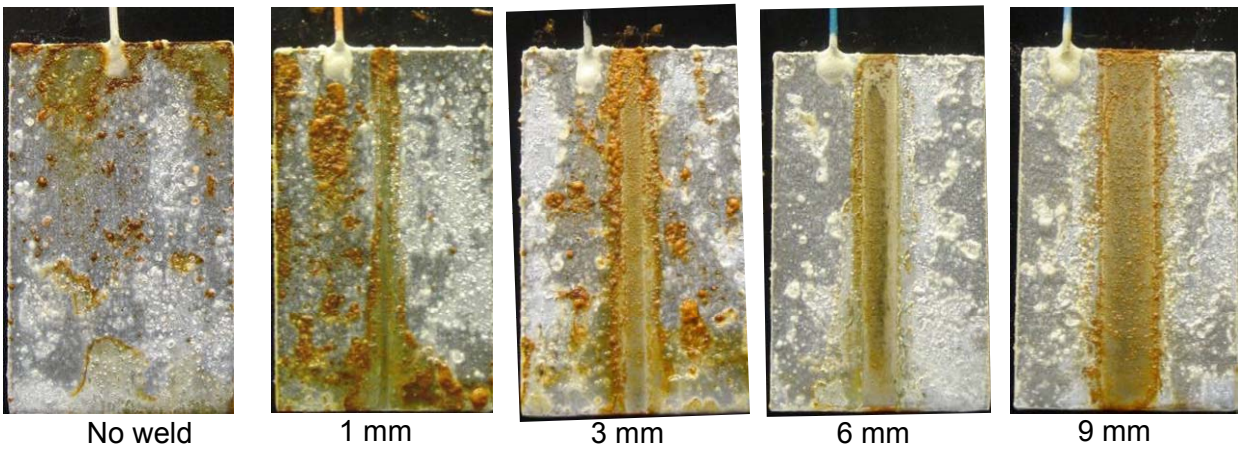

Figure 5-14: Rust formation on stripped coupons after 27 days of immersion in 0.1 M NaCl

The corrosion progress entered the third stage when the potential rose rapidly towards the value of iron and rust started to form in the exposed region. This is illustrated in the stripped coupons at day 27 in Figure 5-14. These three stages have also been observed in El-Mahdy's (2000) and Yadav's (2004) corrosion monitoring of galvanized steel in accelerated conditions as a function of wet-dry cycles. While the transitions were fast and abrupt for stripped coupons, they were longer and more gradual for both welded and deformed coupons as observed from Figures 5-11 and 5-12. With the consumption of zinc in solution and formation of corrosion products, the coupon surface experienced some degree of passivation where the current density decreased steadily until it

stabilized. Although at this point, there was no longer adequate protection from zinc to further suppress the corrosion of the exposed steel, the passivated surface had significantly reduced the corrosion current on the coupon. It is believed that welded coupons were able to persevere over a longer period of time without rust than stripped coupons due to the formation of Fe-Zn alloy compounds in the coating. Since the locally annealed coating in the HAZ had a comparable microstructure to that of a GA coating, therefore, their formation provided improved corrosion resistance than a homogeneous HDG coating.

In the last stage, the current density remained relatively constant while the potential stabilized at a mixed value between that of zinc and iron. Rust accumulation was seen in the exposed region. It was observed that the build up of both zinc and iron corrosion products on the surface could polarize the corrosion potential of the coupon. Over time, rust build-up will likely widen in the exposed region as well as penetrate through the zinc corrosion products on the zinc surface. Figure 5-13 shows a stripped, welded and deformed coupons having a 9 mm exposed width after 45, 40 and 45 days in solution respectively.

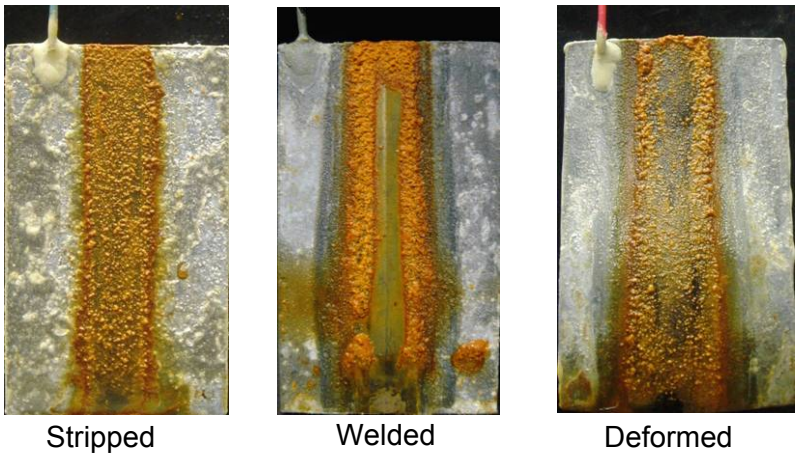

Figure 5-15: Rust formation on a 9 mm exposed width after a) 45 b) 40 and c) 45 days of immersion in 0.1 M NaCl

It was observed on all three types of coupons that there was a slight more build up of rust at the coating-steel interface than in the exposed region itself. For welded coupons, it may be attributed to the development of cracks in the coating after laser welding which traps the chloride ions and facilitates corrosion of the substrate. In the exposed region, rust does not adhere well to steel in solution and can easily spall off to the bottom of the corrosion cell. The visual appearance of the exposed region after welding differs from that after chemical stripping of the stripped coupons. Therefore, it is possible that a very thin oxide film was formed on the exposed surface during diode laser welding of the 3, 6 and 9 mm coupons which provided resistance to rust formation.

5.4 Effect of zinc surface area on corrosion

The 3 mm (N) and (W) stripped coupons were made to investigate whether a difference in zinc surface area can influence the corrosion performance. LPR results indicate that with half the nominal zinc area, the 3 mm(N) coupons corroded much sooner than did the normal 3 mm coupons while the 3 mm(W) coupons corroded at a later time. The abscissa in Figure 5-3 can also be interpreted as increasing in zinc surface area which reveals a linear relationship with corrosion rate. Hence, the larger the zinc surface area, the lower the corrosion rate and the longer the zinc protection. On a tailor welded blank, the actual exposed area of the steel after laser welding is considerably smaller than that of the remaining galvanized coating. Therefore, a large zinc to steel area ratio could suggest very much greater galvanic protection than that observed in the relatively small coupons. Further investigations on the corrosion rate of coupons with increased widths of exposed steel while maintaining a constant zinc surface area would be useful.

5.5 Effect of Fe-Zn intermetallics in the coating over the HAZ

The difference between the trend of corrosion potential of stripped coupons in Figure 5-8 and that of welded coupons in Figure 5-9 can be attributed to the formation of Fe-Zn intermetallics in the HAZ. The effect is especially prominent on the 6 and 9 mm coupons where the HAZ is wide and growth of

the delta phase is substantial. The narrower HAZ experienced by the 3 mm coupons resulted in a faster rise in potential and more importantly, shorter time to rust formation.

Although specific plateaus in potential were not observed corresponding to the individual corrosion potentials of the intermetallic phases, the increase in potential was relatively gradual suggesting the presence of a multi-compound coating affording varying degrees of protection and prolonged life to the exposed substrate. Had welding conditions been controlled to the extent such that a relatively wide HAZ was produced with each Fe-Zn phase growing homogeneously, then perhaps a more noticeable potential plateau would have exist.

Past research and publications on the effect of increasing iron content in the galvanized coating proved the enhanced corrosion resistance of Fe-Zn compounds to that of pure zinc (Hadden 1952; Campbell, Stanners et al. 1965). Thus, by producing Fe-Zn compounds in the coating, it is possible for laser welding to improve the corrosion performance of galvanized steel.

5.6 Effect of deformation in the coating

When laser welded sheets were subjected to LDH testing, the exposed region was expanded and increased in surface area. More importantly, significant cracks at the coating steel interface perpendicular to the weld line could be observed on the surface. This could have lead to the pronounced galvanic corrosion and rust accumulation. Stretch forming not only reduced the thickness of the galvanized coating resulting in shortened protection time, it generated micro cracks in the coating and deteriorated the corrosion performance. Due to the high ductility zinc, the eta phase is more likely to resist crack formation than the brittle zeta or delta phases where cracks can propagate and expose the steel substrate. Especially after deformation, cracks will likely lead to higher corrosion rates.

The corrosion current density of deformed coupons confirmed higher corrosion rates than that of welded coupons. The biaxial strain generated in this work caused an increase of more than 40% in the zinc corrosion rate in the non-welded coupons. In contrast, the corrosion rate of the 9 mm coupon remained relatively constant after deformation. It is probable that an oxide layer exists on the expose

weld and was responsible for the corrosion protection and negligible rust build up. Since the 9 mm coupon also had the widest HAZ, perhaps the degree of strain was inconsequential to the corrosion resistance afforded by Fe-Zn intermetallics.

It was suspected that the presence of peak strains both along and across the weld might affect the corrosion performance. However, no significant differences were detected from electrochemical results nor by visual inspection. Rust accumulation on the deformed coupon surface was generally similar to that on welded coupons where the coating-steel interface showed slightly more volume than in the exposed region. It is possible that the cracks in the coating outside the exposed region trapped the chloride ions and induced more rapid corrosion in between the delta columns which appeared to have a greater accumulation than the exposed region itself. It is also likely that peak strains produce only a localized effect in which case detection of corrosion potential and current density changes on the surface require electrodes and monitoring methods at a smaller scale.

CHAPTER 6
CYCLIC CORROSION TEST

By conducting the cyclic corrosion test according to SAE J2334, corrosion was accelerated relative to general atmospheric corrosion on the welded and deformed coupons of both IF and HSLA steel. Same as in the continuous immersion test, coupons were made in triplicates for each welding speed, hence, exposed width. After an exposure of 30, 45, and 60 cycles, one coupon from each set was removed from the corrosion chamber. The corrosion progress on the coupons' surface was examined and the final weight of corroded coupons was recorded.

Unfortunately, difficulty arose in interpreting the weight measurements. Due to the accumulation of both iron and zinc corrosion products on the coupon surface, the weight gain or loss from either iron or zinc corrosion products could not be differentiated. Although the ASTM G01-03 standard was helpful in selecting appropriate chemicals and procedures to remove both types of corrosion products, one could not be retained on the surface while dissolving the other. In particular, the zinc corrosion products were very difficult to remove. Therefore, in order to better understand how much the galvanized coating has corroded after each specified intervals, the coupons were sectioned, metallographically prepared and examined under the SEM. This permitted the investigation on the presence of remaining zinc in the coating and their average thicknesses after the respective exposures.

6.1 Corrosion Progress

The corrosion progress on an IF 1.77 mm non-welded and deformed coupon is shown in Figure 6-1 and 6-2 respectively. After 30 cycles, zinc corrosion products had formed a thin layer of film on both surfaces of the non-welded coupon for both steel types and thicknesses. The same was also observed on those of the non-welded deformed coupons. The surfaces appeared dull and grey rather than shiny. However, no red spots or signs of rust could be visually detected. Despite longer exposure to test cycles, the coupons continued to resist rust formation on the surface. Only a slight build up of rust

was detected near the edges of the coupons after 60 cycles which can be attributed to poor epoxy selection, poor epoxy bonding to the steel near the edges and crevice corrosion from underneath the epoxy coating. This would also account for less than 5 percentage error in terms of gravimetry which is discussed in the next section.

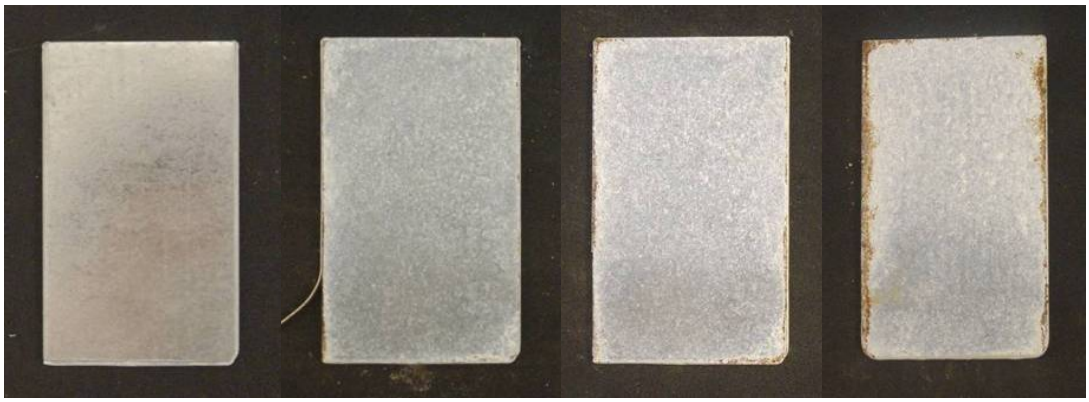

a) b) c) d)

Figure 6-1: Corrosion progress of IF 1.77 mm non-welded coupon after a) 0 b) 30 c) 45 and d) 60 cycles

a) b) c) d)

Figure 6-2: Corrosion progress of IF 1.77 mm non-welded deformed coupon after a) 0 b) 30 c) 45 and d) 60 cycles

In the case of deformed coupons, slight corrosion can be seen on the front surface after 30 cycles at the location where the coupons were inserted in the slots of the rack. This is attributed to crevice corrosion. Likewise, poor bonding between the epoxy and the steel was like the cause of minor corrosion near the deformed coupon edges. No particular build up of rust was observed near the location of the peak strain on the deformed coupon surface other than a film of zinc corrosion products.

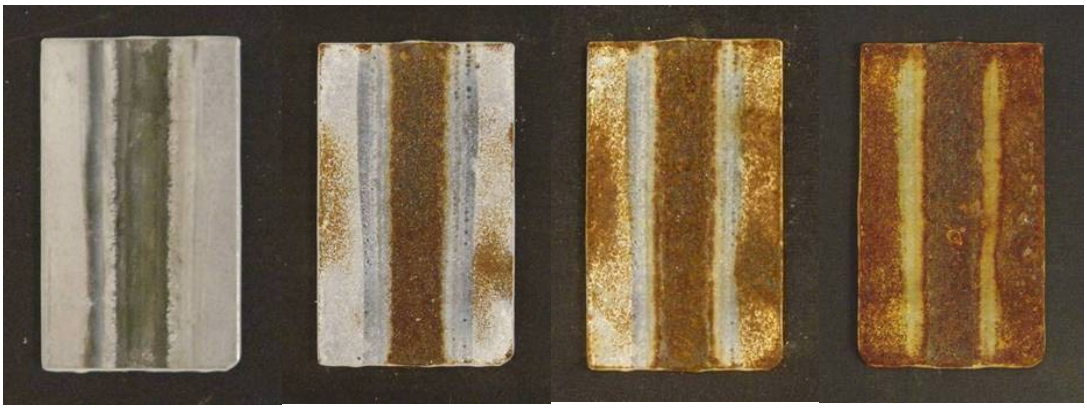

Figure 6-3: Corrosion progress of IF 1.77 mm 9 mm welded coupon after a) 0 b) 30 c) 45 and d) 60 cycles

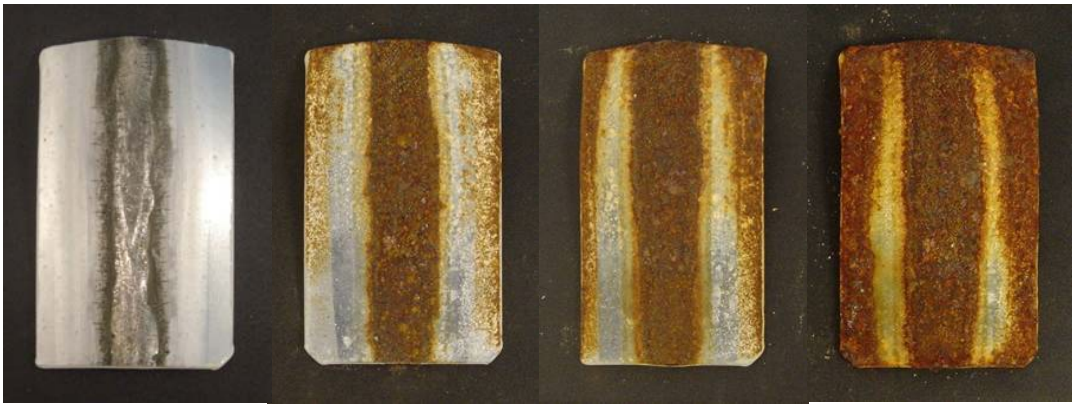

Figure 6-4: Corrosion progress of IF 1.77 mm 9 mm deformed coupon after a) 0 b) 30 c) 45 and d) 60 cycles

In contrast, the exposed weld and substrate after welding for both steels were fully covered with rust after 30 cycles. In fact, the presence of rust in the exposed region of all welded and deformed coupons was observed after just 1 test cycle. Figure 6-3 and 6-4 show the corrosion progress on an IF 9 mm welded and deformed coupon respectively. Although corrosion was much faster than anticipated, it was understood that in humid or dry conditions and with the lack of dissolved zinc ions, protection could not be afforded from the coating to the exposed region; therefore, corrosion on the exposed weld and steel occurred almost instantaneously and was more substantial than in the case of continuous immersion. Furthermore, rust also accumulated outside the exposed region after 30 cycles.

With increasing test cycles, rust continued to penetrate through the thin film of zinc corrosion products and expand in surface area. Surprisingly, the HAZ on both welded and deformed coupons resisted rust build up and endured corrosion attack after 60 cycles. The locally annealed coating in the HAZ showed minimal red rust and only a slight yellow tint. It is suspected that the yellow colour was contributed by corrosion products from the Fe-Zn compounds. Hadden (1952) had also observed such an appearance when his heat treated galvanized steels were exposed to atmospheric conditions. But yellow gradually changed to black. Comparing the corrosion performance of the two steel grades, it was noticed that more rust appeared on the HSLA than on the IF steel, for both welded and deformed coupons.

6.2 Weight Gain/Loss Measurements

The difference between the initial and corroded coupon weight is plotted for each exposed width for both steel grades and thicknesses. While both weight gain and loss were observed, the former were recorded most of the time. Weight loss would be observed if the corrosion products were removed from the coupon surface or dissolved in the solution during the immersion period. However, with a significant amount of moisture in the corrosion chamber, the iron corrosion products were able to absorb it and adhere to the coupon surface, resulting in weight gain rather than loss. The zinc corrosion products are known to adhere tightly to the coupon surface which makes them rather difficult to clean or remove.

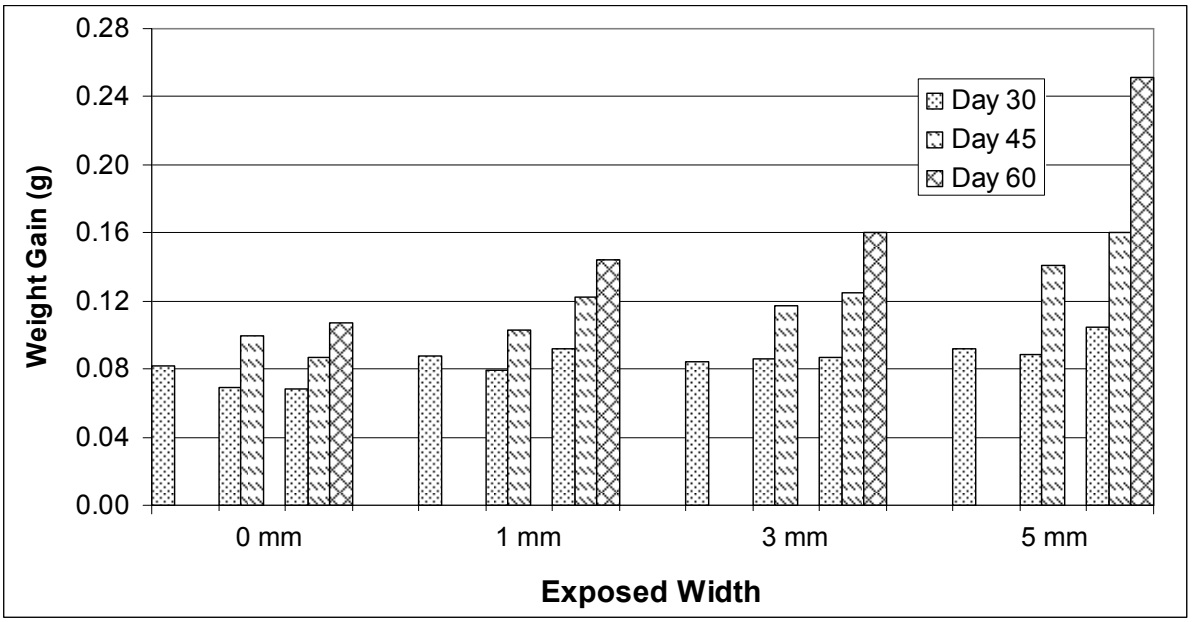

Figure 6-5: Weight measurements on IF 0.77 mm welded coupons

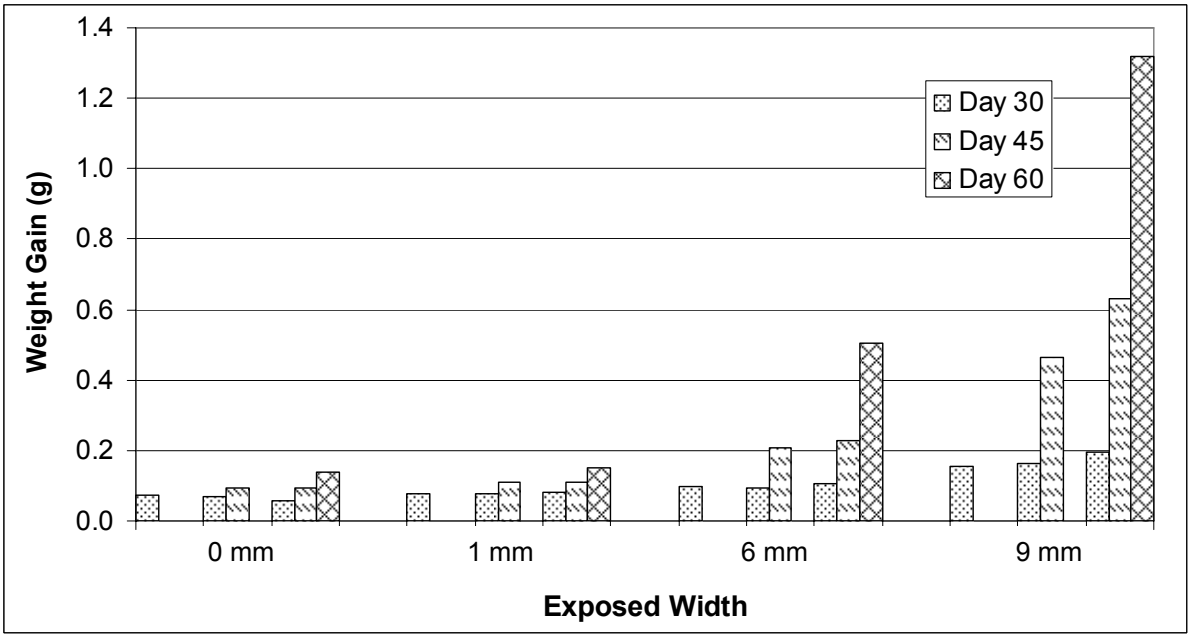

Figure 6-6: Weight measurements on IF 1.77 mm welded coupons

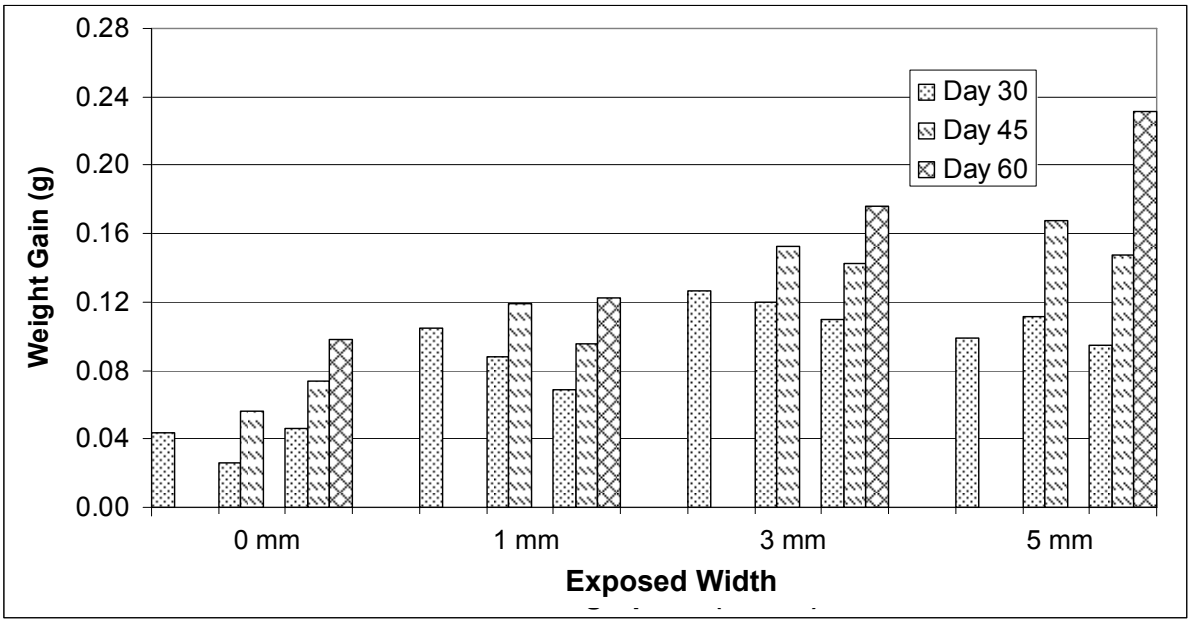

Figure 6-7: Weight measurements on HSLA 0.77 mm welded coupons

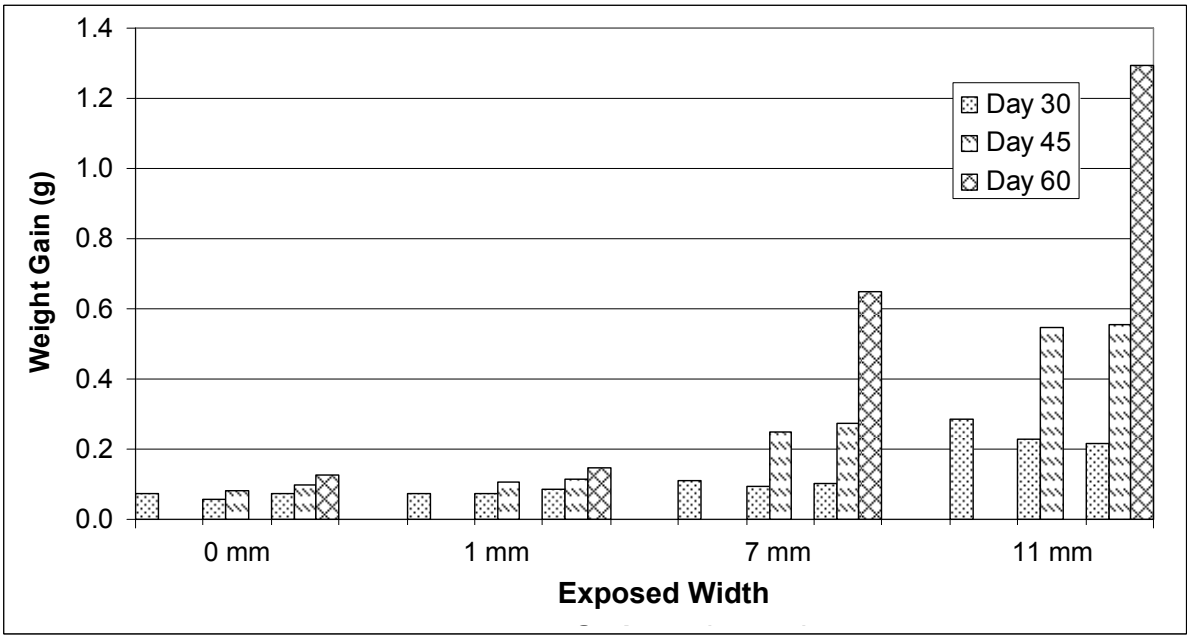

Figure 6-8: Weight measurements on HSLA 1.77 mm welded coupons

The weight measurements on IF 0.77 mm welded coupons show that after 60 cycles, 0.16 and 0.25 g were gained on the 3 and 5 mm coupon respectively in Figure 6-5. The rate at which weight gain developed over time was relatively linear. There was a slight increase in weight gain with increased exposed width, however, the difference is small. On average, the corrosion performance of these coupons can be considered to be similar, irrespective of FZ width.

As illustrated in Figure 6-6, IF 1.77 mm welded coupons show that while the 0 and 1 mm coupons had very close weight gains, there was a considerable increase in weight for the 6 and 9 mm coupons particularly after 30 cycles. This is likely due to a much wider unprotected width which assisted corrosion on the substrate. But more importantly, the increase in weight gain became more exponential as test cycles increased for the 6 and 9 mm coupons. After an exposure of 60 cycles, the 9 mm coupon revealed a weight gain of 1.32 g or more than five times that on a 5 mm coupon of 0.77 mm in the previous Figure.

Similar weight gain trends were also observed on HSLA coupons. Results from Figure 6-7 and 6-8 indicate that values from both thicknesses were very close to those found on IF coupons. The 3 and 5 mm coupons exhibited a weight gain of 0.18 and 0.23 g respectively after 60 cycles. With the HSLA 0.77 mm welded coupons, the increase in weight gain as a result of increased exposed width was slightly higher than that of IF ones. On HSLA 1.77 mm welded coupons, while 0 and 1 mm exhibited comparable weight gains both 7 and 11 mm showed a significant weight increase with longer exposures. After 60 cycles, the 11 mm coupon gained 1.30 g which is also more than 5 times that on the 5 mm coupon.

Unlike welded coupons, the weight measurements on IF deformed 0.77 mm ones were rather inconsistent as Figure 6-9 shows. Both weight loss and weight gain were observed on the 0 and 5 mm coupons and there was a greater scatter. An exposed width of 3 mm showed the most weight gain among the 0.77 mm coupons despite having a narrower exposed width than the 5 mm. More inconsistency was revealed when it was found that the deformed 3 mm coupon had almost 4 times as much weight gain over the welded 3 mm coupon whereas the deformed 5 mm coupon had similar weight gain as the welded counterpart after 60 cycles. The average weight gain/loss of the coupons and the general trend after 30, 45 and 60 cycles is included in Appendix B for reference.

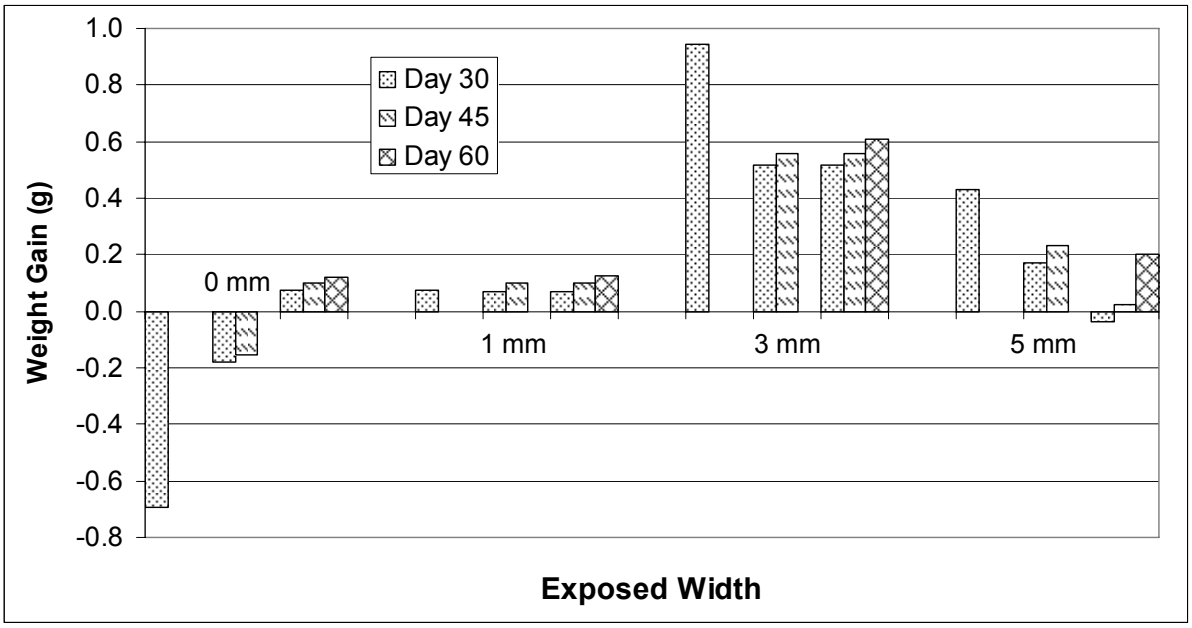

Figure 6-9: Weight measurements on IF 0.77 mm deformed coupons

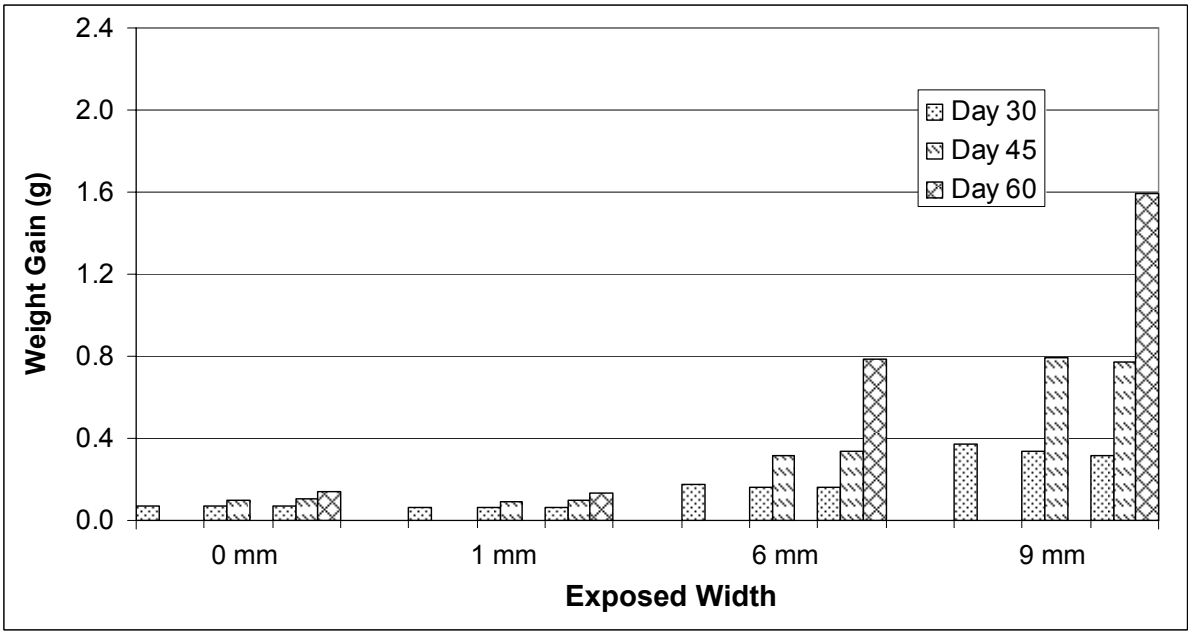

Figure 6-10: Weight measurements on IF 1.77 mm deformed coupons

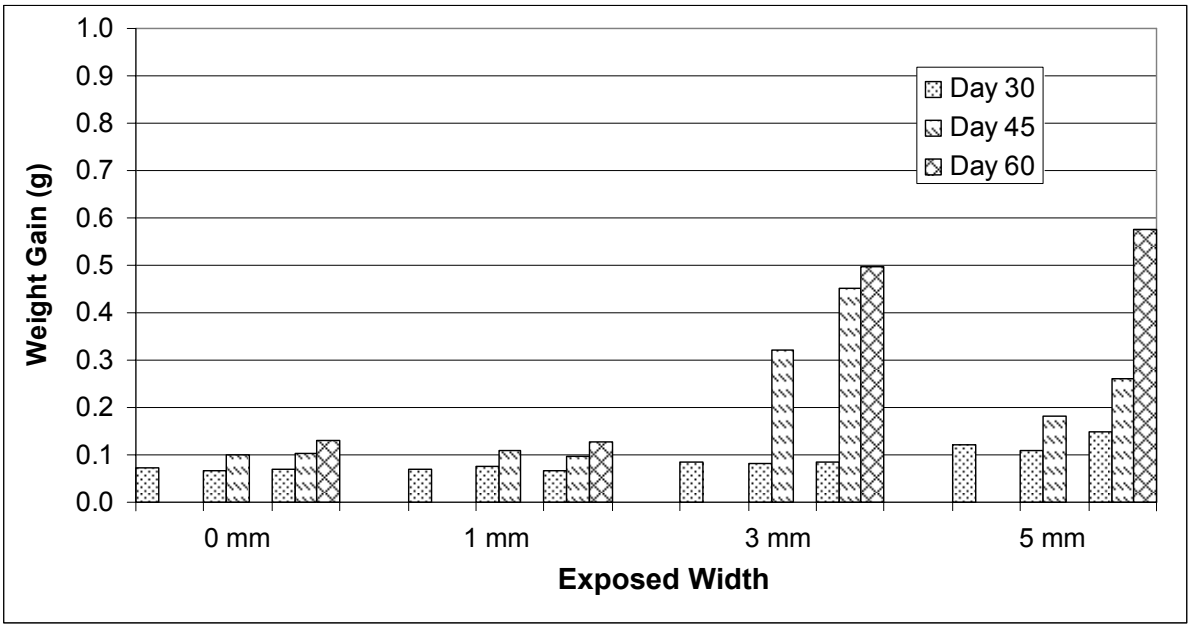

Figure 6-11: Weight measurements on HSLA 0.77 mm deformed coupons

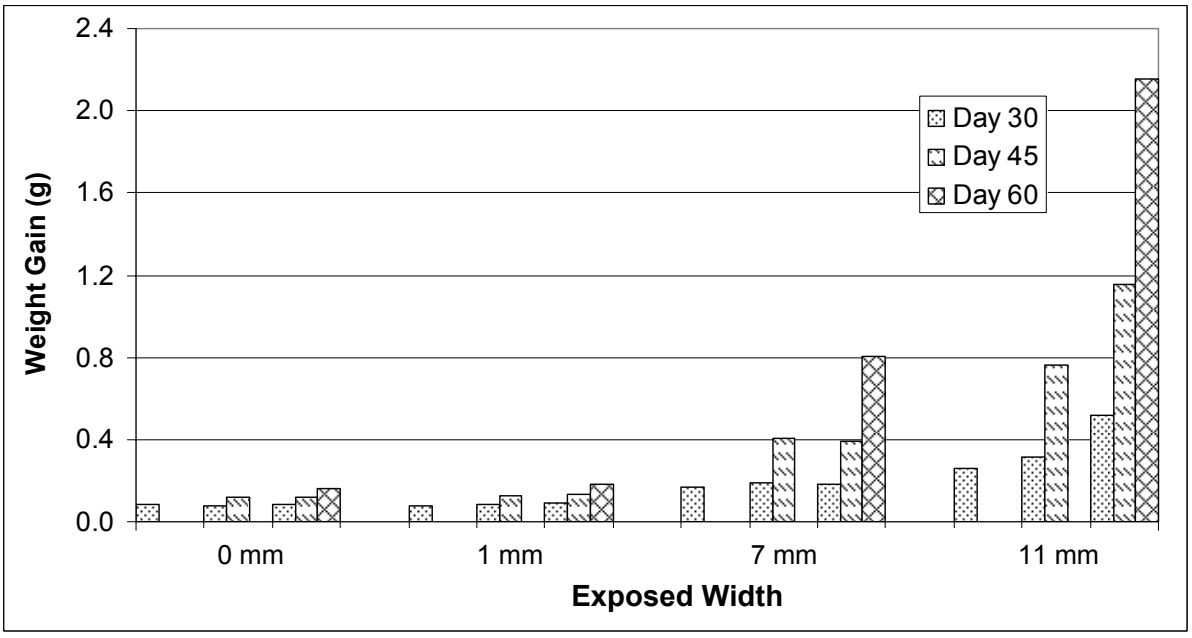

Figure 6-12: Weight measurements on HSLA 1.77 mm deformed coupons

For IF deformed 1.77 mm coupons, results shown in Figure 6-10 were similar to their welded counterparts. Again, comparable weight gains were observed on the 0 and 1 mm coupons while a significant increase in weight were seen on the 6 and 9 mm coupons. At 60 cycles, 0.79 g and 1.60 g were gained on the 6 and 9 mm coupons which are about 56% and 21% increase from that on the welded 6 and 9 mm ones. This confirms the deterioration of the corrosion resistance on a galvanized coating after stretch forming.

Surprisingly, for HSLA deformed 0.77 mm coupons, the 3 mm coupons showed greater weight gains at 45 cycles than the 5 mm ones, but after 60 cycles, Figure 6-11 shows that the 3 mm coupon had little increase in weight gain whereas the 5 mm coupon doubled its weight gain from that at 45 cycles. Their respective values were 0.50 and 0.58 g and were more than twice the weight gain of the welded ones. Compared to the IF deformed 0.77 mm coupons, better consistency was observed with the HSLA deformed 0.77 mm ones.

Finally, Figure 6-12 shows more consistent results of HSLA deformed 1.77 mm coupons with similar trends to those of the welded ones in Figure 6-8. Not only did the 0 and 1 mm coupons perform equally after 60 cycles, they were also very close to those of welded ones after the same exposure. On the other hand, with a weight gain of 0.80 g, the 7 mm deformed coupon exhibited a 24% increase from the 7 mm welded one. With the largest exposed width, the 11 mm deformed coupon showed a weight gain of 2.15 g and a 66% increase compared to that of the 11 mm welded coupon at 60 cycles.

In summary, it can be seen that gravimetry results were difficult to interpret since weight gain and loss were not always consistent. Nonetheless, general remarks can be made with respect to the exposed width and deformation. The 1 mm welded coupons, produced using the Nd:YAG laser, performed reasonably close to that of non-welded ones regardless of steel grade or thickness. On coupons welded by the diode laser, the increase from 5 to 9 mm exposed width on welded IF steel, or 5 to 11 mm on welded HSLA steel, caused an increase of more than 5 times in weight gain. Stretch forming generally caused an increase in gain weight from that of welded coupons. This is likely due to the increase in the surface area of the exposed region. But while the effect is small on the non-welded and 1 mm coupons, it was much greater on larger exposed widths.

6.3 Reduction of Zinc Coating in Accelerated Test

Microscopy of mounted and polished cross sections of coupons after cyclic corrosion testing allowed the thickness of the remaining zinc coating after 30, 45, and 60 cycles to be measured. Due to the non-uniform nature of corrosion, it was observed that many regions of the galvanized coating had already corroded completely and been displaced by corrosion products. This is shown in Figure 6-13 where parts of the coating remained intermittently. It can be seen that the corrosion products have fully covered both the remaining coating and the underlying steel. As a result, measurements could only be made in regions where the galvanized coating still remained. The average thickness of the remaining coating across the surface of the coupon for both steels and thicknesses is summarized in Table 6-1.

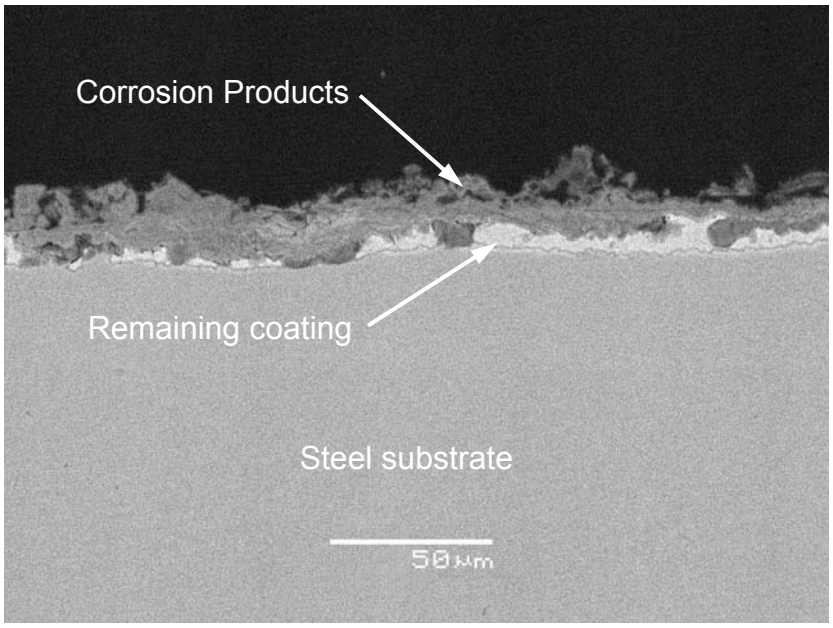

Figure 6-13: Example of corroded coating with corrosion products

The nominal coating weight for IF and HSLA steel before corrosion were 11.5 µm and 10.5 µm respectively. Although the reduction in coating thickness with increased number of cycles in the corrosion chamber was not as significant as anticipated, a decreasing trend was more apparent on

deformed coupons than on non-welded ones. It is believed that the adherent zinc corrosion products created a barrier for the remaining coating against the environment and offered partial protection and resistance so that further dissolution or oxidation was reduced or minimized.

Table 6-1: Average thickness of the remaining galvanized coating in µm on non-welded coupons after 30, 45, and 60 cycles of SAE J2334

Steel	Thickness	Cycles		
		30	45	60
IF	0.77 mm	8.6	7.9	7.6
	1.77 mm	9.4	7.8	7.5
HSLA	0.77 mm	8.7	7.6	7.2
	1.77 mm	9.3	9.0	7.4

Table 6-2: Average thickness of the remaining galvanized coating in µm on deformed coupons after 30, 45, 60 cycles of SAE J2334

Steel	Thickness	Cycles		
		30	45	60
IF	0.77 mm	7.7	6.9	5.3
	1.77 mm	9.3	7.7	6.5
HSLA	0.77 mm	8.6	7.1	5.7
	1.77 mm	8.6	7.6	6.8

Upon examining the cross section of a 9 mm welded sample with 60 cycles of exposure, it was found that Fe-Zn intermetallics still remained on the surface of the HAZ region. Figure 6-14 shows that the eta matrix had corroded leaving the delta layer on the surface to further protect the underlying steel. This confirms the corrosion progress seen in Figures 6-3 and 6-4 where the HAZ persisted against red rust formation. It also demonstrates the superior corrosion resistance of Fe-Zn alloy phases, specifically the delta phase in this example, over the pure eta phase zinc coating.

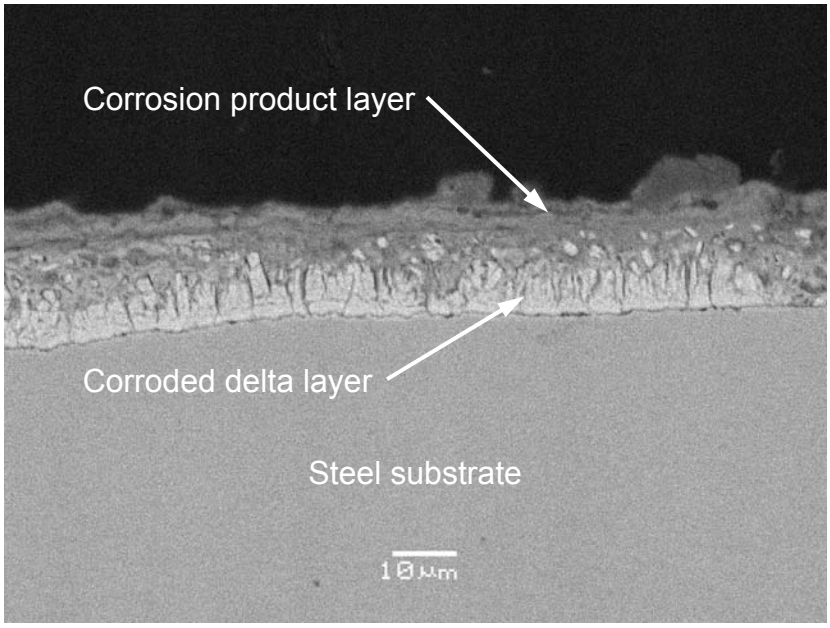

Figure 6-14: Corroded surface in the HAZ on a 9 mm coupon after 30 cycles

CHAPTER 7
IDENTIFICATION OF CORROSION PRODUCTS

The identification of both iron and zinc corrosion products was performed using both X-Ray diffraction (XRD) and Raman spectroscopy. Analyses were done at the exposed region, the HAZ, and the HDG coating before and after the cyclic corrosion testing so that a comparison could be made.

7.1 XRD

Figure 7-1 shows the XRD pattern on the HDG coating which corresponded to that of pure zinc. With the build up of zinc corrosion products on the non-welded coupon surface, it was expected that zinc oxide (ZnO) and zinc hydroxy chloride (ZHC) ($ZnCl_2[Zn(OH)_2]_4$) would be detected. Both compounds were identified by XRD results shown in Figure 7-2. In addition, hydrozincite ($[ZnCO_3]_2[Zn(OH)_2]_3$) was also detected in the white corrosion products of zinc. The formation of calcium carbonate ($CaCO_3$) and its presence in the corrosion products is likely due to the use of calcium chloride and sodium bicarbonate in the SAE J2334 test solution. Calcium carbonate would also explain the overall protection offered by the corrosion products, the strong adherence to the surface, and difficulty in removing it. It is believed that the build up of the corrosion product layer provides a diffusion barrier against oxygen and slows down the corrosion rate for the underlying steel.

The diffraction pattern for the exposed weld is shown in Figure 7-3. An oxide film was detected on the surface of the exposed weld consisting of Wuestite (FeO), Hematite (α-Fe_2O_3) and Magnetite (Fe_3O_4) and was bluish grey in appearance. Despite being a very thin layer, the sound formation of the oxide film provided some corrosion resistance and probably inhibited rust accumulation in the exposed region more so than at the coating steel interface during continuous immersion.

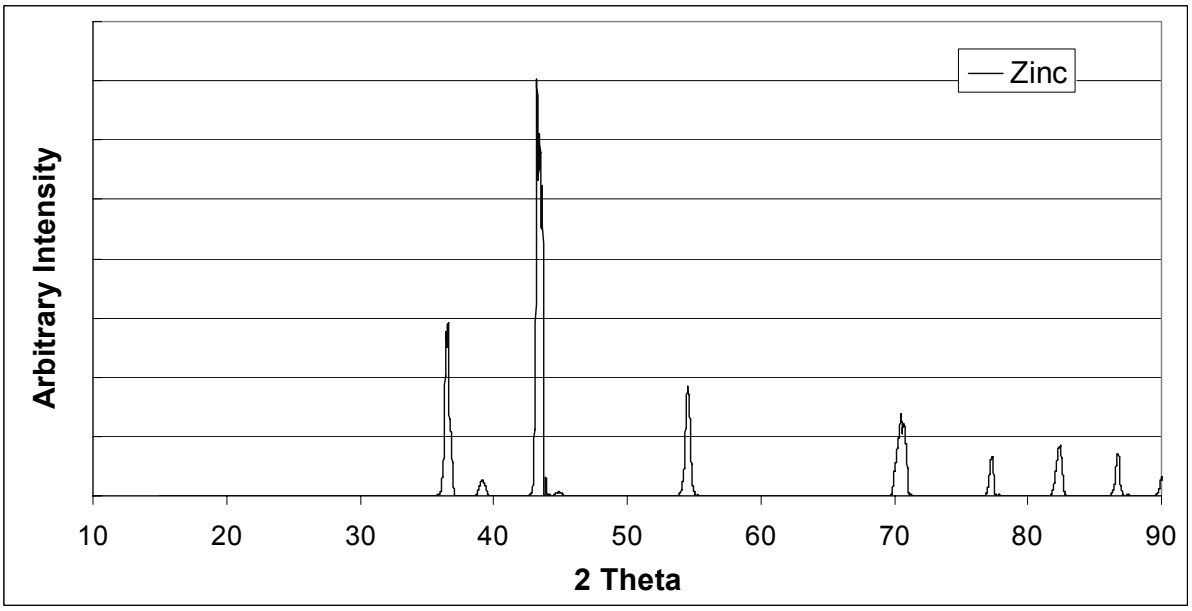

Figure 7-1: XRD of the original HDG coating before corrosion test

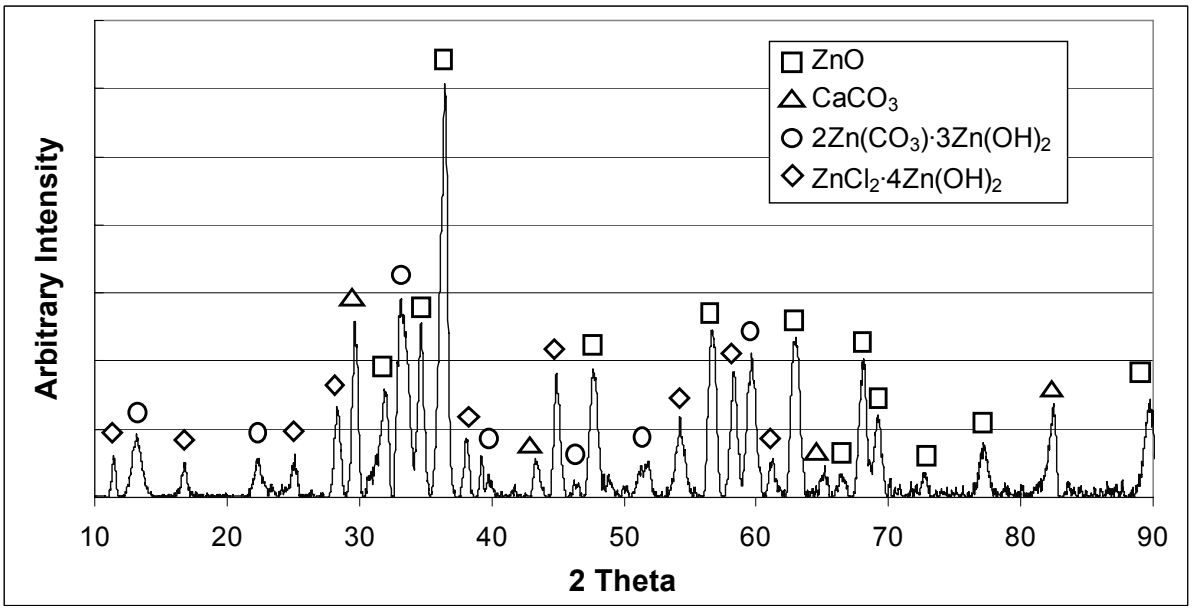

Figure 7-2: XRD of the corroded HDG coating after 60 cycles of SAE J2334

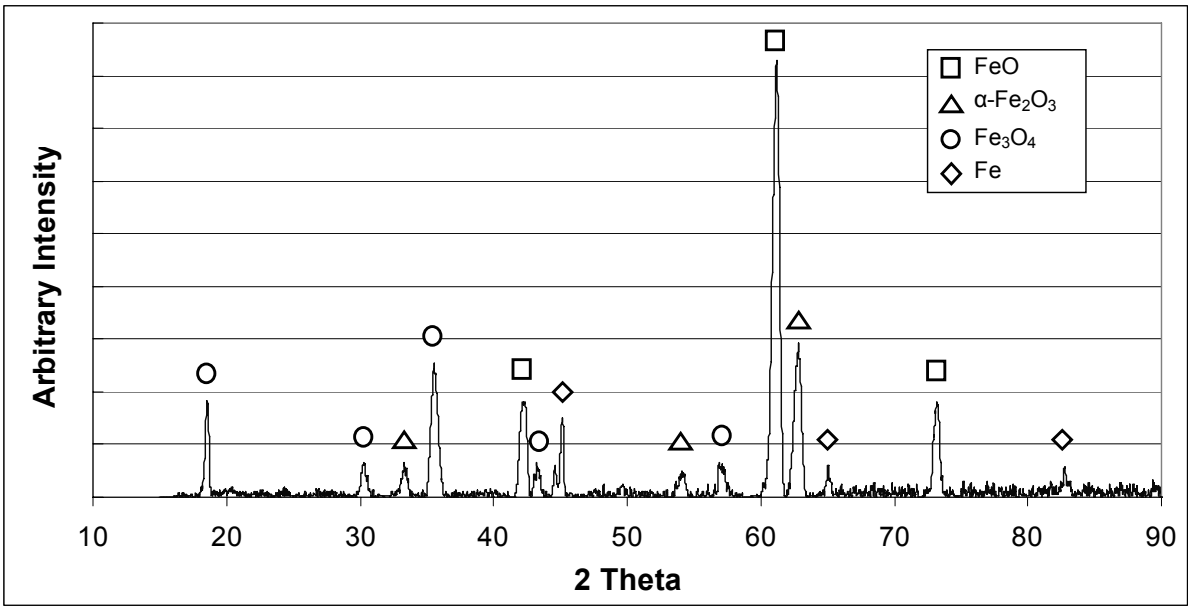

Figure 7-3: XRD of the surface of the exposed region of a welded coupon

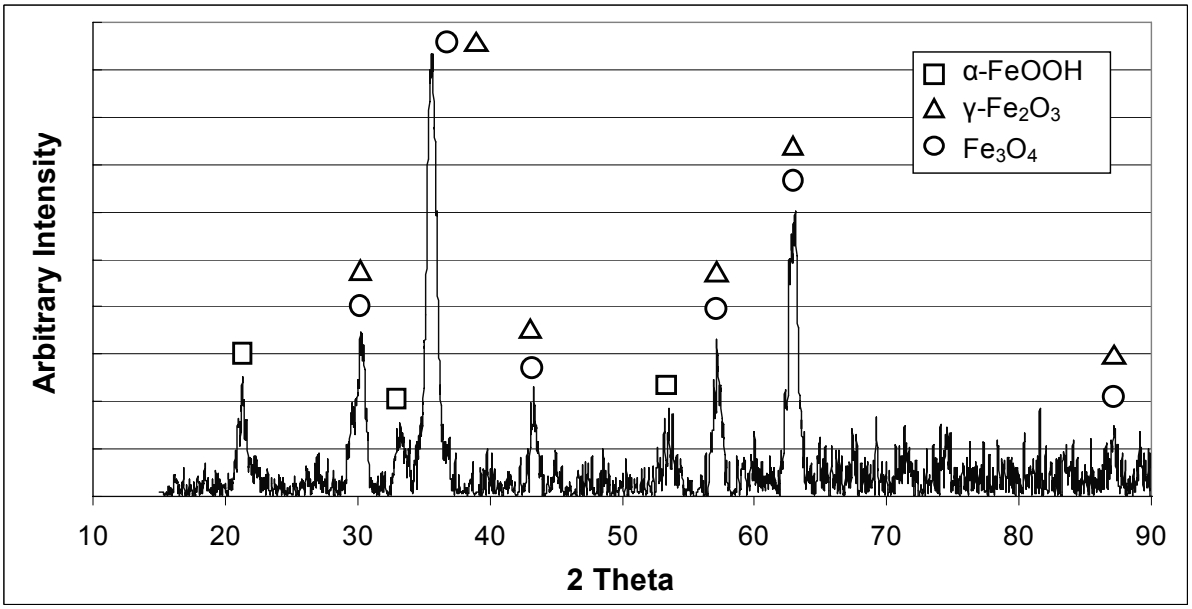

Figure 7-4: XRD of iron corrosion products in the exposed region of a welded coupon after 60 cycles of SAE J2334

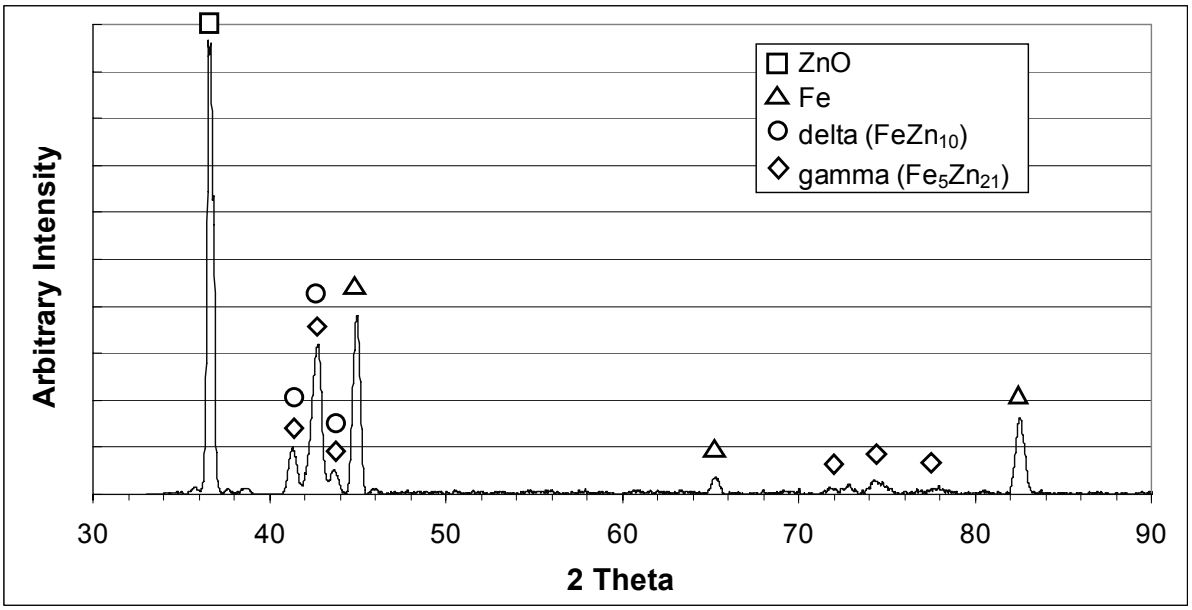

Figure 7-5: XRD of the surface of the HAZ of a diode laser welded coupon

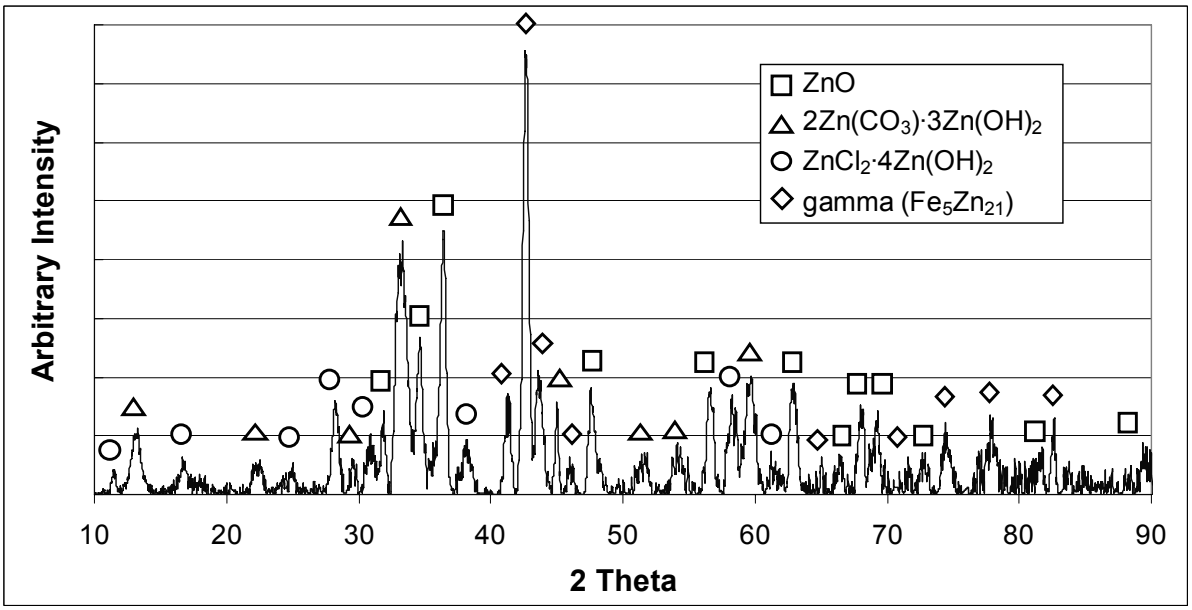

Figure 7-6: XRD of the corroded coating in the HAZ region of a diode laser welded specimen after 60 cycles of SAE J2334

After 60 cycles of SAE J2334 testing, significant corrosion in the exposed region have developed. Red rust obtained from the accumulation was analyzed in powder form. The powder diffraction pattern in Figure 7-4 shows that it consisted of goethite (α-FeOOH), Maghemite (γ-Fe_2O_3) and Magnetite (Fe_3O_4).

Using the SEM and EDS described in chapter 4, it was previously observed that the growth of the delta phase Fe-Zn intermetallic was the most dominant in the locally annealed region of the coating and hence, was more easily identified than the gamma phase. However, the presence of the gamma phase was confirmed by XRD on the coating adjacent to the exposed steel substrate of a diode laser welded specimen in addition to the delta phase Fe-Zn alloy, as illustrated by Figure 7-5. Moreover, the formation of ZnO suggests local oxidation in the annealed part of the coating. After 60 cycles of SAE J2334, it was observed that corrosion products on the annealed part of the coating appeared to be yellow rather than red. The diffraction pattern in Figure 7-6 confirmed the absence of iron oxides and iron oxide hydroxides in this region and instead, detected zinc oxide (ZnO), hydrozincite, and ZHC, commonly formed on a corroded zinc surface. The gamma phase Fe-Zn alloy was also detected.

7.2 Raman Analysis

Complementary to XRD, Raman is capable of in-situ analysis on the corrosion species from both zinc and iron. The Raman spectrum in Figure 7-7 was obtained from the white corrosion product on a non-welded coupon after 80 days of immersion in 0.1 M NaCl solution. Similar to XRD, it was found that the peaks corresponded to different compounds rather than one. They were identified as ZnO, ZHC and $ZnCO_3$. This further confirms the complexity of corrosion and the effects of dissolved oxygen and carbon dioxide on the formation of zinc corrosion products. But contrary to publications (El-Mahdy, Nishikata et al. 2000; Ohtsuka and Matsuda 2003; Yadav, Nishikata et al. 2004), the formation of zinc hydroxy chloride (ZHC) in the presence of chlorides in solution was not as significant as expected. Also, hydrozincite was not detected either as XRD had indicated.

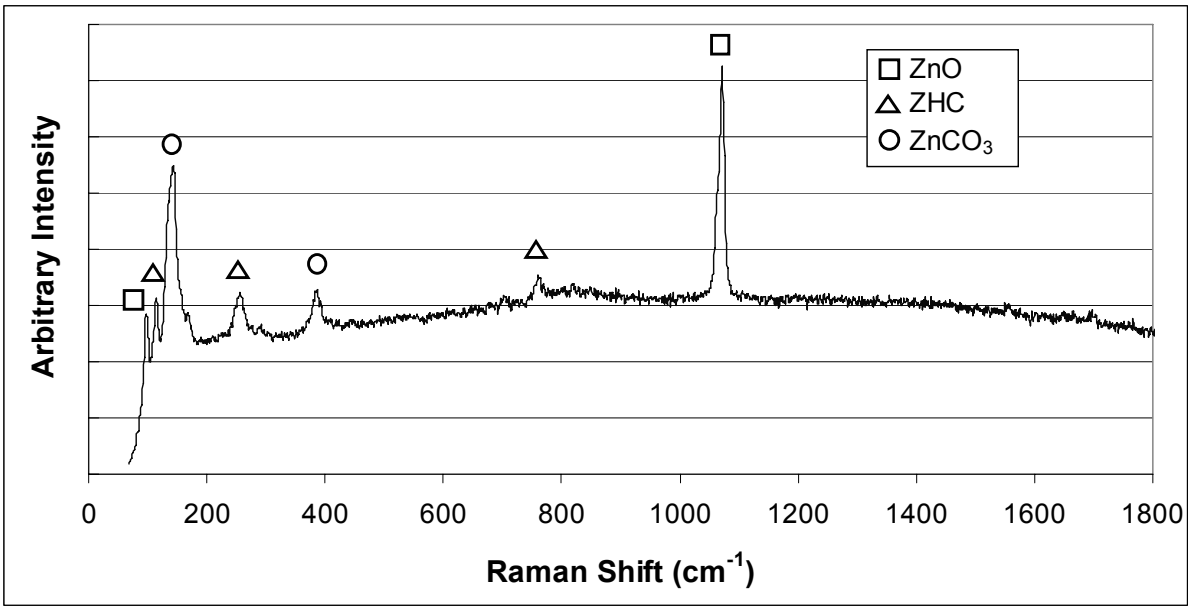

Figure 7-7: Raman spectrum on zinc corrosion products of a non-welded coupon after 80 days of immersion in 0.1M NaCl

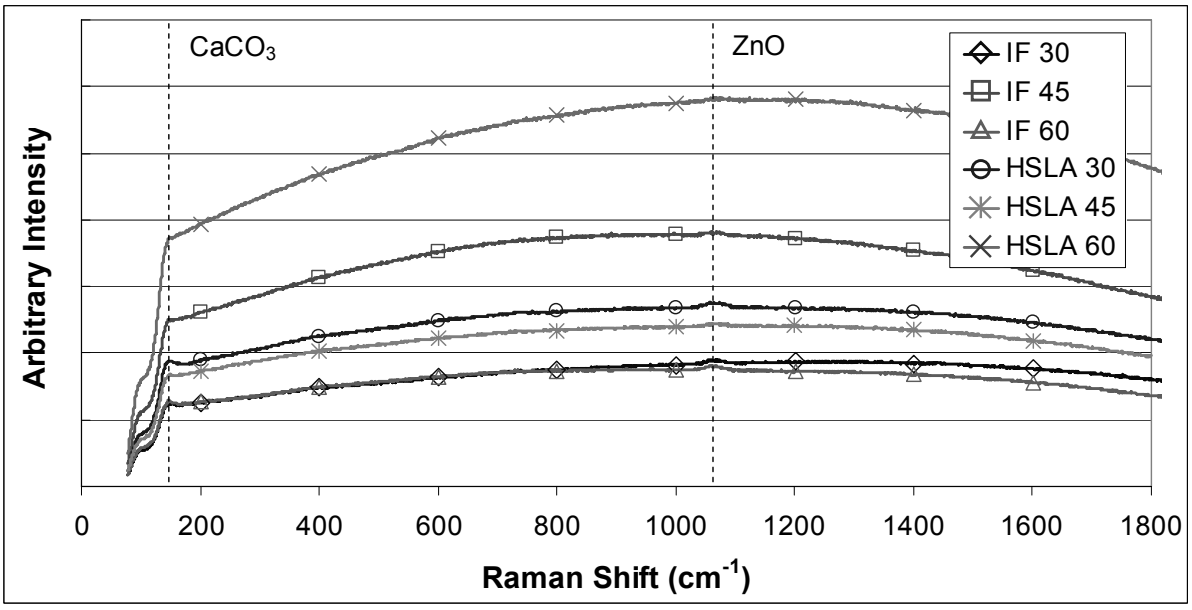

Figure 7-8: Raman spectrum on the corroding surface of IF and HSLA coupons exposed to 30, 45, and 60 cycles of SAE J2334

Raman spectra were also obtained from IF and HSLA coupons exposed to 30, 45, and 60 cycles of SAE J2334. Unfortunately, as shown in Figure 7-8, the spectra exhibited significant fluorescence for both IF and HSLA coupons and for each exposure. Nonetheless, two peaks could be distinguished at 153 and 1065 cm^{-1} which are characteristics of $CaCO_3$ and ZnO respectively. It is possible that the short wavelength of the Raman laser was particularly prone to fluorescence, in which case, a longer wavelength laser may reduce this effect (Fagan 2008). It is also possible that the synergistic effect from different compounds making up the corrosion film caused the Raman spectra to fluoresce rather than detecting peaks for the compounds.

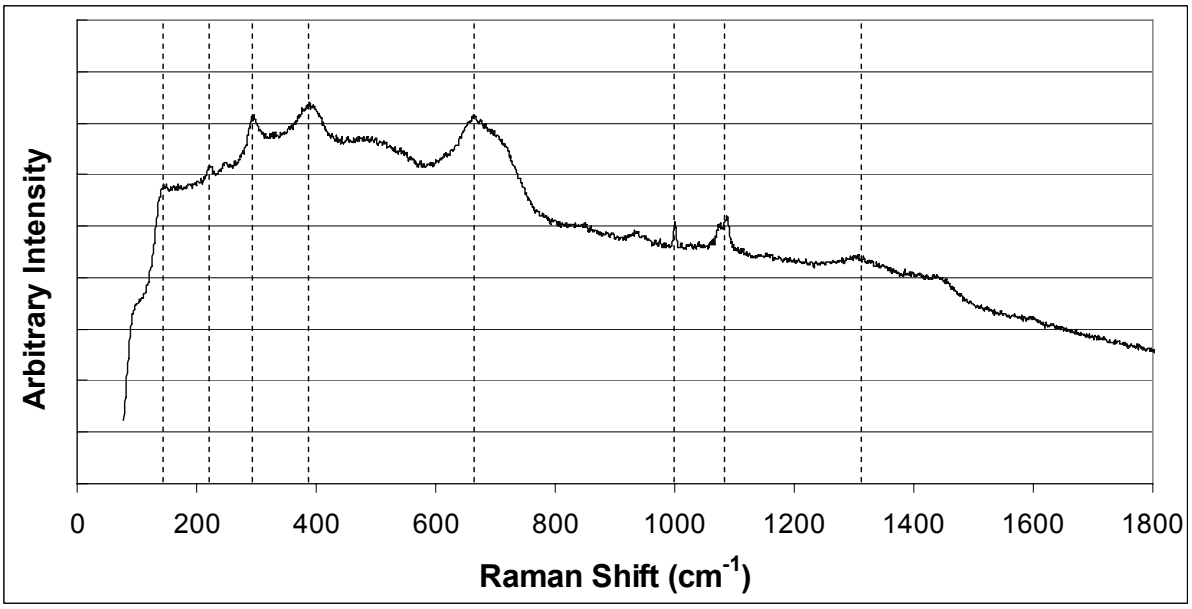

Figure 7-9: Raman spectra on rust accumulation in the exposed region

Table 7-1: Identification of Raman peaks in Figure 7-9

Peak (cm^{-1})	153	224	295	396	663	1000	1086	1316
Compound	$CaCO_3$	α-Fe_2O_3	α-Fe_2O_3	γ-Fe_2O_3	Fe_3O_4	α-FeOOH	$CaCO_3$	α-Fe_2O_3

The Raman spectrum in Figure 7-9 obtained on the rust accumulation in the exposed region after the cyclic corrosion test showed better correlation to that identified by XRD. Different peaks were detected and their corresponding compounds were identified and presented in Table 7-1. The corrosion products from iron included goethite (α-FeOOH), Hematite (α-Fe_2O_3), Maghemite (γ-Fe_2O_3), and Magnetite (Fe_3O_4). Calcium carbonate was also detected by Raman spectroscopy which confirmed its formation due to the addition of calcium chloride and sodium bicarbonate in the test solution.

CHAPTER 8
CONCLUSIONS

The objective of this study was to determine how laser welding and stretch forming affect the corrosion performance of hot-dip galvanized (HDG) steel sheets without the application of paint coatings. Using methods of continuous immersion and wet-dry cycles, it was concluded that:

1. The zinc coating was able to effectively protect a chemically exposed region of steel on the galvanized sheet as wide as 9 mm in 0.1 M NaCl solution.

2. Nd:YAG laser welding had a negligible effect on the corrosion performance of HDG steel under both immersed and wet-dry conditions.

3. Diode laser welded coupons, particularly those with exposed widths of 6 and 9 mm exhibited slightly lower zinc peak corrosion rates than that of Nd:YAG laser welded ones.

4. Both zinc corrosion products and the Fe-Zn intermetallics produced in the heat affected zone of the weld offered considerable protection to the steel substrate and demonstrated substantial corrosion resistance to rust formation.

5. Under wet-dry conditions and inadequate amounts of zinc ions, the galvanized coating was unable to protect the exposed steel and rust formed after one test cycle using the SAE J2334 standard.

6. Evaluation of the corrosion performance using gravimetry was unsuccessful due to the build up of very adherent zinc and iron corrosion products and the inability to differentiate the weight gain/loss from the two.

7. Weight gain measurements showed that the increase as a function of increasing exposed width changed from a linear to an exponential relationship as the exposure increased from 30 to 60 test cycles.

8. No significant difference was observed between the corrosion rates of IF and HSLA steel.

9. Biaxial strain generally caused higher zinc peak corrosion rates and greater rust accumulation on stretch formed coupons than those seen on undeformed laser welded ones.

10. The effect of peak strains on the corrosion rate or rust formation both along and across the weld was inconclusive using the current test method. Further investigations are recommended.

11. While rust consisted of α-FeOOH, γ-Fe_2O_3 and Fe_3O_4, the white corrosion products of zinc were made up of ZnO, $[ZnCO_3]_2[Zn(OH)_2]_3$, and $ZnCl_2[Zn(OH)_2]_4$.

12. In the absence of paint coatings, the formation of corrosion products were capable of passivating the surface and reducing the corrosion rate of the galvanized coating significantly in order to protect the underlying steel.

13. On actual tailor welded blanks, the large zinc to steel area ratio would generate significantly greater galvanic protection than that experienced by the comparatively small test coupons.

14. An annealed coating with a significant growth of the delta phase Fe-Zn layer, similar to the microstructure of a commercially galvannealed coating, performed superior than that of a pure zinc coating. Therefore, for those components that will not be paint coated and are used as interior parts such as the inner door panel, annealing is encouraged at the expense of increased cost.

15. During stamping of tailor welded blanks, the deterioration of the coating could be reduced if the welds are placed away from regions that will be subjected to high deformation or biaxial strains. Such designs would essentially increase the corrosion resistance of the coating.

CHAPTER 9
RECOMMENDATIONS

To investigate the effect of paint coatings or the corrosion performance of a specific type of epoxy, it is recommended to test laser welded and deformed specimens in the fully painted condition according to SAE J2334.

Since the electrochemical reactions taking place on a HDG surface are likely to be localized, a micro tip reference electrode is required to distinguish such fine potential variations across the surface. While the scanning reference electrode technique (SRET) (Vyas and Isaacs 1978) has been applied successfully to map out contours of the corrosion potential across the weld, the scanning vibrating electrode technique (SVET) (Isaacs 1988) allows highly sensitive measurements of local current intensities on an active corroding surface in solution. Hence, the galvanic interaction at the zinc-steel interface or in the locally annealed part of the coating may be characterized. Further, these techniques may prove to be useful in determining local effects from peak strains in deformed specimens in relation to the original HDG coating.

Opportunities exist to further examine the corrosion behaviour of coupons when subjected to deaerated conditions. This would simulate zinc surfaces in confined spaces such as inside crevices of hem flanges or paint blisters where delamination has occurred. The lack of oxygen could foster different corrosion mechanisms as well as corrosion products from those found in the current study.

It is recommended to study the corrosion performance as a function of percentage biaxial strain in which case varying limited dome heights should be used. In addition, the effect of strain rate on the corrosion rate could provide practical knowledge for the stretch forming process.

To further understand the effect of oxide formation in the fusion zone after laser welding, it would be useful to observe how varying percentages of oxygen addition to the argon shielding gas would influence the formation of the oxide film and whether a difference in the corrosion resistance or the corrosion protection afforded to the exposed weldment can be determined. The oxide film should be characterized using analytical tools such as SEM and XRD.

A longer wavelength laser should be used when conducting in-situ Raman spectroscopy on corrosion species. This could potentially eliminate fluorescence and reveal more peaks during analysis.

REFERENCES

ASTM G 01-03. “Standard Practice for Preparing, Cleaning, and Evaluating Corrosion Test Specimens.” American Society for Testing and Materials International. West Conshohocken, PA, USA.

ASTM B 487 – 85 (Reapproved 2007). “Standard Test Method for Measurement of metal and Oxide Coating Thickness by Microscopical Examination of Cross Section.” American Society for Testing and Materials International. West Conshohocken, PA, USA.

SAE J2334 – OCT 2002. “Cosmetic Corrosion Lab Test.” Society of Automotive Engineers International, USA

(1998). "Ultra Light Steel Auto Body - Overview Report." 2006, from http://was.iconicweb.com/assets/attachments/ULSAB_Overview_Report.pdf.

(2001). Tailor welded blank applications and manufacturing - A state of the art survey. Southfield, Michigan, The Auto/Steel Partnership.

(2002). "Automotive Steel Design Manual Rev.6.1." 2008, from http://www.a-sp.net/database/default.asp?doc=28.

Aristotile, R. and M. Fersini (1999). "'Tailored blanks' for automotive components. Evaluation of mechanical and metallurgical properties and corrosion resistance of laser-welded joints." Welding International 13(3): pp.16~25.

Baldwin, K. R., C. J. E. Smith and M. J. Robinson (1995). "Cathodic Protection of Steel by Electrodeposited Zinc-Nickel Alloy Coatings." Corrosion 51(12): pp.932~940.

Bandyopadhyay, N., G. Jha, A. K. Singh, T. K. Rout and N. Rani (2006). "Corrosion behaviour of galvannealed steel sheet." Surface & Coating Technology 200: pp.4312~4319.

Barranco, V., S. Feliu Jr. and S. Feliu (2004). "EIS study of the corrosion behaviour of zinc-based coatings on steel in quiescent 3% NaCl solution. Part 1:directly exposed coatings." Corrosion Science 46: pp.2203~2220.

Bernard, M. C., A. H. Goff and N. Phillips (1995). "In Situ Raman Study of the Corrosion of Zinc-Coated Steel in the Presence of Chloride." Journal of Electrochemistry Society 142(7): pp.2162~2170.

Berndsen, H., F. Friedel, R. Petzold, M. Meurer, K. Benedens and K. P. Imlau (2003). "Coated Steel Sheet – A Metallographic Challenge." Praktische Metallographie 40(1): pp.25~33.

Bliedtner, J., T. Heyse, D. Jahn, G. Michel, H. Mueller and D. Wolff (2001). "Advances in Diode Lasers Increase Weld Penetration." Welding Journal 80(6): pp.47~52.

Bocos, J. L., F. Zubiri, F. Garciandia, J. Pena, A. Cortiella, J. M. Berrueta and F. Zapirain (2005). "Application of the diode laser to welding on tailored blanks." Welding International 19(7): pp.539~543.

Callister Jr., W. D. (1997). Materials Science and Engineering, an Introduction. Fourth Edition. New York, New York, John Wiley & Sons, Inc.

Campbell, H. S., J. F. Stanners and K. O. Watkins (1965). "Effect of heat treatment on the protective properties of zinc coatings on steel." Journal of Iron and Steel Institute 203(3): pp.248~251.

Cullity, B. D. (1978). Elements of X-Ray Diffraction, Second Edition, Addison-Wesley Publishing Company Inc.

Dionne, S. (2006). "The Characterization of Continuous Hot-Dip Galvanized and Galvannealed Steels." Journal of the Minerals, Metals, and Materials Society 58(3): pp.32~40.

Duley, W. W. (1999). Laser Welding. New York, New York, John Wiley & Sons, Inc.

El-Mahdy, G. A., A. Nishikata and T. Tsuru (2000). "Electrochemical corrosion monitoring of galvanized steel under cyclic wet-dry conditions." Corrosion Science 42: pp.183~194.

Fagan, R. (2008). Personal Communication. Waterloo, Ontario.

Fedrizzi, L. and P. L. Bonora (1993). "Effects of mechanical deformation on electrochemical behaviour of galvanized steel." British Corrosion Journal 28(1): pp.37~42.

Graham, M. P., D. C. Weckman, H. W. Kerr and D. M. Hirak (1996). "Nd:YAG Laser Beam Welding of Coated Steels Using a Modified Lap Joint Geometry." Welding Journal 75(5): pp.162-s~170-s.

Gupta, A. K. and D. R. Kumar (2006). "Formability of galvanized interstitial-free steel sheets." Journal of Materials Processing Technology 172(2): pp.225~237.

Hadden, S. E. (1952). "Effect of annealing on the resistance of galvanized steel to atmospheric corrosion." Journal of Iron and Steel Institute 171(2): pp.121~127.

Howard, K. (2005). "Diode Laser Welding of Aluminum Sheet." Mechanical and Mechatronics Engineering. Waterloo. University of Waterloo. MASc

Isaacs, H. S. (1988). "Measurement of the galvanic corrosion of soldered copper using the scanning vibrating electrode technique." Corrosion Science 28(6): pp.547-558.

Kou, S. (1987). Welding Metallurgy, John Wiley & Sons.

Looi, Y. M., J. R. Flores, C. Kwakernaak and J. H. W. de Wit (2004). "Intergranular corrosion on Nd:YAG laser-welded A653 steel for automotive application." Materials and Corrosion 55(11): pp.831~836.

Marder, A. R. (2000). "The metallurgy of zinc-coated steel." Progress in Materials Science 45: pp.191~271.

Matsunawa, A., M. Mizutani, S. Katayama and N. Seto (2003). "Porosity formation mechanism and its prevention in laser welding." Welding Journal 17(6): pp.431~437.

Moran, J. P., P. R. Ziman and T. R. Kipp (1995). Cosmetic corrosion of painted aluminium automotive body sheet: results from outdoor and accelerated laboratory testing. Philadelphia, PA, American Society for Testing and Materials.

Nacey, T. (2001). "Diode Lasers Offer Welding Advantages." Welding Journal 80(6): pp.28~30.

Oh, S. J., D. C. Cook and H. E. Townsend (1998). "Characterization of iron oxides commonly formed as corrosion products on steel." Hyperfine Interactions 122(1): pp.59~65.

Ohtsuka, T. and M. Matsuda (2003). "In Situ Raman Spectroscopy for Corrosion Products of Zinc in Humidified Atmosphere in the Presence of Sodium Chloride Precipitate." Corrosion 59(5): pp.407~413.

Panda, S. K., D. R. Kumar, H. Kumar and A. K. Nath (2007). "Characterization of tensile properties of tailor welded IF steel sheets and their formability in stretch forming." Journal of Materials Processing Technology 183(2): pp.321~332.

Porter, F. (1991). Zinc Handbook: properties, processing, and use in design. New York, New York, Marcel Dekker Inc.

Pourbaix, M. (1996). Atlas of electrochemical equilibria in aqueous solutions. Toronto, Pergamon Press.

Prosek, T., D. Thierry, C. Taxen and J. Maixner (2007). "Effect of cations on corrosion of zinc and carbon steel covered with chloride deposits under atmospheric conditions." Corrosion Science 49: pp.2676~2693.

Queiroz, F. M. and I. Costa (2007). "Electrochemical, chemical and morphological characterization of galvannealed steel coating." Surface & Coating Technology 201: pp.7024~7035.

Raja, V. S., C. K. Panday, V. S. Saji, S. T. Vagge and K. Narasimhan (2006). "An electrochemical study on deformed galvanneal steel sheets." Surface & Coating Technology 201: pp.2296~2302.

Repp, J. (2002). "Status Update - J2334 Corrosion Test (US Army Corrosion Summit)." 2006, from www.armycorrosion.com.

Reumont, G., J. B. Vogt, A. Iost and J. Foct (2001). "The effects of an Fe-Zn intermetallic-containing coating on the stress corrosion cracking behavior of a hot-dip galvanized steel." Surface & Coatings Technology 139: pp.265~271.

Roudabush, L. A., D. C. McCune and H. E. Townsend (1995). Update on the Development of An Improved Cosmetic Corrosion Test By the Automotive and Steel Industries. Philidelphia, PA, American Society for Testing and Materials.

Sephton, M. and P. C. Pistorius (2000). "Localized Corrosion of Carbon Steel Weldments." Corrosion 56(12): pp.1272~1279.

Simpson, T. C., J. D. Hoffman, L. Soreide and D. H. Meyer (1998). "Corrosion Performance of Tailor Welded Blanks." Corrosion 98(Paper 745): pp.1~20.

Skoog, D. A., F. J. Holler and T. A. Nieman (1997). Principles of Instrumental Analysis. Toronto, Saunders College Publishing.

Slunder, C. J. and W. K. Boyd (1983). Zinc: Its Corrosion Resistance. New York, International Lead Zinc Research Organization Inc.

Sreenivasan, N. (2007). "Effects of Laser Welding on Formability Aspects of Advanced High Strength Steel." Mechanical and Mechatronics Engineering. Waterloo. University of Waterloo. MASc

Stern, M. and A. L. Geary (1957). "Electrochemical Polarization: I. A Theoretical Analysis of the Shape of Polarization Curves." Journal of the Electrochemical Society 104(1): pp.55~63.

Thierry, D., D. Massinon and A. Hugot-Le-Goff (1991). "In Situ Determination of Corrosion Products Formed on Painted Galvanized Steel by Raman Spectroscopy." Journal of Electrochemistry Society 138(3): pp.879~880.

Uhlig, H. H. (1955). The Corrosion Handbook. New York, New York, John Wiley & Sons Inc.

Uhlig, H. H. and R. W. Revie (2008). Corrosion and Corrosion Control. Hoboken, New Jersey, John Wiley & Sons, Inc.

Vagge, S. T., V. S. Raja and R. G. Narayanan (2007). "Effect of deformation on the electrochemical behaviour of hot-dip galvanized steel sheets." Applied Surface Science 253: pp.8415~8421.

Van Ooij, W. J., R. A. Edwards and G. L. Neihelse (1991). Cosmetic Corrosion of Welded Hot-Dip Galvanized Steel Panels. The 5th Automotive Corrosion & Prevention Conference.

Vyas, B. and H. S. Isaacs (1978). "Detecting Susceptibility to Intergranular Corrosion of Stainless Steel Weld Heat Affected Zones." ASTM International: pp.133-145.

Xia, M., N. Sreenivasan, S. Lawson, Y. Zhou and Z. Tian (2007). "A Comparative Study of Formability of Diode Laser Welds in DP980 and HSLA Steels." Journal of Engineering Materials and Technology 129(3): pp.446~452.

Xie, J. and P. Denney (2001). "Galvanized Steel Joined with Lasers." Welding Journal 80(6): pp.59~61.

Yadav, A. P., H. Katayama, K. Noda, H. Masuda, A. Nishikata and T. Tsuru (2007). "Effect of Fe-Zn alloy on the corrosion resistance of galvanized steel in chloride containing environments." Corrosion Science 49(3): pp.3716~3731.

Yadav, A. P., A. Nishikata and T. Tsuru (2004). "Degradation mechanism of galvanized steel in wet-dry cyclic environment containing chloride ions." Corrosion Science 46(2): pp.361~376.

Zhang, X. G. (1996). Corrosion and Electrochemistry of Zinc. New York, Plenum Publication Co.

Zhang, X. G. (2000). "Galvanic Protection Distance of Zinc-Coated Steels Under Various Environmental Conditions." Corrosion 56(2): pp.139~143.

Zhang, X. G. and E. M. Valeriote (1993). "Galvanic Protection of Steel and Galvanic Corrosion of Zinc Under Thin Layer Electrolytes." Corrosion Science 34(12): pp.1957~1972.

Zhu, F., D. Persson, D. Thierry and C. Taxen (2000). "Formation of Corrosion Products on Open and Confined Zinc Surfaces Exposed to Periodic Wet/Dry Conditions." Corrosion 56(12): pp.1256~1265.

APPENDIX A:

SAE J2334 Programming Steps for CC450XP

Test specimens are placed in an enclosed chamber and exposed to a changing climate that comprises of the following 3 part repeating cycle. 6 hours exposure to a water fog/condensing humidity climate of 100%RH at 50°C. This is followed by 15 minutes immersion in (or a direct spray of) salt water at ambient temperature. This is followed by 17 hours 45 minutes of air drying in a climate of 50%RH at 60°C.

The number of cycle repeats and therefore the test duration is variable.
(7 day week - Automatic Operation)

1. Identify a blank Main Program (existing programs can be blanked by using the delete command)

2. Create a Main Program titled SAE J2334

Step 1 = Wetting function, at 50.0C, for 1 minute (special *rapid* step)*[1]
Step 2 = Wetting function, at 50.0C, for 5 hours & 59 minutes *[1]
Step 3 = Salt Spray function, at 20.0C, for 1 minute (special *rapid* step) *[2] *[3]
Step 4 = Salt Spray function, at 20.0C, for 14 minutes*[2] *[3]
Step 5 = Controlled Humidity function, at 60.0C/50%RH, for 1 minute (special *rapid* step)
Step 6 = Controlled Humidity function, at 60.0C/50%RH, for 17 hours & 44 minutes.
Steps 7 to 15 = Function OFF and zero time

Repeats = set as required (typically 59 repeats as J2334 is usually conducted for a minimum of 60 cycles)

*[1] If ACC32 (water fog humidity) option is fitted, this function can be selected for steps 1 & 2.

*[2] If ACC30 (salt spray vertically down) option is fitted, this function can be selected in place
of salt spray, steps 3 & 4. This option would also allow the 'normal' salt spray function to be used as a water fog humidity generator for steps 1 & 2.

*[3] If ACC34 (liquid immersion) option is fitted, this function can be selected for steps 3 & 4. This option would also allow the salt spray function to be used as a water fog humidity generator for steps 1 & 2.

APPENDIX B:

Gravimetric measurements after cyclic testing using SAE J2334

Table B1: Average weight gain in grams of IF welded coupons at 30, 45 and 60 cycles

Thickness	Exposed Width	Day 30	Day 45	Day 60
0.77	0 mm	0.0729	0.0929	0.1074
	1 mm	0.0861	0.1123	0.1440
	3 mm	0.0857	0.1210	0.1604
	5 mm	0.0950	0.1503	0.2514
1.77	0 mm	0.0659	0.0936	0.1395
	1 mm	0.0784	0.1104	0.1514
	6 mm	0.0986	0.2174	0.5038
	9 mm	0.1711	0.5486	1.3181

Table B2: Average weight gain in grams of HSLA welded coupons at 30, 45 and 60 cycles

Thickness	Exposed Width	Day 30	Day 45	Day 60
0.77	0 mm	0.0384	0.0650	0.0983
	1 mm	0.0873	0.1075	0.1222
	3 mm	0.1188	0.1476	0.1762
	5 mm	0.1017	0.1579	0.2316
1.77	0 mm	0.0674	0.0908	0.1273
	1 mm	0.0771	0.1088	0.1473
	7 mm	0.1026	0.2613	0.6482
	11 mm	0.2430	0.5503	1.2952

Table B3: Average weight gain in grams of IF deformed coupons at 30, 45 and 60 cycles

Thickness	Exposed Width	Day 30	Day 45	Day 60
0.77	0 mm	-0.2670	-0.0279	0.1211
	1 mm	0.0722	0.0992	0.1275
	3 mm	0.6585	0.5559	0.6086
	5 mm	0.1877	0.1299	0.2029
1.77	0 mm	0.0689	0.1038	0.1391
	1 mm	0.0645	0.0957	0.1356
	6 mm	0.1648	0.3250	0.7855
	9 mm	0.3422	0.7807	1.5963

Table B4: Average weight gain in grams of HSLA deformed coupons at 30, 45 and 60 cycles

Thickness	Exposed Width	Day 30	Day 45	Day 60
0.77	0 mm	0.0695	0.1020	0.1288
	1 mm	0.0710	0.1022	0.1276
	3 mm	0.0834	0.3868	0.4966
	5 mm	0.1264	0.2220	0.5757
1.77	0 mm	0.0803	0.1190	0.1589
	1 mm	0.0841	0.1276	0.1787
	7 mm	0.1786	0.3962	0.8026
	11 mm	0.3613	0.9585	2.1542

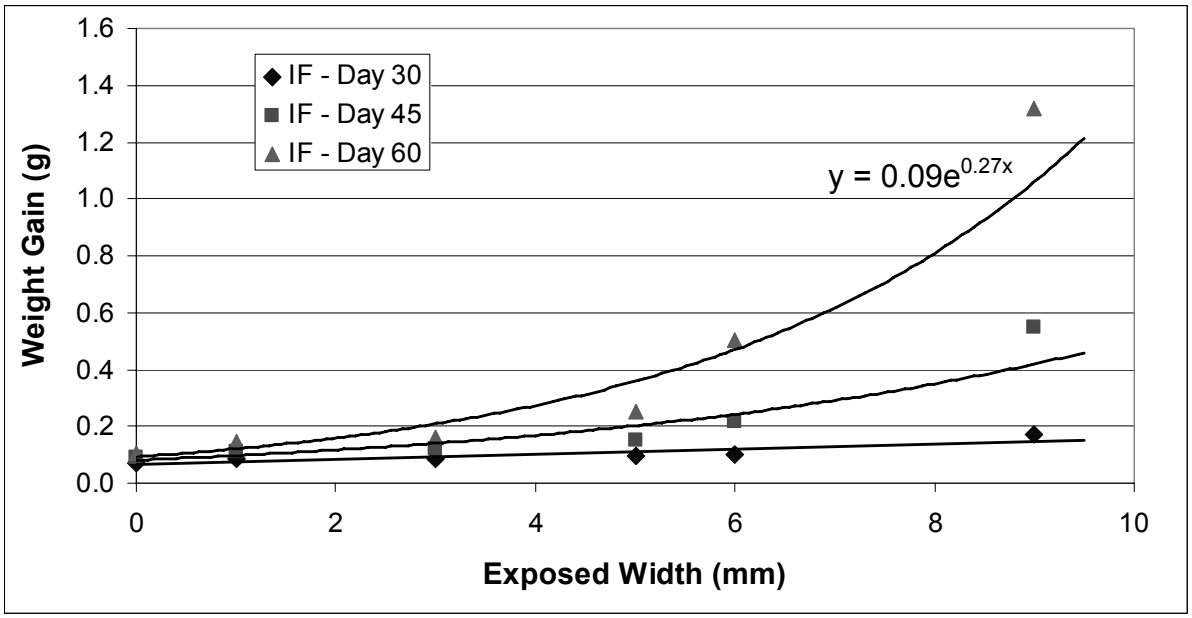

Figure B1: Weight gain vs. exposed width of IF welded coupons at 30, 45 and 60 cycles

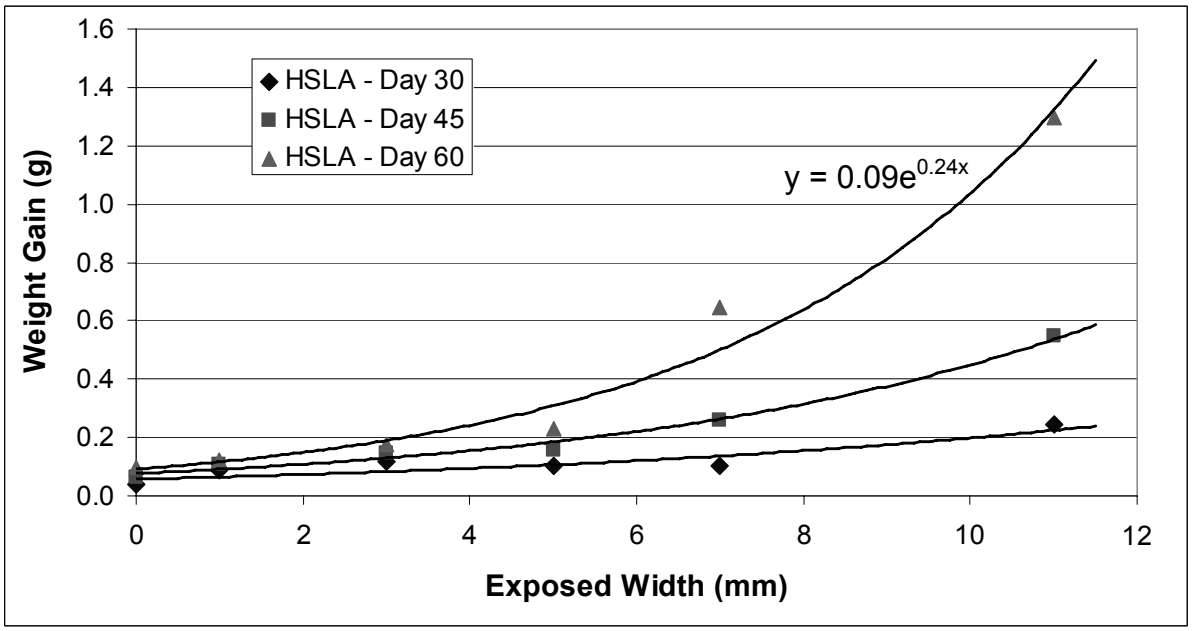

Figure B2: Weight gain vs. exposed width of HSLA welded coupons at 30, 45 and 60 cycles

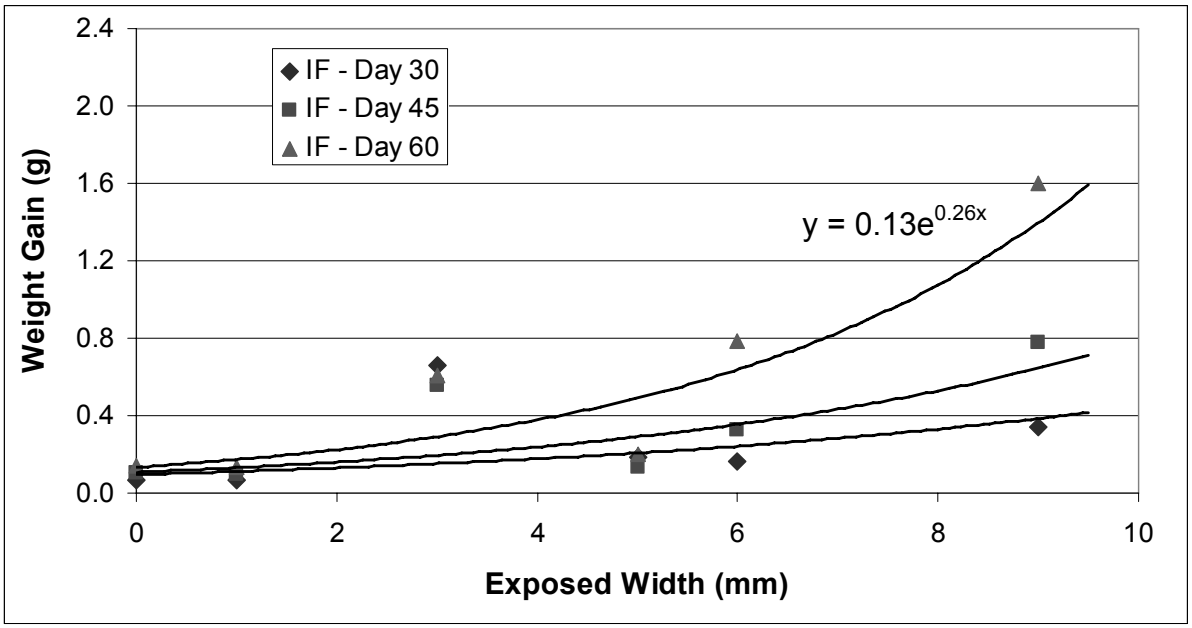

Figure B3: Weight gain vs. exposed width of IF deformed coupons at 30, 45 and 60 cycles

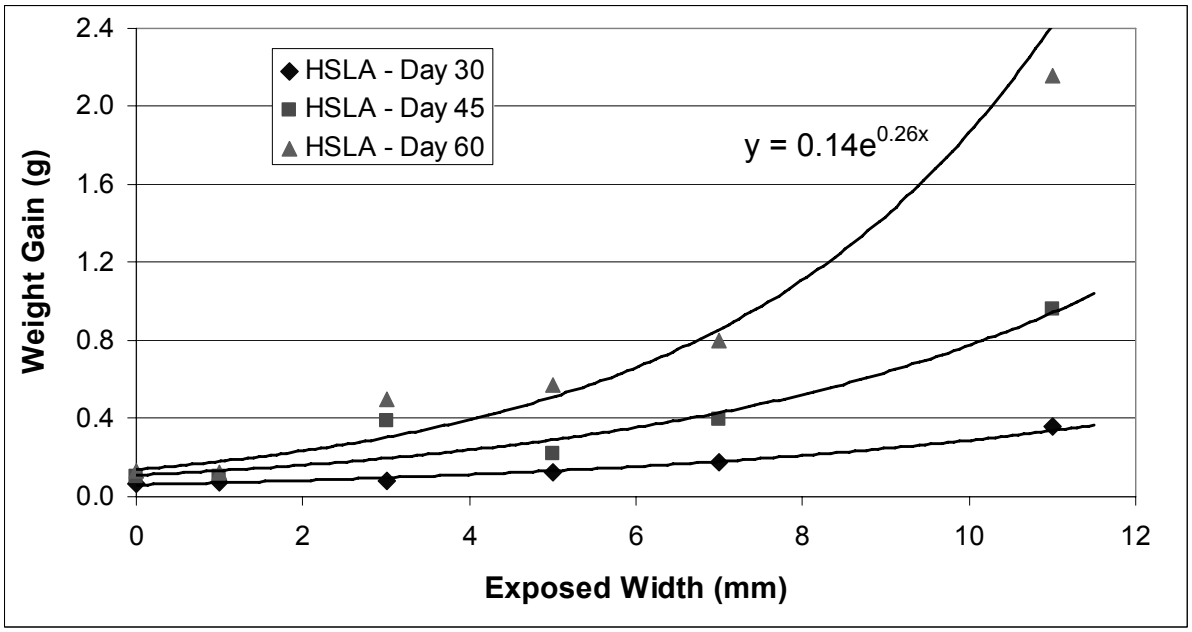

Figure B4: Weight gain vs. exposed width of HSLA deformed coupons at 30, 45 and 60 cycles